



Physik-Department

Munich School of Bioengineering

Low-Field NMR: 2D Relaxation Data Analysis and Multi-Channel System Development

Stephan Johannes Huber

Vollständiger Abdruck der von der Fakultät für Physik der Technischen Universität München zur Erlangung des akademischen Grades eines

Doktors der Naturwissenschaften (Dr. rer. nat.)

genehmigten Dissertation.

Vorsitzender: Prof. Dr. Ulrich Gerland

Prüfer der Dissertation: 1. Prof. Dr. Axel Haase

2. Priv.-Doz. Dr. Marion I. Menzel

Die Dissertation wurde am 24.05.2018 bei der Technischen Universität München eingereicht und durch die Fakultät für Physik am 07.01.2019 angenommen.

Abstract

Low-field NMR investigations are increasingly executed in a broad set of fields like biology, chemistry or diagnostics. Often low-field setups are characterized by the use of permanent magnets which offer a high degree of mobility and a reduction in cost. In turn, SNR and resolution get decreased.

This work deals with two projects within the framework of low-field NMR. First, this is the development of a novel algorithm for the numerical Laplace inversion of 2D relaxation data which aims to enhance the resolution of relaxometry studies. Second, this is the development of a mobile multi-channel hetero-nuclear NMR platform to increase the sample throughput of low-field investigations but concurrently maintain the portability and flexibility of the setup.

In the first project, to analyze 2D NMR relaxation data based on a discrete delta-like relaxation map the Padé-Laplace method was extended to two dimensions by using Chisholm approximations. With a simulated dataset based on a discrete map it is shown that the Chisholm approximation method outcome is superior to the state-of-the-art Tikhonov regularization method for SNRs larger than 50. Based on an experimental dataset with a SNR of 750 it is shown that the Chisholm approximation method was able to resolve two relaxation compartments differing by a factor of 1.7 in 8 of 10 cases. In contrast to that the Tikhonov regularization method was able to separate them in 3 of 10 cases.

In the second project, to achieve a higher sample throughput in low-field experiments a portable hetero-nuclear multi-channel NMR system was developed. In order to implement multi-channel capabilities but concurrently avoid redundant system multiplications parallelized micro-coil arrays with active decoupling capabilities were developed. The necessary signal processing and serialization was implemented digitally with alleviated resource requirements. In addition, a tailored set of time-interleaved IR, CPMG and spectroscopy sequences were developed which enabled a quasi-parallel acquisition of NMR relaxation times and spectra. The system was characterized and validated with the rapid determination of ^1H relaxation times at 0.5 T. The acquisition of T_1 and T_2 times was sped up by a factor of nearly 4. For ^1H and ^{19}F hetero-nuclear spectroscopy at 1 T a decrease in the measurement time by a factor of nearly 6 was achieved. Moreover parallel ^{13}C and ^1H spectroscopy capabilities at 1 T were demonstrated with field-locking procedures.

In conclusion, with the Chisholm approximation method a novel algorithm was developed which shows superior capabilities for discrete delta-like 2D relaxation maps at moderate SNR. In addition a unique multi-channel setup was developed and validated with high-throughput relaxation and spectroscopy studies at low-field.

Zusammenfassung

Niederfeld NMR Anwendungen kommen in Bereichen wie der Biologie, der Chemie und bei Diagnoseanwendungen vermehrt zum Einsatz. Die Aufbauten zeichnen sich dabei oftmals durch die Verwendung von Permanentmagneten aus. Dadurch wird eine Kostenreduktion bei einem gleichzeitigem Gewinn an Mobilität erreicht. Im Gegensatz dazu sinkt aber das SNR und die Auflösung.

Diese Arbeit befasst sich mit zwei Projekten im Bereich der Niederfeld NMR. Zum einen ist dies die Entwicklung eines neuartigen Algorithmuses zur numerischen Laplace Invertierung von 2D Relaxationsdaten mit dem Ziel, die Auflösung von Relaxometrie-Studien zu erhöhen. Zum anderen ist dies die Entwicklung eines mobilen mehrkanaligen NMR Systems für mobile hetero-nukleare Anwendungen mit hohem Durchsatz.

Im ersten Projekt wurde die Padé-Laplace Methode auf zweidimensionale Datensätze durch die Verwendungen von Chisholm Approximierten erweitert. Mittels einer simulierten diskreten Relaxationsverteilung wurde gezeigt, dass die Methode der Chisholm Approximierten dem Stand der Technik des Tikhonov Verfahrens ab einem SNR von 50 überlegen ist. Mittels eines experimentellen Datensatzes mit einem SNR von 750 wurde gezeigt, dass die Methode der Chisholm Approximierten zwei Relaxations-Kompartimente in 8 von 10 Fällen auflösen kann, wenn sich diese um einen Faktor von 1.7 unterscheiden. Im Vergleich dazu konnte die Tikhonov-Methode diese nur in 3 von 10 Fällen auflösen.

Im zweiten Projekt wurde ein mobiles hetero-nukleares NMR System entwickelt. Zur Implementierung mehr-kanaliger Funktionalitäten bei gleichzeitiger Vermeidung von redundanter Hardware-Vervielfachung wurden parallelisierte Micro-Spulen Arrays mit einem aktiven Entkopplungskreis entwickelt. Die dazugehörige Signalverarbeitung wurde digital unter verringertem Ressourcenbedarf implementiert. Zusätzlich wurden maßgeschneiderte zeitmultiplexing Sequenzen für IR, CPMG und Spektroskopie-Anwendungen entwickelt. Diese erlauben eine quasi-parallele Aufzeichnung von Relaxationszeiten und Spektren. Das System wurde charakterisiert und mit der beschleunigten Aufzeichnung von ^1H Relaxationszeiten bei 0.5 T validiert. Die Aufnahme konnte dabei um nahezu einen Faktor 4 beschleunigt werden. Für hetero-nukleare ^1H und ^{19}F Spektroskopie Anwendungen konnte die Messzeit um nahezu einen Faktor 6 verkürzt werden. Zudem wurde die Flexibilität des System mittels der kombinierten ^{13}C und ^1H Spektroskopie mit einem Field-Lock Verfahren demonstriert.

Letztlich wurde mit der Methode der Chisholm-Approximierten ein neuartiger Algorithmus entwickelt, der bei diskreten Relaxationsverteilungen auf Grund seiner Eigenschaften vorzuzugswürdig ist. Zudem wurde eine mehrkanalige NMR Plattform entwickelt und durch hetero-nukleare Relaxations- und Spektroskopie Anwendungen mit hohem Durchsatz validiert.

Contents

| | | |
|----------|--|-----------|
| 1 | Introduction | 1 |
| 1.1 | Analysis of 2D Relaxation Data using Chisholm Approximations | 1 |
| 1.2 | Multi-Channel NMR System Development | 2 |
| 2 | Theory | 5 |
| 2.1 | Nuclear Induction | 5 |
| 2.2 | Relaxation | 10 |
| 2.3 | NMR Probe Circuit Design | 12 |
| 2.4 | Signal-to-Noise Ratio of a NMR Experiment | 15 |
| 3 | Analysis of 2D Relaxation Data using Chisholm Approximations | 17 |
| 3.1 | Algorithm | 17 |
| 3.2 | Methods | 21 |
| 3.2.1 | Simulation | 21 |
| 3.2.2 | Experiment | 23 |
| 3.2.3 | Implementation | 23 |
| 3.3 | Results | 25 |
| 3.3.1 | Simulation | 25 |
| 3.3.2 | Experiment | 26 |
| 3.4 | Discussion | 29 |
| 4 | Multi-Channel NMR System Development | 37 |
| 4.1 | Methods - System Development | 37 |
| 4.1.1 | System Overview | 37 |
| 4.1.2 | Digital Processing Unit | 38 |
| 4.1.3 | Analog Amplification Unit | 40 |
| 4.1.4 | NMR Coils | 44 |
| 4.1.5 | Pulse Sequences | 45 |
| 4.1.6 | Data Analysis | 46 |
| 4.2 | Methods - NMR Application | 48 |
| 4.2.1 | General Settings | 48 |
| 4.2.2 | Quattro Channel - qCoil | 48 |
| 4.2.3 | Hexa Channel - hCoil | 49 |
| 4.2.4 | Dual Channel - bCoil | 50 |
| 4.3 | Results - System Development | 50 |
| 4.3.1 | Digital Processing Unit | 50 |

| | | |
|----------|---|------------|
| 4.3.2 | Analog Amplification Unit | 51 |
| 4.3.3 | NMR Coils | 54 |
| 4.4 | Results - NMR Application | 62 |
| 4.4.1 | General Setup | 62 |
| 4.4.2 | Quattro Channel - qCoil | 62 |
| 4.4.3 | Hexa Channel - hCoil | 68 |
| 4.4.4 | Dual Channel - bCoil | 69 |
| 4.5 | Discussion | 69 |
| 4.5.1 | System Development | 69 |
| 4.5.2 | NMR Application | 77 |
| 5 | Conclusion | 85 |
| 6 | Appendix | 95 |
| 6.1 | Coil Matching Capacitances | 95 |
| 6.2 | DVD | 96 |
| 6.3 | RF Characterization Instruments | 97 |
| 7 | List of Publications | 99 |
| 8 | Acknowledgments | 101 |

1 Introduction

Low-field NMR is characterized through permanent magnets generating the required external magnetic field B_0 [1]. Several advantages come along with this. Permanent magnets are not based on superconductors and do not require a cost and maintenance intensive cooling. Additionally they can get manufactured in a compact way which makes them portable and cheap.

However, also drawbacks are associated with that. Technically, permanent magnets suffer from a limited field strength, a limited homogeneous volume and a temperature dependent field drift. Experimentally this causes a decreased SNR and a low chemical resolution with respect to superconducting high field magnets.

Nevertheless during the last years a broad set of applications were successfully developed for low-field NMR spectroscopy [2,3], frequently in combination with NMR system developments. Those are for example a high-resolution ex-situ setup [4], a lab-on-chip reaction monitoring platform [5] or further applications in process monitoring [6].

Besides that, NMR relaxometry developed to a successful tool within the NMR community. For example the transversal relaxation time T_2 is a versatile probe to monitor the binding state of functionalized magnetic nanoparticles with biomarkers [7]. Since the functionalization can get customly designed and has a direct influence on the binding partners, a highly applicable diagnosis platform was developed. In addition to this one-dimensional relaxometry, two-dimensional relaxation experiments emerged during the last decade [8] and are now a substantial feature in low-field NMR.

This work is split into two parts. The first part deals with the development of a novel algorithm to analyze the outcome of such two-dimensional relaxation experiments. The second part of this work is about the development of a multi-channel low-field NMR setup specifically suited for high-throughput relaxation and spectroscopy experiments.

1.1 Analysis of 2D Relaxation Data using Chisholm Approximations

In two dimensional NMR relaxation experiments the relaxation behavior of a sample is examined as a function of two independent variables. This allows a related study by investigating a combination of the longitudinal or transversal relaxation times T_1 and T_2 as well as the diffusion coefficient D . The result of such an experiment can be regarded as a 2D Laplace transform of an underlying relaxation map which shows the correlated two dimensional relaxation behavior of the sample and gives new physical insight. Consequently, in order to get the relaxation map, an inverse Laplace transform of the experimental signal is necessary [9, 10].

Methodically 2D relaxation experiments first became feasible with the upcome of an efficient algorithm, namely the Tikhonov regularization method, to perform such a 2D Laplace inversion [11]. Nowadays 2D relaxation studies are an important aspect of low field NMR and find application in many distinct fields. For example in porous rocks T_2 - T_2 experiments are used to determine the exchange rates between different pore systems [12]. Furthermore, in the petrol industry T_1 - T_2 correlation maps are employed in the examination of oil bearing rocks [13]. Another example is the food industry where D - T_2 experiments can be used to analyze diary products [14].

However, the numerical Laplace inversion is an ill-posed problem. Due to the signal's noise content small changes in the experimental data may cause a different outcome of the inversion process. To cope with that the Tikhonov regularization method is based on a least squares procedure and assumes that the relaxation distribution is smooth. For that reason it requires the adjustment of a smoothing parameter α by the user.

This parameter must undergo a time consuming optimization process. Also there are samples like bulk compartments which posses not a smooth but a discrete delta-like distribution of relaxation rates. Furthermore, the algorithm requires the definition of a memory expensive kernel matrix which defines the resolution of the outcome. When discrete relaxation rates are closely spaced they may not get resolved by the algorithm when the kernel matrix is too coarse.

In this work a new algorithm was developed for the 2D numerical Laplace inversion which is able to resolve a delta-like distribution of relaxation rates. There is no parameter which requires an optimization process and it is not based on a least squares procedure. Finally the resolution is limited by the noise, the sampling rate and the numerical precision, a memory consuming kernel matrix is not required. Eventually the algorithm is based on the ideas of the Padé-Laplace method [15] and extends it to two dimensions by using so called Chisholm approximations [16, 17].

1.2 Multi-Channel NMR System Development

To further exploit the low-field merits and concurrently attenuate the drawbacks like the decreased resolution and limited SNR, hardware development is an ongoing field of research [18, 19] for low-field setups.

So far, there are several works describing the miniaturization of NMR systems even down to developing integrated chips with NMR functionality [20, 21]. However, most of this work is dealing with single-channel (SC) devices. Only a few focus on multi-channel (MC) setups [22, 23]. Although they would provide a higher sample throughput and a gain of flexibility for spectroscopy and for relaxometry applications.

Recently it was shown that a miniaturized low-field setup allows the investigation of the metabolic flux of tumor cells based on ^{13}C spectroscopy. In addition to that ^{19}F spectroscopy

develops more and more to a versatile tool in NMR cell tracking [24]. In both cases a multi-channel device would clearly increase the applicability through a higher sample throughput.

Furthermore for T_2 targeted binding applications there are sample series which are unstable. Still, to ensure a comparison within a series, it would be ideal to measure all samples simultaneously. Here the quality of the outcome would also gain from MC capabilities. Hence, there are several promising applications for a hetero-nuclear multi-channel platform that would allow accelerated NMR studies at low B_0 fields. The second project of this work was devoted to the development of such a platform.

So far, existing MC systems follow a rather multiplicative approach, i.e. SC systems were duplicated and stacked to get MC systems [25,26]. Clearly, with that approach not only the system but also the required spacing, cost and power consumption get multiplied.

Here a low field multi-channel NMR system termed mNMR is presented. In this setup only the NMR coils got multiplied to a MC probe array with active decoupling capabilities. The rest of the system has only SC requirements. Therefore a time-multiplexed procedure got employed along with a parallelization in the digital domain. Additionally custom time-interleaved T_1 , T_2 and spectroscopy sequences were designed, implemented and validated in the system for hetero-nuclear spectroscopy and ^1H relaxometry.

2 Theory

The first nuclear magnetic resonance (NMR) experiments were conducted more than 75 years ago. In 1938 Rabi et al. were able to induce resonant transitions between nuclear spin states [27]. They used an apparatus similar to the famous Stern-Gerlach setup and worked with a molecular beam. Independent of each other Bloch et al. and Purcell et al. proceeded with that work. In 1946 both were able to observe NMR in bulk materials [28,29]. Especially Bloch's approach was a landmark for NMR experiments and was temporarily termed 'Nuclear Induction'.

Although at the beginning NMR was rather a method to study fundamental physical properties, in the upcoming years it developed to an outstanding method in science, industry and healthcare. It is impossible to appreciate all contributors independently, only a few milestones should be mentioned. For example, there is the initial discovery of the chemical shift by Proctor et al. [30]. Based on this Wüthrich and Ernst implemented methods to elucidate the structure of molecules through NMR spectroscopy [31]. In addition to that Lauterbur and Mansfield introduced spatially resolved routines which paved the way to clinical imaging applications of NMR [32].

In this chapter the underlying theory of NMR will be introduced. Subsequently the behavior of relaxation times will be analyzed with a focus on the influence of paramagnetic impurities inside the sample. The last two sections serve to describe the NMR probe circuit and give a qualitative analysis of the SNR.

2.1 Nuclear Induction

Atomic nuclei with a spin \vec{I} also possess a magnetic moment $\vec{\mu}$, connected by the gyromagnetic ratio γ as given in Eq. 2.1.

$$\vec{\mu} = \gamma \vec{I} \tag{2.1}$$

In this work only nuclei with spin $1/2$ will be considered, i.e. along a preferred direction there are only two possible spin quantum numbers m_I with $-1/2$ and $+1/2$ available for a single spin. In free space both spin states are degenerated. When brought into an external magnetic field $\vec{B}_0 = (0, 0, B_0)$, due to the Zeeman effect, the levels will split up according to Eq. 2.2.

$$E = -\vec{\mu} \cdot \vec{B}_0 \tag{2.2}$$

Nuclei with a parallel spin $+1/2$ will be in a low energy state, vice versa an anti-parallel spin with $-1/2$ will be in a high energy state. Because a parallel spin alignment is preferred,

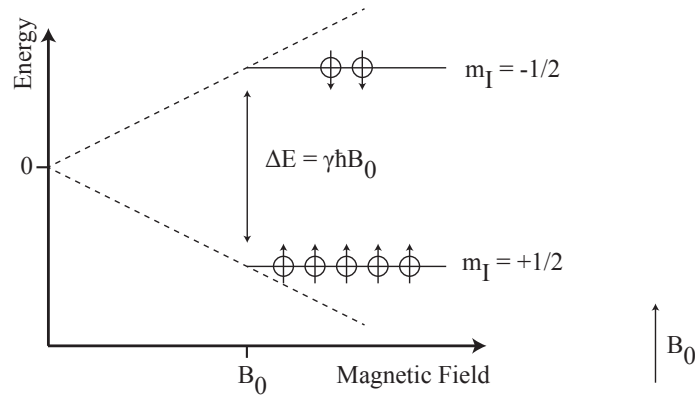


Figure 2.1: Zeemann splitting of spins in an external magnetic field B_0 . Tiny arrows indicate the spin quantum number. The population difference is strongly exaggerated.

there will be a population difference, Fig. 2.1. For that reason, the sum over all nuclei in bulk samples will result in a net macroscopic magnetic moment \vec{M} .

One must note that the population difference as shown in Fig. 2.1 is greatly exaggerated. In general cases the level population follows a Boltzmann distribution. However, for technically accessible magnetic fields the energy difference $\gamma\hbar B_0$ is several orders smaller than $k_B T$. This makes the resulting Boltzmann factor nearly zero and allows to approximate the Boltzmann distribution. The resulting magnetization is given in Eq. 2.3 [33], where the sample temperature is denoted with T and N is the spin density.

$$M = \frac{1}{4} \frac{N \gamma^2 \hbar^2 B_0}{kT} \quad (2.3)$$

In their seminal work [28, 34] Bloch and coworkers studied the behavior of \vec{M} with a semi-classical approach. In the presence of an external magnetic field \vec{B} a magnetic moment vector \vec{M} will experience a torque given by Eq. 2.4.

$$\frac{d\vec{M}}{dt} = \gamma \vec{M} \times \vec{B} \quad (2.4)$$

Equation 2.4 must get analyzed for two cases. The first case is when \vec{B} is equal to B_0 and \vec{M} is perpendicular to the z-axis. According to Eq. 2.4 this will cause a rotation of \vec{M} around the z-axis. The angular velocity ω_L of this rotation is given in Eq. 2.5, in most cases it is simply termed Larmor frequency.

$$\omega_L = -\gamma B_0 \quad (2.5)$$

The second case is when in addition to B_0 an alternating magnetic field B_1 is applied, perpendicular to B_0 and oscillating with ω_L . For simplicity \vec{M} is supposed to be parallel to \vec{e}_z . In this instance one can transform the system into a rotating frame of reference and show

that the magnetic moment will rotate around B_1 , again with the Larmor frequency. When the alternating field B_1 is only applied for a time τ , the magnetic moment will get tipped away from the z-axis by an angle α given in Eq. 2.6.

$$\alpha = \gamma B_1 \tau \quad (2.6)$$

With this in mind one can study the basics of a NMR setup, Fig. 2.2 A). A coil which contains the sample under investigation is placed in a magnetic field B_0 in such a way that the coil will generate a excitation field B_1 perpendicular to B_0 . When a resonant excitation pulse (Tx) gets applied to the coil, the macroscopic magnetic moment will leave its equilibrium position and rotate according to Eq. 2.4. The Larmor precession of \vec{M} around \vec{B}_0 will generate a time dependent magnetic flux in the coil and induce a receive (Rx) voltage, which is detectable when the pulse is off. This is the pulsed version of Bloch's 'Nuclear Induction' principle which is now the basis for literally all NMR experiments.

Besides that Bloch also introduced a set of phenomenological equations describing the behavior of the magnetic moment vector more generally [34, 35]. Now, those equations are termed the Bloch-equations and are given in Eq. 2.7. Two relaxation times are introduced, the longitudinal relaxation time T_1 and the transversal relaxation time T_2 . The first measures how fast the equilibrium of M_z will get restored (spin-lattice relaxation) after a deflection of \vec{M} . The latter describes how fast the individual constituents $\vec{\mu}$ of the macroscopic magnetic moment will lose coherence. This loss of coherence can have two causes. First the spin-spin relaxation, i.e. the exchange of energy between individual spins. The second case is mostly of an experimental cause. Due to inhomogeneities in the static magnetic field B_0 , Fig. 2.2 B), different spins will experience a different Larmor frequency which accelerates the loss of coherence. For that reason the x- and y-component of \vec{M} decay with a time constant T_2^* which takes the inhomogeneities into account and is smaller than T_2 .

$$\frac{dM_x}{dt} = \gamma (\vec{M} \times \vec{B})_x - \frac{M_x(t)}{T_2} \quad (2.7a)$$

$$\frac{dM_y}{dt} = \gamma (\vec{M} \times \vec{B})_y - \frac{M_y(t)}{T_2} \quad (2.7b)$$

$$\frac{dM_z}{dt} = \gamma (\vec{M} \times \vec{B})_z - \frac{M_z(t) - M_0}{T_1} \quad (2.7c)$$

Figure 2.2 C) shows the basic outcome of a single pulse NMR experiment. The resonant pulse is denoted with the square. The excited signal is called a free induction decay (FID) [36]. The sample dependent spin-spin relaxation time T_2 is shown in the background. The magnetic moment \vec{M} decays exponentially with the shorter T_2^* time due to magnetic inhomogeneities. A Fourier transform of such an exponentially damped Larmor oscillation gives a Lorentzian peak centered at ω_L with a linewidth proportional to $1/T_2^*$. In general the Fourier analysis

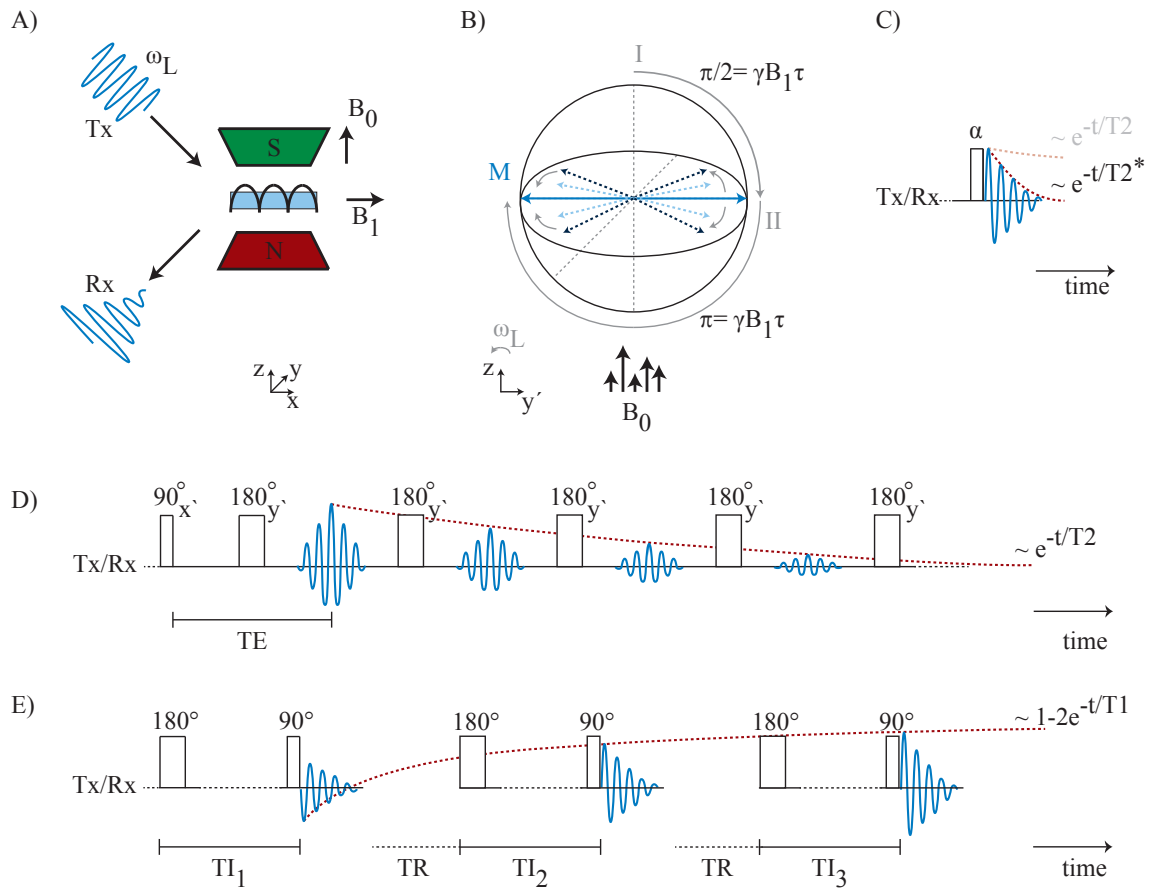


Figure 2.2: A) Basic pulsed NMR experiment. B) Rotating frame of reference showing the dephasing after a 90° pulse (I) and the rephasing after a 180° pulse, both due to B_0 inhomogeneities. C) FID signal after a resonant excitation with flip angle α . D) CPMG (Carr-Purcell-Meiboom-Gill) sequence for T_2 determination. E) IR (Inversion Recovery) sequence for T_1 determination.

of a NMR signal gives a spectrum showing the distribution of Larmor frequencies in the sample. There are two effects influencing this distribution. Those are the field dependent chemical shift [30] and the field independent spin-spin or scalar coupling. The chemical shift is caused by the magnetic shielding through the electronic shell of a nucleus. Nuclei with a different electronic surrounding will experience microscopically a different B_0 field and hence a different Larmor frequency. The scalar coupling originates from a spin-spin interaction between different nuclei. It is mediated through the electronic bonds within a molecule and causes a splitting of spectral lines into multiplets [35].

Figure 2.2 D) shows a Carr-Purcell-Meiboom-Gill (CPMG) sequence to measure T_2 [37,38]. The basic building block is a so called spin echo [39]. The formation of a spin echo is also illustrated in Figure 2.2 B) for a 90° - 180° example. After the 90° pulse (I) the magnetic moment will dephase due to B_0 inhomogeneities. Through an additional 180° pulse (II), applied after a time $TE/2$, the dephasing gets reversed and a spin echo will form at the echo time TE . When typical diffusion lengths are negligible with respect to the spatial field inhomogeneities, the spin echo signal will experience the pure T_2 decay [40]. In Fig. 2.2 D) the excitation pulses are indicated by their B_1 directions x' and y' in the rotating frame of reference, equivalent to the phase in the laboratory frame. This is necessary to suppress the influence of pulse imperfections on the echo train [38].

Finally, to determine the T_1 relaxation time an inversion recovery sequence, Fig. 2.2 E), can be used. Through a 180° pulse the magnetic moment gets rotated parallel to $-\vec{e}_z$. During an inversion time (TI) it relaxes with T_1 . Then the current state of \vec{M} gets probed with a 90° pulse. Afterwards a suitable long relaxation period (TR) is added to ensure a complete equilibrium restoration and the procedure gets repeated for an additional inversion time TI with a different length.

In Fig. 2.3 the two-dimensional extensions of the IR and CPMG sequences are shown [41]. In both cases the narrow and broad rectangles represent 90° and 180° pulses respectively. Figure part A) shows a T_2 - T_2 sequences where two CPMG sequences are concatenated and separated by an exchange period τ_{Ex} . Data are only acquired during the second CPMG train which is also called the direct train. Usually this sequence is repeated for a different number of echoes i in the first (indirect) CPMG train. With this sequence the exchange between different relaxation compartments can be studied [12].

Figure 2.3 B) shows a T_1 - T_2 sequence. To a preceding IR sequence (indirect dimension) a CPMG train (direct dimension) is attached. Again, data are only acquired in the direct dimension. In general this sequence gets repeated for a set of TI. With this sequence relaxation time correlations are studied [42].

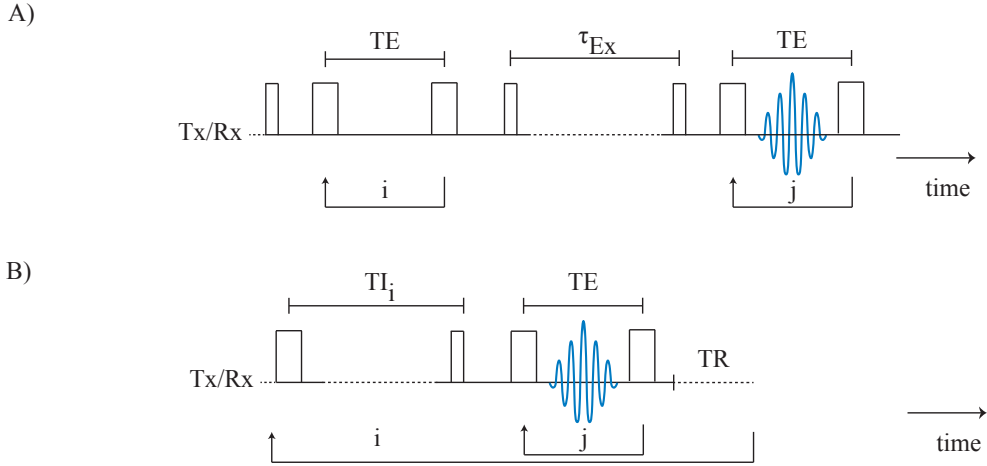


Figure 2.3: Two-dimensional relaxation sequences. A) T_2 - T_2 sequence. B) T_1 - T_2 sequence.

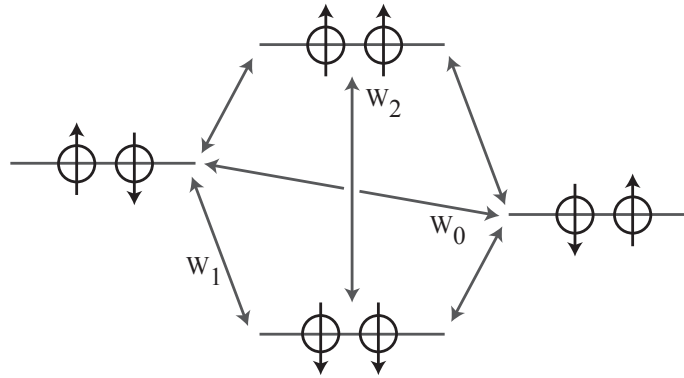


Figure 2.4: The energy levels of two spins with the transition rates W .

2.2 Relaxation

The first theoretical examination of the T_1 and T_2 spin relaxation goes back to the seminal work of Bloembergen et al. [43] and was later developed by Abragam et al. [44] and Solomon [45]. Two spins affect each other through a dipole-dipole interaction. Due to the molecular tumbling a time dependence is introduced which causes transitions between the spin states. In their work, Bloembergen, Abragam and Solomon characterized the random molecular motion through a correlation time τ_C . The correlation time is a measure of how long two spins are in a correlated state with respect to each other. Based on this they calculated the transition rates between spin states and deduced expressions for T_1 and T_2 from that. In the following the calculation of T_1 gets summed up. The T_2 case would be similar and is given in [45].

The energy states of a nuclear spin I and an electron spin S with spin $1/2$ are given in Fig. 2.4 along with the transition rates W .

Based on that one can write down the rate of change of the magnetization of I_z with respect to its equilibrium value I_0 , Eq. 2.8 [45].

$$\frac{dI_z}{dt} = (2W_1 + W_0 + W_2)(I_0 - I_z) + (W_2 - W_0)(S_0 - S_z) \quad (2.8)$$

Equation 2.8 gets significantly simplified when one takes into account that the electron relaxation is fast with respect to the nuclear relaxation, i.e. $S_0 = S_z$. The remaining rates W for transitions between states i and j can be calculated with Eq. 2.9 [45, 46].

$$W_{ij} = \frac{1}{t_0} \frac{1}{\hbar^2} \left| \int_0^{t_0} \langle m_i | \hat{H}'(t) | m_j \rangle e^{i\omega_{ij}t} dt \right|^2 \quad (2.9)$$

Here the individual spin states are given by the bracket notation. The perturbing Hamiltonian $\hat{H}'(t)$ describes the time dependent dipolar interaction between both spins and t_0 is the averaging window which must be larger than the correlation time. The resulting transition rates are given in Eq. 2.10.

$$W_0 = \frac{1}{10} \left(\frac{\mu_0}{4\pi} \right)^2 \frac{\gamma_I^2 \gamma_S^2 \hbar^2}{r_{IS}^6} \frac{\tau_C}{1 + (\omega_S - \omega_I)^2 \tau_C^2} \quad (2.10a)$$

$$W_1 = \frac{3}{20} \left(\frac{\mu_0}{4\pi} \right)^2 \frac{\gamma_I^2 \gamma_S^2 \hbar^2}{r_{IS}^6} \frac{\tau_C}{1 + \omega_I^2 \tau_C^2} \quad (2.10b)$$

$$W_2 = \frac{6}{10} \left(\frac{\mu_0}{4\pi} \right)^2 \frac{\gamma_I^2 \gamma_S^2 \hbar^2}{r_{IS}^6} \frac{\tau_C}{1 + 4(\omega_S + \omega_I)^2 \tau_C^2} \quad (2.10c)$$

Based on this one can write down the relaxation times T_1 by plugging Eq. 2.10 into Eq. 2.8. The result is shown in Eq. 2.11 along with the result for T_2 [45].

$$\frac{1}{T_{1L}} = \frac{1}{10} \left(\frac{\mu_0}{4\pi} \right)^2 \frac{\gamma_I^2 \gamma_S^2 \hbar^2}{r_{IS}^6} \left[\frac{7\tau_C}{1 + \omega_S^2 \tau_C^2} + \frac{3\tau_C}{1 + \omega_I^2 \tau_C^2} \right] \quad (2.11a)$$

$$\frac{1}{T_{2L}} = \frac{1}{20} \left(\frac{\mu_0}{4\pi} \right)^2 \frac{\gamma_I^2 \gamma_S^2 \hbar^2}{r_{IS}^6} \left[\frac{13\tau_C}{1 + \omega_S^2 \tau_C^2} + \frac{3\tau_C}{1 + \omega_I^2 \tau_C^2} + 4\tau_C \right] \quad (2.11b)$$

Here, r_{IS} gives the distance between the nuclear spin I and the electron spin S and ω denotes their Larmor angular frequencies. In Eq. 2.11 it is already assumed that $\omega_S \gg \omega_I$. Finally the two gyromagnetic ratios are designated with γ_I and γ_S respectively. In particular γ_S is defined with Eq. 2.12. Where g_s is the g-factor of the electron spin S and μ_B is the Bohr magneton.

$$\gamma_S = \frac{g_s \mu_B}{\hbar} \quad (2.12)$$

With that one can describe the relaxation of an aqueous solution doped with paramagnetic ions, i.e. the relaxation of a nuclear spin in the presence of an electronic spin. In such a case the overall relaxation rate, Eq. 2.13, consists out of two contributions which are additive [47].

$$\frac{1}{T_i} = \frac{1}{T_{iW}} + \frac{1}{T_{iP}} = R_{i,0} + c_p \cdot r_i \quad (2.13)$$

In Eq. 2.13 the index i stands for either the longitudinal ($i = 1$) or the transversal relaxation rate ($i = 2$), T_{iW} is the bulk relaxation rate in the absence of ions and T_{iP} is the paramagnetic contribution. The second part of Eq. 2.13 defines the relaxation rates $R_{i,0} = 1/T_{iW}$, i.e. the inverse of the relaxation time, as well as the paramagnetic ion molartiy c_p and the relaxivity r_i .

A paramagnetic ion dissolved in an aqueous solution will form a coordination complex with H_2O molecules as ligands and the ion as the coordination center [48]. In such a case only the ligands will experience the relaxation due to the electronic spin [46] and the paramagnetic relaxation contribution is given by Eq. 2.14, [47].

$$\frac{1}{T_{iP}} = \frac{c_p}{c_w} \cdot \frac{q}{T_{iL} + \tau_M} \quad (2.14)$$

In Eq. 2.14 the mean residence lifetime of a ligand molecule is denoted by τ_M , c_w is the molarity of water, q is the number of bound ligands and T_{iL} is the relaxation time for the bound ligands. Those two relaxation times T_{1L} and T_{2L} were already calculated above, Eq. 2.11. It would also be possible to calculate the relaxation rates T_{1W} and T_{2W} from Eq. 2.13 with the same procedure as before. Those relaxation rates define the case of a homo-nuclear system, so the transition W_0 in Eq. 2.8 would give zero. For the remaining two transition rates W_1 and W_2 one can still use Eq. 2.10 for $\omega_I = \omega_S$ and plug them into Eq. 2.8.

2.3 NMR Probe Circuit Design

To understand the behavior of a NMR probe it is helpful to have a basic understanding of a few radio frequency (RF) technology aspects. In general a RF system consists out of a signal source, a signal load and a transmission line connected in between. Standard RF components possess $50\ \Omega$ ports, i.e. the device in- and outputs behave like a resistor with a real-only $50\ \Omega$ impedance. The maximum power transfer theorem states that for a RF system the highest power transmission from a source to a load occurs, when the source and the load have mutually complex conjugated impedances [49]. Standard systems fulfill this since both, source and load are $50\ \Omega$ matched.

Though, in general this is not fulfilled for a sole NMR coil. Such a probe typically has a complex impedance Z , i.e. an inductance L along with some parasitic ohmic resistance R . The ratio between the imaginary and real part of Z define the quality or Q-factor, Eq. 2.15.

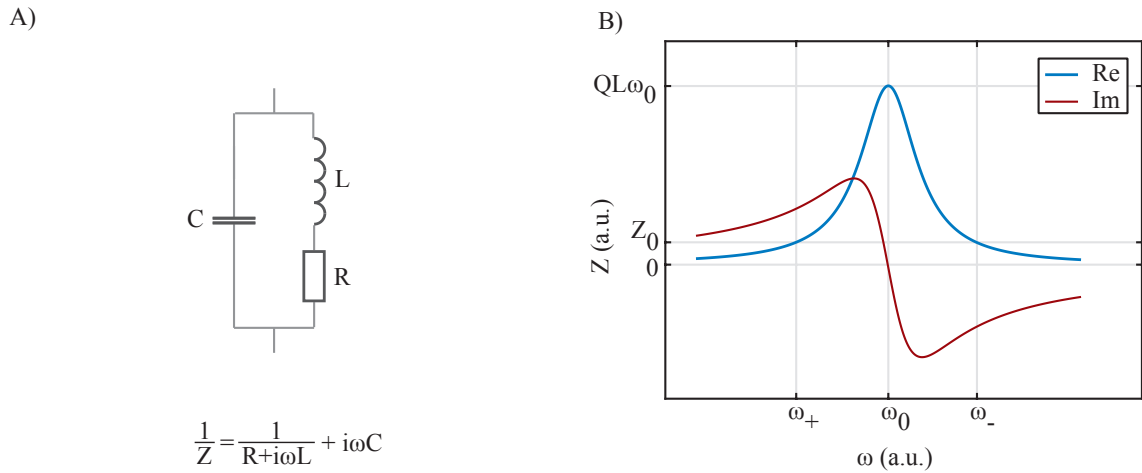


Figure 2.5: A) Tank circuit. B) Complex impedance of a tank circuit.

$$Q = \frac{\omega L}{R} \quad (2.15)$$

In Fig. 2.5 A) a parallel circuit of a NMR probe and a capacitor is shown along with an expression for its overall complex impedance [50]. The capacitor is supposed to be lossless. Frequently such a circuit is also called a tank circuit. The complex impedance of this tank circuit is plotted in Fig. 2.5 B). The real part's maximum is located at ω_0 with a value of $QL\omega_0$ (assumed that $Q \gg 1$). At an angular velocity ω_+ the real part is equal to some defined impedance $Z_0 = 50 \Omega$ with a non-vanishing positive imaginary part.

When a NMR coil is supposed to excite the nuclear magnetization a high power pulse must get fed to the coil. Hence, to achieve a maximum power transfer the coil must get impedance matched to 50Ω . To accomplish this, in Fig. 2.6 A) a standard NMR probe matching circuit is presented (the parasitic resistance is omitted). Basically it consists out of a tank circuit with an accompanying serial matching capacitor C_M . The tuning capacitor C_T is chosen in such a way that it forms with the probe impedance a resonant circuit with ω_+ located at the angular Larmor velocity. The matching capacitor C_M cancels the remaining imaginary part.

When high voltages are applied to the NMR coil, parasitic capacitances can build up between the coil and the inserted sample. Those capacitances lead to dielectric losses which will degrade the Q-factor of the circuit [50]. A symmetric scheme as shown in Fig. 2.6 B) can attenuate those losses [51]. The matching capacitance C_M got doubled and an additional symmetrizing capacitor C_S is connected between the NMR coil and ground. In case that $C_S = 2C_M$ a virtual ground will emerge in the coil center, i.e. the applied voltages will get halved, and the dielectric losses will get attenuated.

Finally in Fig. 2.6 C) a symmetric impedance matching circuit with an active decoupling functionality [52, 53] is shown. The design is based on a PIN diode denoted with P and a decoupling coil denoted with L_D in the schematic. In contrast to ordinary pn-diodes, a PIN

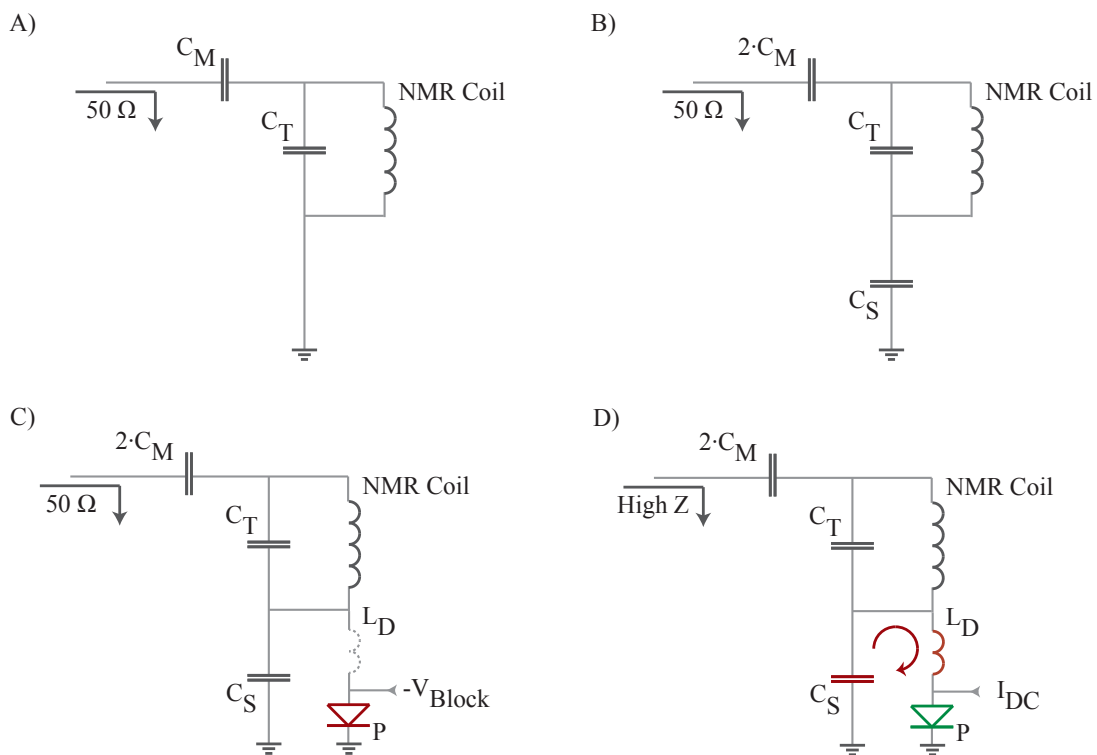


Figure 2.6: A) Single-ended impedance matching circuit for NMR probes. B) Symmetric impedance matching circuit. C) Symmetric circuit with active decoupling functionality turned off. D) Decoupling functionality turned on.

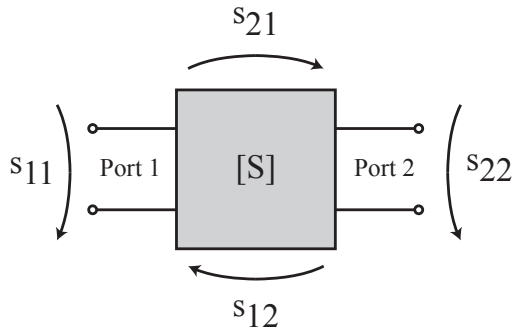


Figure 2.7: Schematic depiction of the scattering matrix $[S]$ for a 2-port device.

diode has a third undoped (intrinsic) region between its p-doped and its n-doped layer [54]. One can regard a PIN diode as a tunable RF resistance. Through an external DC current it is possible to dynamically adjust the number of charge carriers in the intrinsic region. When such an external current is applied, i.e. the undoped region is flooded with carriers, the PIN diode will conduct in the RF regime. When the external current is turned off and a negative blocking voltage is applied, i.e. the undoped region is nearly free of charge carriers, it will behave like a high resistance in the RF regime. The latter case is shown in Fig. 2.6 C), a blocking voltage is applied, the PIN diode P is in a high impedance state and the impedance matching circuit is equivalent to Fig. 2.6 B).

In Fig. 2.6 D) the decoupling case is shown. The PIN diode is brought into a conducting state and L_D forms a tank circuit with C_S . When the inductance of the decoupling coil is matched to C_S at the Larmor frequency the resulting high impedance block will switch away the whole NMR probe circuit [50].

Quantitatively the matching of a NMR probe and the RF behavior of any electric component can be characterized by the scattering matrix $[S]$. For a 2-port network like it is depicted in Fig. 2.7 this is a 2x2 matrix [55]. In case of a symmetric and reciprocal network this simplifies further with $s_{11} = s_{22}$ and $s_{21} = s_{12}$ [56]. And in case of a one-port network, e.g. a NMR coil, the matrix has got only a single entry s_{11} . The parameter s_{11} quantifies how much of a RF signal generated by a $50\ \Omega$ source will get reflected when entering port 1 whereas the parameter s_{21} quantifies the portion of a RF signal entering port 1 and appearing at port 2 when both, source and load have $50\ \Omega$.

2.4 Signal-to-Noise Ratio of a NMR Experiment

In the last paragraph the signal-to-noise ratio (SNR) should be analyzed qualitatively. In an NMR experiment, after a pulse with flip angle α , the M_{xy} component of a macroscopic magnetic moment, Eq. 2.3, rotates with the Larmor frequency, Eq. 2.5, in a coil. With

respect to Faraday's law of induction this causes a voltage in the coil proportional to the magnitude of the magnetization and to the Larmor frequency. Hence, with respect to Eq. 2.3, the signal has a proportionality as shown in Eq. 2.16.

$$\omega_L M_{xy} \propto \sin(\alpha) N \gamma^3 B_0^2 \quad (2.16)$$

In an NMR experiment there are several noise sources [57]. Most noticeably is the thermal noise given by Eq. 2.17 for the time domain [50].

$$\sqrt{4kT\Delta f \xi R} \quad (2.17)$$

Here Δf gives the bandwidth of the investigated signal and R the ohmic resistance of the coil conductor. This resistance gets increased by a factor ξ . This factor takes the proximity effect into account, i.e. the mutual interference of closely placed wires. The skin effect, i.e. the effectively decreased conductor cross section for RF signals, is already included in R . In their work Hoult and Richards [33] analyzed the SNR of a NMR experiment in detail. They introduced the so-called principle of reciprocity. This principle states that a coil with good excitation capabilities, i.e. the coil generates a high B_1 field for a given current I_0 , has also good receiver capabilities. For that reason a factor $\frac{B_1}{I_0}$ must get considered which leads to a qualitative expression for the SNR of a NMR experiment, Eq. 2.18.

$$SNR \propto \frac{B_1 \sin(\alpha) N \gamma^3 B_0^2}{I_0 \sqrt{4kT\Delta f \xi R}} \quad (2.18)$$

Besides that, like described in [58], the proportionality with $B_1/I_0\sqrt{R}$ can be replaced by a proportionality with $\sqrt{\eta Q}$ where η is the filling factor and Q is the quality factor of the setup. The filling factor accounts for ratio of the sensitive coil volume filled with a sample to the overall sensitive volume. In conclusion from a probe design perspective it is equivalent to optimize the excitation properties of a coil, i.e. B_1/I_0 , or to optimize the filling factor η in conjunction with the quality factor Q .

3 Analysis of 2D Relaxation Data using Chisholm Approximations

In this chapter the development of a new algorithm for the analysis of 2D NMR relaxation data will be presented. The results were published in [59]. At the beginning a detailed mathematical examination of the algorithm is given. The basic idea is to approximate the 2D Laplace image of the experimental dataset with a 2D rational polynomial, a so-called Chisholm approximation. To validate the algorithm, it was tested with simulated and experimental data. Besides validation the outcome is also compared to the state-of-the-art method. Both outcomes, validation and comparison, are given in the results section followed by a concluding discussion.

3.1 Algorithm

In general a two dimensional relaxation signal is a function of two independent variables which are called the direct and indirect or the first and the second dimension. In case that T_1 or T_2 is investigated, the particular dimension corresponds to time. Here the direct and indirect dimension in the experimental domain is denoted as t_1 and t_2 respectively.

Exemplified for a T_2 - T_2 experiment, Eq. 3.1 gives the analytical time domain signal $S(t_1, t_2)$. The direct and indirect transversal relaxation rates are R_{2_i} and R_{2_j} respectively. Those relaxation rates are weighted with the relaxation amplitudes r_{ij} . The noise contribution is omitted for clarity.

$$S(t_1, t_2) = \sum_{i,j} r_{ij} e^{-R_{2_i} t_1} e^{-R_{2_j} t_2} \quad (3.1)$$

All R_{2_i} and R_{2_j} as well as the weights r_{ij} define the relaxation map $M(a_1, a_2)$, Eq. 3.2, as a function of the direct and indirect relaxation dimension a_1 and a_2 .

$$M(a_1, a_2) = \sum_{i,j} r_{ij} \delta(a_1 - R_{2_i}) \delta(a_2 - R_{2_j}) \quad (3.2)$$

This map $M(a_1, a_2)$ contains the correlation and distribution of the different relaxation compartments. By that it gives physical insight and hence is the requested quantity of interest for 2D relaxation experiments. Now Eq. 3.3 shows how the experimental signal $S(t_1, t_2)$ can be regarded as the result of 2D Laplace transform \mathcal{L}_2 of such a relaxation map $M(a_1, a_2)$.

$$S(t_1, t_2) = \mathcal{L}_2 [M(a_1, a_2)] (t_1, t_2) = \int_0^\infty \int_0^\infty da_1 da_2 M(a_1, a_2) e^{-a_1 t_1} e^{-a_2 t_2} \quad (3.3)$$

Vice versa, to compute the desired relaxation map $M(a_1, a_2)$ from the experimental time domain signal one must carry out the numerical 2D inverse Laplace transform of $S(t_1, t_2)$. To accomplish this, the so called Tikhonov regularization method is applied in most cases [60]. With this method the time domain signal gets analyzed with least square procedures and a smooth fit gets calculated. In contrast to that the algorithm developed in this work does not investigate the time domain signal, Eq. 3.1, directly but rather computes another 2D forward Laplace transform \mathcal{L}_2 like illustrated in the flowchart in Fig. 3.1 A). The resulting Laplace image $G(x, y)$ of $S(t_1, t_2)$ has got the form of Eq. 3.4 and is a function of x and y , which are again denoted as direct and indirect relaxation dimensions.

$$G(x, y) = \mathcal{L}_2 [S(t_1, t_2)] (x, y) = \sum_{i,j} \frac{r_{ij}}{(x + R_{2i})(y + R_{2j})} \quad (3.4)$$

With respect to Eq. 3.1 and Eq. 3.4 it is clear that the determination of all relaxation rates and amplitudes of Eq. 3.1, i.e. the calculation of the relaxation map, is equivalent to the determination of all poles and residues of $G(x, y)$ in Eq. 3.4.

To do so, Eq. 3.4 gets approximated for x and y around a point (x_0, y_0) with a two dimensional rational polynomial of order $\langle M - 1/M \rangle$ where $M - 1$ is the highest order in the nominator and M is the highest order in the denominator. The general form of such a multivariate rational polynomial approximation, Eq. 3.5, is called a Chisholm approximation [16, 17].

$$\frac{\sum_{\mu, \nu=0}^{M-1} a_{\mu\nu} x^\mu y^\nu}{1 + \sum_{\substack{\sigma, \tau=0 \\ \sigma+\tau \geq 1}}^M b_{\sigma\tau} x^\sigma y^\tau} \quad (3.5)$$

Due to its rational form one can easily find the poles χ_i and γ_j of the Chisholm approximation by looking for the zeros of the denominator function along x and y . Those poles will span a grid over the two dimensional relaxation domain which is also illustrated in Fig. 3.1 B) for an exemplary Laplace image with two poles $\chi_{1,2}$ and $\gamma_{1,2}$ along the direct and indirect dimension and two residues r_{11} and r_{22} .

Whenever there is a crossing of a direct and an indirect grid line one can calculate the residue at that point by evaluating the rational approximation multiplied with $(x + \chi_i)(y + \gamma_j)$ at the given pole coordinate. Whenever the crossing belongs to an existing relaxation compartment the multiplication factor from before will zero all fractions in Eq. 3.4 except that one belonging to the pole under investigation. Because within this particular fraction the multiplication factor will cancel with the denominator and the residue r_{ij} will emerge. How-

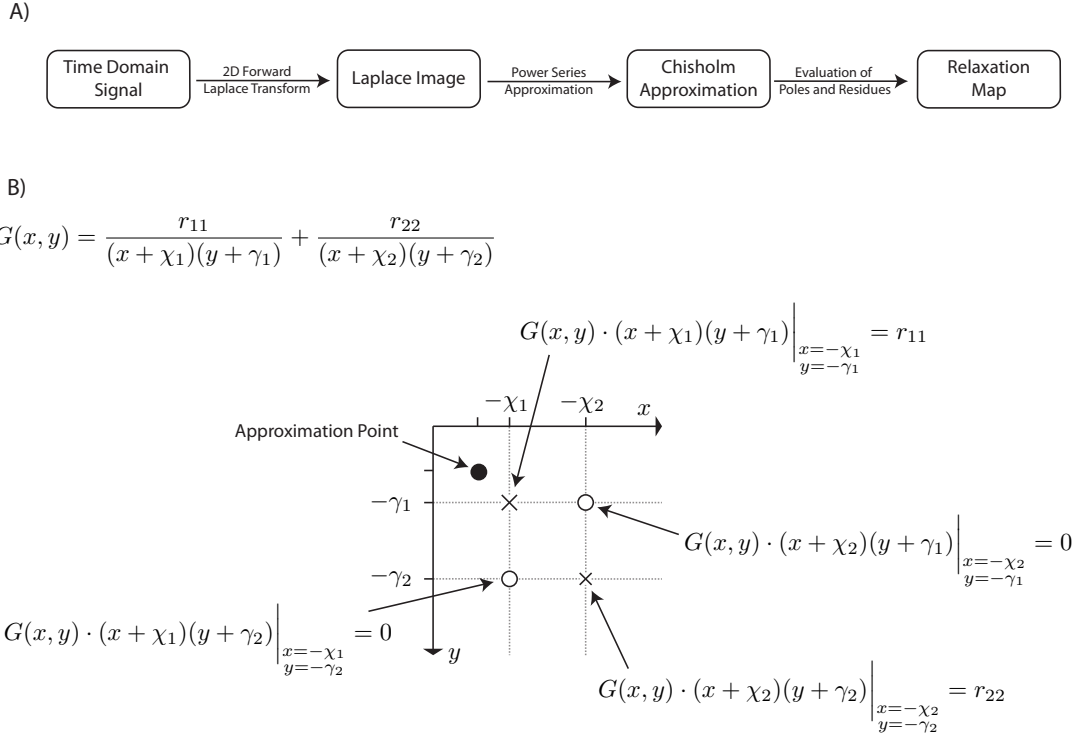


Figure 3.1: A) The flowchart of the Chisholm approximation method. B) The grid defined by the poles of $G(x, y)$ along with the residues and the corresponding evaluation.

ever when the crossing of a grid line does not belong to an existing relaxation compartment in the signal, the multiplication factor will not get canceled and the evaluation of the rational approximation at the pole coordinate will give zero.

Each relaxation component present in the time domain signal $S(t_1, t_2)$ is represented by such a pair of poles and a residue in the 2D Laplace image. For this reason one needs to calculate the Chisholm approximation up to an order $\langle N - 1/N \rangle$ where N is the number of poles along the relaxation dimension with the maximum number of poles. When N is unknown an incrementation procedure must get applied, i.e. the approximation order $\langle M - 1/M \rangle$ of the Chisholm approximation gets stepwise increased and the poles and residues get calculated for each M . It is supposed that either unreasonable high or negative poles emerge or residues with an imaginary part will occur when $M > N$. With that conditions in mind one can abort the incrementation of the approximation [61].

To proceed it is necessary to calculate the Chisholm approximation coefficients $a_{\mu\nu}$ and $b_{\sigma\tau}$. For an approximation of order $\langle M - 1/M \rangle$ there are $2M^2 + 2M$ unknowns. In order to determine those, a power series approximation of $G(x, y)$ with its associated coefficients c_{nk} gets calculated around an evaluation point x_0 and y_0 . By equating the power series approximation with the Chisholm approximation, Eq. 3.6, a set of equations gets deduced

which allows the calculation of the Chisholm approximation coefficients $a_{\mu\nu}$ and $b_{\sigma\tau}$ out of c_{nk} . A detailed description of this is given in [16, 17].

$$G(x, y) \approx \sum_{n,k=0} c_{nk} (x - x_0)^n (y - y_0)^k = \frac{\sum_{\mu,\nu=0}^{M-1} a_{\mu\nu} (x - x_0)^\mu (y - y_0)^\nu}{1 + \sum_{\substack{\sigma,\tau=0 \\ \sigma+\tau \geq 1}}^M b_{\sigma\tau} (x - x_0)^\sigma (y - y_0)^\tau} \quad (3.6)$$

It is important to note that the power series coefficients c_{nk} can be described by the two dimensional Taylor series of Eq. 3.4 around x_0 and y_0 . This is shown in Eq. 3.7 where $G(x_0, y_0)^{(n,k)}$ is the n^{th} derivative along the direct relaxation dimension of $G(x, y)$ evaluated at x_0 and the k^{th} derivative of $G(x, y)$ along the indirect relaxation dimension evaluated at y_0 .

$$\begin{aligned} c_{nk} &= \frac{1}{n! k!} G(x_0, y_0)^{(n,k)} \\ &= \frac{(-1)^{n+k}}{n! k!} \sum_{i,j} r_{ij} \frac{n!}{(x_0 + R_{2_i})^{n+1}} \frac{k!}{(y_0 + R_{2_j})^{k+1}} \end{aligned} \quad (3.7)$$

Hence, in order to determine the Chisholm coefficients $a_{\mu\nu}$ and $b_{\sigma\tau}$ one needs to calculate the power series coefficients c_{nk} of the two dimensional Taylor series approximation, Eq. 3.7. This can be done by the differentiation rule, Eq. 3.8, of the two dimensional Laplace transform easily.

$$c_{nk} = \frac{(-1)^{n+k}}{n! k!} \mathcal{L}_2 \left[t_1^n t_2^k S(t_1, t_2) \right] (x_0, y_0) \quad (3.8)$$

The \mathcal{L}_2 transform itself is extended in Eq. 3.9. This integral, incorporating the experimental signal $S(t_1, t_2)$, in conjunction with the prefactors from Eq. 3.8 must get computed numerically for all necessary power series coefficients c_{nk} .

$$\mathcal{L}_2 \left[t_1^n t_2^k S(t_1, t_2) \right] (x_0, y_0) = \int_0^\infty \int_0^\infty dt_1 dt_2 t_1^n t_2^k S(t_1, t_2) e^{-x_0 t_1} e^{-y_0 t_2} \quad (3.9)$$

In the previous paragraph it was explained how one can determine all relaxation rates and amplitudes of a signal from a T_2 - T_2 experiment. Due to the equivalent analytical form of a T_2 - D signal this method can also be applied to the analysis of the experiments where the transversal relaxation rate T_2 is measured against the diffusion coefficient D . However, when T_1 is stored along a dimension of the relaxation data a preprocessing stage must get included. In case T_1 is measured with an IR sequence the analytical form of the signal is given in Eq. 3.10. Here R_{1_j} denote the longitudinal relaxation rates. The noise contribution is again omitted for clarity.

$$S(t_1, t_2) = \sum_{i,j} r_{ij} e^{-R_{2i} t_1} (1 - 2e^{-R_{1j} t_2}) \quad (3.10)$$

To get the underlying relaxation map out of Eq. 3.10 one can either subtract the signal from its equilibrium state of the indirect dimension, i.e. one must calculate $\frac{1}{2}(S(t_1, t_2 \rightarrow \infty) - S(t_1, t_2))$ like it is for example done in [62] and subsequently apply the algorithm as described above. Or, due to the linearity of the Laplace transform, one can also perform this in the Laplace image of Eq. 3.10. The power series coefficients of the Laplace image, denoted as d_{nk} here, are given in Eq. 3.11. Within the sum of Eq. 3.11 the first fraction corresponds to the direct dimension and the brackets in the sum correspond to the indirect dimension.

$$\begin{aligned} d_{nk} &= \frac{1}{n! k!} G(x_0, y_0)^{(n,k)} \\ &= \frac{(-1)^{n+k}}{n! k!} \sum_{i,j} r_{ij} \frac{n!}{(x_0 + R_{2i})^{n+1}} \left(\frac{k!}{y_0^{k+1}} - \frac{2k!}{(y_0 + R_{1j})^{k+1}} \right) \end{aligned} \quad (3.11)$$

A careful comparison of Eq. 3.11 with Eq. 3.7 shows that d_{nk} can get transformed into c_{nk} . Therefore one must calculate the fraction in Eq. 3.11 corresponding to the direct dimension independently. Basically this is the one dimensional Laplace transform of $S(t_1, t_2 \rightarrow \infty)$ like it is shown in Eq. 3.12.

$$p_n = \frac{(-1)^n}{n!} \int_0^\infty dt_1 t_1^n S(t_1, t_2 \rightarrow \infty) e^{-x_0 t_1} = (-1)^n \sum_i \frac{1}{(x_0 + R_{2i})^{n+1}} \quad (3.12)$$

With this in mind one can transform Eq. 3.11 into Eq. 3.7 by Eq. 3.13.

$$c_{nk} = \frac{1}{2} \left[\frac{(-1)^k}{y_0^{k+1}} \cdot p_n - d_{nk} \right] \quad (3.13)$$

To conclude it is important to note that both T_1 - T_2 preprocessing methods in the way they are described here, require a proper normalization of the time domain signal, i.e. $\sum_{i,j} r_{ij} = 1$.

3.2 Methods

3.2.1 Simulation

To demonstrate the feasibility of the algorithm and compare it with the Tikhonov regularization method, two different simulations were performed.

In a first step the time domain signal of a T_2 - T_2 experiment with the relaxation map listed in Tab. 3.1 got simulated. The inset of this table shows the relaxation amplitudes r_{ij} like defined in Eq. 3.1. The inset rows correspond to the direct relaxation dimension, the inset

columns to the indirect dimension respectively. The associated relaxation rates are given in the right-hand column and in the bottom row.

| r_{ij} | \rightarrow | | | R_{2_i} (1/s) |
|-----------------|---------------|-----|-----|-----------------|
| \downarrow | 0.3 | 0.1 | – | 1 |
| | 0.1 | 0.2 | – | 3 |
| | – | – | 0.3 | 7 |
| R_{2_j} (1/s) | 1 | 3 | 7 | |

Table 3.1: The discrete relaxation map for the T_2 - T_2 simulation with three compartments. Two compartments are exchanging, one compartment is isolated.

The map had three relaxation compartments located at 1 s^{-1} , 3 s^{-1} and 7 s^{-1} with corresponding amplitudes of 0.3, 0.2 and 0.3. Furthermore an exchange between the two compartments with 1 s^{-1} and 3 s^{-1} was introduced. The amplitudes of the symmetric exchange peaks were 0.1. The compartment with a relaxation rate of 7 s^{-1} was isolated and non-exchanging. In the time domain the data consisted of 1024 echos in each dimension and had an echo spacing of 5 ms. The dataset was simulated for 10 different SNRs logarithmically spaced between 10 and 10 000 whereas SNR is defined by the maximum signal amplitude divided by the standard deviation of the noise floor [60]. For every given SNR 16 simulations were performed and subsequently 2D Laplace inversions based on the Chisholm approximation and based on the Tikhonov regularization method were applied. Since the relaxation map contained three separated compartments the calculated Chisholm approximation order was $\langle 2/3 \rangle$.

In order to compare the results of the Tikhonov regularization and Chisholm approximation method the χ^2 distance, Eq. 3.14, between the respective outcome F and the simulated input relaxation map M was computed. To do so, the simulated relaxation map and the results of the Chisholm approximation method were regridded to the relaxation rates defined by the Tikhonov regularization kernel.

$$\chi^2 = \sum_{i,j} \frac{(F_{ij} - M_{ij})^2}{F_{ij} + M_{ij}} \quad (3.14)$$

In case that for a given matrix element (i, j) both relaxation maps, F_{ij} and M_{ij} , contained a zero, the contribution of that element to the sum in Eq. 3.14 was nulled.

In a second simulation the time domain signal of a T_1 - T_2 experiment - the underlying relaxation map did not contain discrete delta-like peaks but rather continuous distributions with a defined width σ - was computed. The relaxation map had three symmetric Gaussian compartments like listed in Tab. 3.2. The echo time was 1 ms and 2500 echoes were employed. The indirect dimension was sampled with 300 inversion times linearly spaced between 0 s and 2.5 s. The SNR was set to 500.

| Compartment | R_1 (1/s) | R_2 (1/s) | σ (1/s) | integral (a.u.) |
|-------------|-------------|-------------|----------------|-----------------|
| 1 | 2 | 5 | 0.025 | 0.25 |
| 2 | 6 | 10 | 0.05 | 0.45 |
| 3 | 15 | 20 | 0.01 | 0.30 |

Table 3.2: The distribution parameters for the T_1 - T_2 simulation.

For the inversion with the Chisholm approximation method it was supposed that the number of relaxation compartments is unknown. Therefore the incrementation procedure like described in the previous section was applied and the approximation order got stepwise increased from $\langle 0/1 \rangle$ to $\langle 3/4 \rangle$. To cope with the T_1 - T_2 decay the preprocessing method in the Laplace image of $S(t_1, t_2)$, also like described earlier, was employed.

3.2.2 Experiment

In a last step the resolution limit of the algorithm with experimental T_1 - T_2 data was investigated and compared to the results of the Tikhonov regularization method. Therefore four samples, each consisting of two separated compartments, got produced. One compartment always contained 100 μl of a 11.2 mM Cu^{2+} solution filled into a 10 mm NMR tube. The other compartment also contained 100 μl of a Cu_2^+ solution but with an increasing concentration of Cu_2^+ logarithmically spaced between 11.2 mM and 33.7 mM. Those samples got filled into a smaller plastic container which got inserted into the 10 mm tube. The Cu^{2+} solutions were produced by dissolving CuSO_4 salt in bidistilled water. All experiments were performed with a 0.5 T MRI device from *Pure Devices* (Wuerzburg, Germany) shown in Fig. 3.2 A). The device had typical 90° pulse lengths in the range of 45 μs . The T_1 and T_2 relaxation times of all employed concentrations were determined with one-dimensional IR and CPMG sequences respectively by 10 independent measurements. After that the four double compartment samples, shown in Fig. 3.2 B), were analyzed with a two dimensional IR-CPMG sequence. Within this work the employed 1D and the 2D sequences were specifically implemented for the MRI device with *MATLAB* from *MathWorks* (Natick, USA). Each sample got measured 10 times with 100 inversion times linearly spaced up to 0.75 s and with 150 echoes separated by an echo time of 5 ms. To analyze the T_1 - T_2 data, this time the preprocessing stage in the time domain was applied, i.e. a direct dimension from the signal measured with an inversion time of 1 s was subtracted. For the Chisholm method, the calculated approximation order was $\langle 1/2 \rangle$.

3.2.3 Implementation

Both, the Tikhonov regularization and the Chisholm approximation methods were implemented in *MATLAB*. To perform a 2D inverse Laplace transform based on the Tikhonov

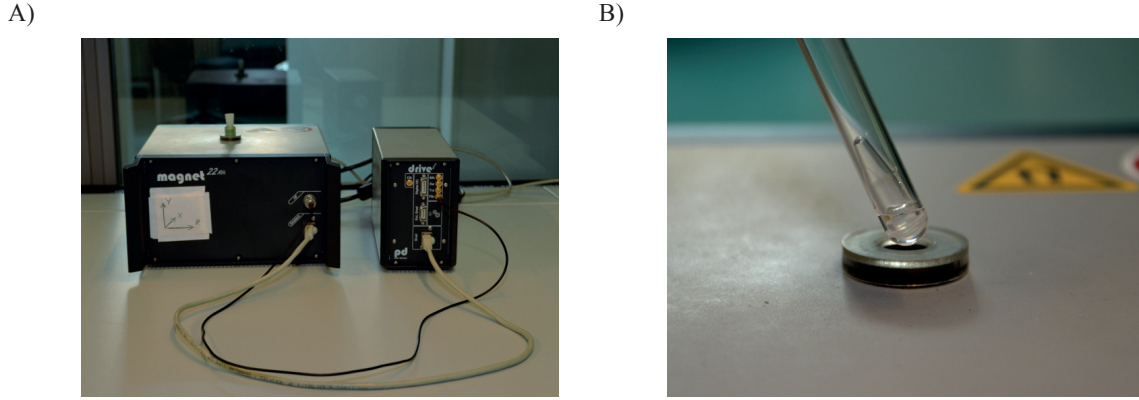


Figure 3.2: Experimental setup. A) The portable 0.5 T MRI system from *Pure Devices* with the 10 mm NMR tube inserted in the magnet. B). Close-up of the 10 mm tube and the inserted container showing both sample compartments.

regularization method it is necessary to solve the numeric problem stated in Eq. 3.15 incorporating the kernel matrix K .

$$\mathbf{F} = \arg \min_{F \geq 0} \|\mathbf{S} - \mathbf{KF}\|^2 + \alpha \|\mathbf{F}\| \quad (3.15)$$

To do so, Eq. 3.15 got transformed into a quadratic programming problem (QPP) like described in [60] and solved with *MATLAB*. To optimize the smoothing parameter α the Butler-Reeds-Dawson (BRD) method was applied as described in [42]. This method solves Eq. 3.15 for several decreasing α and investigates the fitting error χ between the experimental signal and the fitted result for all solutions as a function of α . The optimized smoothing parameter is chosen to be the first α which fulfills $d(\log_{10}\chi)/d(\log_{10}\alpha) \leq \text{TOL}$ [63]. Thereby TOL is some tolerance value predefined by the user within the range $0 \leq \text{TOL} \leq 0.1$ [60]. Due to the discrete nature of the relaxation maps the TOL value was set to 0.05. In all cases the inversion results F had a size of 32×32 based on logarithmically spaced relaxation rates in the range from 0.1 s^{-1} to 100 s^{-1} .

To calculate the core integral in Eq. 3.9 of the Chisholm approximation method the trapezoidal rule was employed in conjunction with a preceding spline interpolation and an interpolation factor of 5 for T_2 -like dimensions and with a factor of 10 for T_1 -like dimensions. To determine an approximation point for a T_2 -like dimension the inverse point in time was chosen, when the signal decayed to half of its initial amplitude. In case the dimension had a T_1 -like behavior based on an IR sequence the inverse point in time was used, when the signal had its zero crossing.

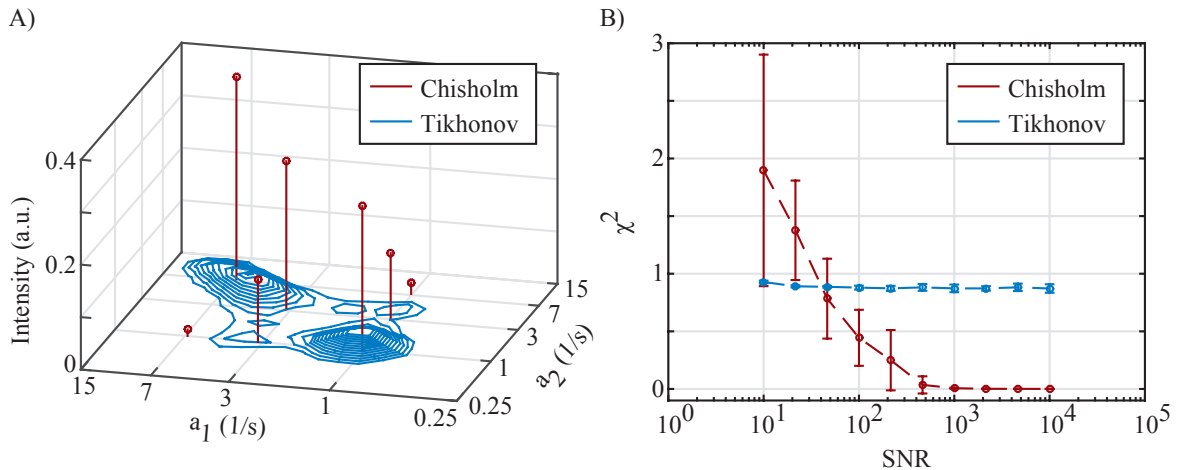


Figure 3.3: Results of the simulated T_2 - T_2 inversion. A) Typical outcome of the Chisholm approximation (stems) and Tikhonov regularization (contour) method applied to a dataset with a SNR of 100. B) The χ^2 distance between the inversion outcome of both methods and the simulated input data as a function of SNR.

3.3 Results

3.3.1 Simulation

For the first simulated relaxation map from Tab. 3.1 a typical delta-like outcome of the Chisholm approximation method is depicted with stems in Fig. 3.3 A). The detected compartments are located at 1.00 s^{-1} , 3.16 s^{-1} and 7.27 s^{-1} for the direct dimension and at 1.01 s^{-1} , 3.16 s^{-1} and 6.80 s^{-1} for the indirect dimension respectively. The relaxation amplitudes on the diagonal were 0.28, 0.28 and 0.39 for increasing relaxation rates. The exchange peaks between the 1 s^{-1} and 3 s^{-1} relaxation compartments were 0.12. The two artifacts visible as exchange peaks between the 1 s^{-1} and 7 s^{-1} had amplitudes of 0.01 and 0.02. No exchange peaks occurred between the 3 s^{-1} and 7 s^{-1} compartments. Additionally shown in Fig. 3.3 A) is the continuous distribution which one gets with the Tikhonov regularization method. The x and y axes of Fig. 3.3 A) show the direct and indirect transversal relaxation rate a_1 and a_2 respectively. In this case the SNR of time domain input signal was 100. As a guide to the eye, the grid lines in the $x - y$ plane show the relaxation rates of the simulated compartments. It took 54s to generate this result with the Chisholm approximation method. For the Tikhonov regularization method the processing time on the same workstation was 224s taking the optimization of the smoothing parameter α not into account.

For each simulated dataset the approximation points x_0 and y_0 for the Chisholm approximation method were estimated separately. The mean was around 3.9 s^{-1} for both dimensions. The standard deviation of the approximation points was nearly 0 s^{-1} for the highest investigated SNR and increased to 0.2 s^{-1} for the lowest SNR.

To perform the Tikhonov regularization inversion for all given samples, α also got optimized for low and medium SNRs. The smoothing parameters increased from 0.001 to 100 with decreasing SNR. For SNRs > 1000 the smoothing was attenuated by defining $\alpha = 0.001$ without the BRD optimization. For the result exemplified in Fig. 3.3 the smoothing parameter α was 0.1.

To compare the inversion outcome of the Tikhonov regularization and Chisholm approximation methods the χ^2 difference between the inversion result of both methods and the simulated relaxation map was calculated for all 10 investigated SNRs and for all 16 runs. In Fig. 3.3 B) the mean and standard deviation of χ^2 as a function of SNR is shown for the Tikhonov regularization and Chisholm approximation method.

To analyze the data of the second simulation, Tab. 3.2, as a first step the smoothing parameter α was optimized for the Tikhonov regularization method and the approximation point for the Chisholm approximation method was estimated. The optimized smoothing parameter was found to be 0.01, the two Chisholm approximation points were given by $x_0 = 15.6 \text{ s}^{-1}$ and $y_0 = 9.3 \text{ s}^{-1}$ for the direct and indirect dimension respectively. Since it was supposed that the number of relaxation compartments is unknown the inversion order of the Chisholm approximation was stepwise increased. In Tab. 3.3 the results for this incrementation procedure is shown for all four investigated approximation orders. The table is grouped into four rows. Each row represents an approximation order ranging from $\langle 0/1 \rangle$ to $\langle 3/4 \rangle$. Furthermore the rows have got a 4×4 table inset which contains the relaxation amplitudes resulting for a given approximation order. Hence the inset for the approximation order $\langle 0/1 \rangle$ shows one relaxation amplitude, the inset for the approximation order $\langle 1/2 \rangle$ shows four relaxation amplitudes and so on. The entry (i, j) of every inset corresponds to the i^{th} transversal relaxation rate shown on the right hand side of the inset and to the j^{th} longitudinal relaxation rate shown below the inset. Residues which were less or equal zero were discarded for clarity.

In Fig. 3.4 a comparison between the Chisholm approximation method and the Tikhonov regularization method is shown. Here Chisholm approximation result for the approximation order $\langle 2/3 \rangle$ is plotted. The grid lines on the axis for the longitudinal and transversal relaxation rate are in correspondence with Tab. 3.2 and serve again as a guide to the eye.

3.3.2 Experiment

To analyze the experimental data, as a first step the one dimensional calibration curves of all five CuSO_4 samples were evaluated with mono-exponential fits. Tab. 3.4 lists the mean longitudinal and transversal relaxation rates along with the standard deviation of the samples. Furthermore the corresponding Cu^{2+} concentration with the associated sample number in roman letters is shown.

Those relaxation rates are the benchmark test for the resolution analysis of the T_1 - T_2 relaxation experiments where the samples I to IV were combined with sample V. That means,

| Approximation Order | Poles and Residues | | | | | |
|-----------------------|--------------------|---------------|-------|------|-------------|--------|
| $\langle 0/1 \rangle$ | r_{ij} | \rightarrow | | | R_2 (1/s) | |
| | \downarrow | | | | | |
| | | | 1.00 | | 8.49 | |
| | R_1 (1/s) | | | | 4.64 | |
| $\langle 1/2 \rangle$ | r_{ij} | \rightarrow | | | R_2 (1/s) | |
| | \downarrow | | | | | |
| | | | 0.25 | 0.23 | 15.86 | |
| | | | 0.28 | 0.24 | 5.94 | |
| | | R_1 (1/s) | 10.62 | 2.61 | | |
| $\langle 2/3 \rangle$ | r_{ij} | \rightarrow | | | R_2 (1/s) | |
| | \downarrow | | | | | |
| | | 0.27 | – | 0.01 | 19.36 | |
| | | 0.03 | 0.43 | – | 9.50 | |
| | | – | – | 0.25 | 4.89 | |
| | R_1 (1/s) | 15.01 | 6.00 | 1.99 | | |
| $\langle 3/4 \rangle$ | r_{ij} | \rightarrow | | | R_2 (1/s) | |
| | \downarrow | – | 0.02 | 0.04 | 0.02 | -48.10 |
| | | – | 0.27 | – | – | 20.39 |
| | | – | 0.01 | 0.40 | – | 10.28 |
| | | – | – | 0.02 | 0.24 | 5.05 |
| | R_1 (1/s) | -3.19 | 15.41 | 6.49 | 2.28 | |

Table 3.3: Inversion outcome of the Chisholm approximation method as a function of the approximation order for an input signal based on Tab. 3.2.

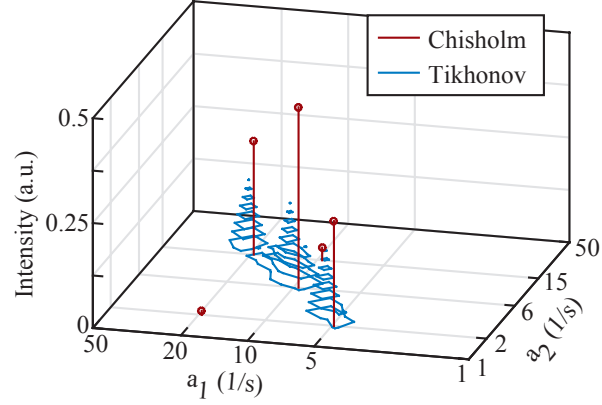


Figure 3.4: The inversion results of the Chisholm approximation (stems) and Tikhonov regularization (contour) methods applied to a signal based on the relaxation map from Tab. 3.2.

| Sample | Concentration (mM) | R_1 (1/s) | R_2 (1/s) |
|--------|--------------------|------------------|------------------|
| I | 33.7 | 29.36 ± 1.09 | 32.84 ± 0.49 |
| II | 25.6 | 22.83 ± 0.68 | 25.50 ± 0.18 |
| III | 19.4 | 17.32 ± 0.32 | 19.20 ± 0.22 |
| IV | 14.7 | 13.17 ± 0.42 | 14.65 ± 0.05 |
| V | 11.2 | 10.28 ± 0.30 | 11.47 ± 0.12 |

Table 3.4: The one dimensional relaxation rates of the five investigated CuSO_4 solutions.

the relaxation rates of the two compartments present in the combined sample had a mean ratio of 2.9, 2.2, 1.7 and 1.3 for increasing sample number of the first compartment. The experimental data of the combined T_1 - T_2 relaxation curves had an average SNR in the range of 750. For the Chisholm approximation the estimation of the approximation point for the direct dimension x_0 had a mean of 29.7 s^{-1} , 26.1 s^{-1} , 22.2 s^{-1} and 19.1 s^{-1} and for the indirect dimension y_0 a mean of 27.5 s^{-1} , 23.9 s^{-1} , 20.4 s^{-1} and 17.5 s^{-1} , listed again with increasing concentration of the first compartment in the sample.

Tab. 3.5 gives the results of the Chisholm approximation analysis. The table rows group the four sample pairs. The 2×2 inset in each row gives the mean relaxation amplitudes and their standard deviation. Like before, the entry (i, j) of that inset corresponds to the i^{th} transversal relaxation rate shown on the right hand side of the row and to the j^{th} longitudinal relaxation rate shown below the inset. All relaxation rates are again given by their mean and standard deviation. In doing so, residues which were less or equal to zero were discarded.

In addition to that, a Tikhonov regularization inversion was applied to each of the 10 datasets for all four samples I-V to IV-V. Therefore, also the smoothing parameter α was optimized. In all cases the optimization result was $\alpha = 0.001$. To exemplify the Tikhonov regularization result and compare it with the Chisholm approximation result Fig. 3.5 shows the inversion outcome of both methods for an arbitrary dataset. The two grid lines between 1 s^{-1} and 100 s^{-1} along the a_1 and a_2 axis represent the one dimensional calibration results from Tab. 3.4 and are a guide to the eye.

The two relaxation compartments are regarded to be resolved with the Tikhonov regularization method when both distributions do not overlap. For the Chisholm approximation method they are regarded to be resolved when the detected relaxation rates are close to the calibration results and the main diagonal shows both residues. Both the Tikhonov regularization and the Chisholm approximation were able to detect two separated relaxation compartments for all datasets with the samples I-V. For the sample II-V the Tikhonov regularization was able to separate both compartments in 9 of 10 cases, whereas the Chisholm approximation method achieved it for all 10 cases. For the measurements with sample III-V the Tikhonov regularization method detected two separated compartments in 3 cases, whereas the Chisholm approximation achieved this in 8 cases. For the IV-V sample the Tikhonov regularization and the Chisholm approximation method failed to separate the two compartments for all ten datasets.

3.4 Discussion

With the Chisholm approximation method the task of determining the relaxation rates and amplitudes of a 2D relaxation signal is separated. In the first step the relaxation rates are determined and in the second step the associated residues, i.e. the relaxation amplitudes, get calculated. A consequence of this can be seen in Fig. 3.3 A). Here all relaxation rates

| Sample Pair | Poles and Residues | | | |
|-------------|--------------------|------------------|-------------------|---------------------|
| I-V | r_{ij} | \rightarrow | | R_2 (1/s) |
| | \downarrow | 0.49 ± 0.05 | 0.02 ± 0.04 | 34.31 ± 1.06 |
| | | 0.02 ± 0.04 | 0.46 ± 0.03 | 11.56 ± 0.22 |
| | R_1 (1/s) | 30.29 ± 1.15 | 10.31 ± 0.39 | |
| II-V | r_{ij} | \rightarrow | | R_2 (1/s) |
| | \downarrow | 0.49 ± 0.05 | 0.02 ± 0.04 | 26.48 ± 0.86 |
| | | 0.04 ± 0.05 | 0.45 ± 0.04 | 11.74 ± 0.25 |
| | R_1 (1/s) | 22.61 ± 0.67 | 10.27 ± 0.42 | |
| III-V | r_{ij} | \rightarrow | | R_2 (1/s) |
| | \downarrow | 0.37 ± 0.19 | 0.11 ± 0.19 | 20.67 ± 1.30 |
| | | 0.15 ± 0.20 | 0.37 ± 0.21 | 11.77 ± 0.63 |
| | R_1 (1/s) | 17.32 ± 1.37 | 10.22 ± 0.83 | |
| IV-V | r_{ij} | \rightarrow | | R_2 (1/s) |
| | \downarrow | 0.35 ± 0.38 | 0.16 ± 0.20 | -30.37 ± 187.31 |
| | | 0.35 ± 0.36 | 0.14 ± 0.20 | 11.20 ± 2.36 |
| | R_1 (1/s) | 14.59 ± 5.93 | -1.39 ± 14.42 | |

Table 3.5: Inversion results of the Chisholm approximation method applied to the double compartment experimental data.

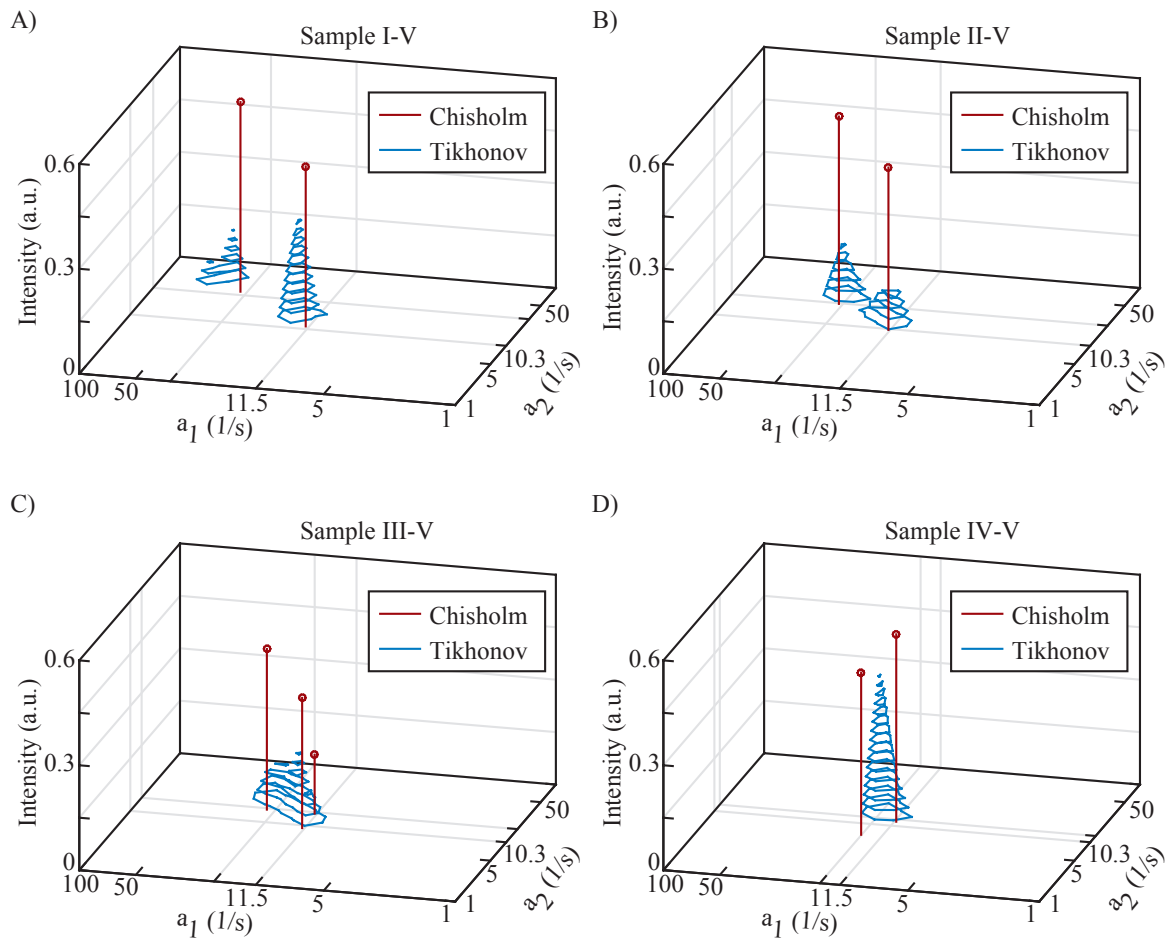


Figure 3.5: Typical inversion outcome of the Tikhonov regularization (contour) and Chisholm approximation (stems) method for all four double compartment samples. Figure parts A), B), C) and D) show inversion results of samples I-V, II-V, III-V and IV-V respectively.

get detected very accurately and one can recognize the grid structure in the relaxation map spanned by the relaxation rates of the direct and indirect dimension. However, the subsequent calculation of residues gives a non-zero relaxation amplitude between the non-exchanging compartments of 1 s^{-1} and 7 s^{-1} .

This behavior can be explained by inaccuracies in the calculation of the power series coefficients, Eq. 3.8 and Eq. 3.9. The exactness of the underlying integral with the kernel $t_1^n t_2^k S(t_1, t_2) e^{-x_0 t_1} e^{-y_0 t_2}$ is affected by several parameters, i.e. the numeric precision of the individual data points, the sampling rate of the decay curves, the noise in the experimental signal and the choice of an appropriate approximation point. To improve the accuracy of the Chisholm approximation method - independently of the experimental parameters - a first approach could be the investigation of integration methods which are less affected by noise.

Theoretically the Chisholm approximation outcome should be independent of the approximation point as long as it is valid with respect to the Laplace transform definition, i.e. the integral in Eq. 3.9 converges. For a closer inspection one can analyze the kernel for a single compartment signal with unity relaxation amplitude located at R_2 for both dimensions. The kernel for the power series coefficient c_{nk} , Eq. 3.9, of such signal has got a maximum located at $t_1 = \frac{n}{x_0 + R_2}$ and $t_2 = \frac{k}{y_0 + R_2}$. That means for an increasing approximation order and - associated with that - for a growing n and k , the maximum gets shifted to higher t_1 and t_2 values. However, with growing t_1 and t_2 the relative noise contamination within an exponential decay signal rises and hence with growing order n and k the noise contribution will more and more dominate the numerical integration. Due to that a rather high approximation point seems to be favorable.

On the other hand, the 2D Laplace image of the time domain signal has a pole structure which gets approximated by a 2D rational polynomial. Clearly one wants to minimize the distance between the approximation point and the biggest pole in the Laplace image in order to achieve a good approximation. This actually counteracts the statement from above because it requires a small approximation point. For those reasons it was aimed to find a compromise and defined the approximation points for T_2 -like dimensions as the inverse point in time when the signal had half of its initial amplitude [15] and for T_1 -like dimensions as the inverse point in time when the signal had its zero crossing.

As a side note one must add that Chisholm approximations with an increasing order will become more unstable when noise is present in the signal. With an increasing approximation order higher c_{nk} are required. However, like explained above, for an increasing power series order noise contributes more and more to the integral in Eq. 3.9 and hence decreases the accuracy of the approximation.

Coming back to the example of Fig. 3.3 A), one can note that the Chisholm approximation method is able to detect all three relaxation compartments correctly and also gives the correct values for the amplitudes with an acceptable precision. However, there are two small artifacts localized at exchange sites which are false positive. In contrast to that the

Tikhonov regularization method is not able to separate the three compartments but one must say that this method was not developed to calculate 2D discrete relaxation maps. This was taken into account with the small TOL value which was chosen to optimize the smoothing parameter α .

Another interesting point is the processing time of both algorithms and the computational needs. The main task during an inversion with the Chisholm approximation method is to calculate the power series coefficients in Eq. 3.7. In case of a $\langle 2/3 \rangle$ approximation this must be done for 14 coefficients [17]. So the computational load is mainly composed of the calculation of the integration kernel in Eq. 3.9 and especially of the subsequent 2D integration. To speed this up one could think about possible parallelization strategies on a workstation or outsource the integration on a FPGA. The calculation of the Chisholm coefficients out of the power series coefficients is done by solving a system of linear equations which is computationally negligible with respect to the integration. With an increasing number of relaxation compartments the required approximation order also increases and hence the computational load gets heavier. But still, this is very memory efficient since only the integration kernel must get stored. This integration kernel has got a size which is equal to the length of the direct and indirect dimensions, denoted with s_1 and s_2 respectively here. So in case of the results in Fig. 3.3 A) its basic size was 1024×1024 which increased by a factor of five for each dimension due to the spline interpolation. In contrast to that the Tikhonov regularization method needs to store the kernel matrix K , Eq. 3.15, which can become very large and is not only a function of s_1 and s_2 but also of the size of the requested inversion result itself, denoted with f_1 and f_2 here. In general the kernel matrix size is then given by $s_1 s_2 \times f_1 f_2$ which gives a kernel matrix size of 1048576×1024 for the example discussed above [60]. Though there are singular value decomposition (SVD) procedures [11] available to truncate this kernel size, they were not implemented in order to maintain the pure resolution properties of the Tikhonov regularization method. However, those SVD truncation techniques would considerably speed up the inversion process. For that reason the Tikhonov regularization could definitely get implemented in a faster manner and hence the processing times given in the previous section represent only the results of the current implementation neglecting the SVD speed up capabilities. Finally one must note that the computational load of the Tikhonov regularization method is independent of the number of relaxation compartments which is in contrast to the Chisholm approximation method.

In Fig. 3.3 B) a more general comparison between both methods is given for the simulated relaxation map from Tab. 3.1. It is interesting to see that the χ^2 distance of the Tikhonov regularization method shows nearly no noise dependency whereas the accuracy of the Chisholm approximation method increases with increasing SNR. For a SNR of around 50 - this lies well in the range of typical 2D NMR relaxation experiments (see e.g. [64, 65]) - the mean Chisholm approximation error is smaller than the mean Tikhonov regularization error. And in contrast to the constant χ^2 behavior of the Tikhonov regularization method the

Chisholm approximation χ^2 distance converges to 0 for large SNR as one would expect. The Chisholm approximation has got a large mean error and standard deviation for low SNR. This is attributed to the noise contribution when calculating the power series coefficients c_{nk} . The behavior of the Tikhonov regularization method can be explained by two points. Firstly, this is the introduction of the smoothing parameter α which aims to make the ill-posed problem of an inverse Laplace transform immune to different noise realizations and hence explains partly the SNR independence. Secondly, with a 32×32 matrix a rather coarse grid size was employed. Certainly the χ^2 distance of the Tikhonov regularization method can get decreased by a finer grid resolution in the region of interest but this could probably also introduce a stronger noise dependency, especially for small SNRs.

Further interesting features of the algorithm emerge in the second simulation where the T_1 - T_2 time domain signal with an underlying relaxation map containing three symmetric Gaussian distributions with moderate widths were investigated, Tab. 3.2. Although the basic implementation of the algorithm is designed for a 2D exponential decay like it occurs in a T_2 - T_2 experiment one can also analyze T_1 - T_2 data by correcting the indirect dimension in the Laplace domain. In addition it is very interesting to note that with this algorithm it was possible to calculate the relaxation map given in the third row of Tab. 3.3. Since the algorithm was designed for delta-like distributions the width of the Gaussian peaks is not accessible by the Chisholm approximation analysis. However, the relaxation rates coincide with the simulated position of the peaks and resulting residues correlate well with the area under every peak. Finally one can see with the $\langle 3/4 \rangle$ approximation how negative relaxation rates emerge, when the Chisholm approximation order exceeds the number of relaxation compartments in the relaxation map while the previously detected compartments remained. This last feature is of great interest when comparing the Chisholm approximation method with a 2D multi-exponential least square fit. With a least square fit it is necessary to know the number of relaxation compartments which are present in the sample, i.e. the number of all r_{ij} in Eq. 3.1. In contrast to that for the Chisholm approximation method this knowledge is not mandatory. Here, one can apply the incrementation scheme described in the previous section and exemplified with the results of the T_1 - T_2 simulation in Tab. 3.3

Additionally one must say that the employed width σ of the Gaussians is very small with respect to the relaxation rates. For that reason it would be interesting to investigate broader relaxation distributions in a future work. For Gaussians, i.e. symmetric relaxation distributions, it should be possible to determine the peak position and the area of the peak with the Chisholm approximation method as long as the SNR is high enough for the required approximation order. But still, the actual peak width is not accessible. In contrast to that it should be hardly possible to determine relaxation compartments of strongly asymmetric distributions like they can be found for example in [42].

When analyzing the experimental data, Tab. 3.5, one can see that the relaxation rates calculated for the samples I-V to III-V are in very good agreement with the 1D calibration

data from Tab. 3.4. Furthermore the results of I-V and II-V contain nearly no relaxation amplitudes on off-diagonal positions, as one would expect. However, for sample III-V the off-diagonal contribution gets stronger nevertheless the detection of relaxation rates is still accurate. The Tikhonov regularization method is also reliable for the I-V and II-V samples. For the sample III-V in 7 of 10 datasets it is not possible to separate the two compartments which illustrates the resolution limit. Potentially one could increase this by using a better resolved kernel but this would make the algorithm even more memory expensive. Another approach would be to further zoom into the region of interest in the relaxation map. This would increase the resolution but not affect the memory requirements. The resolution limits found in this work agree well with the literature. For example in the supplementary information of [64] for a SNR of 1000 two compartments with an amplitude ratio of 1 : 1 were not resolvable with the Tikhonov regularization method when their relaxation rates had a ratio of 1.5.

Again visible in Fig. 3.5 for the inversion outcome of sample III-V are exchange artifacts. To counteract those false peaks a more accurate calculation of the power series coefficients c_{nk} is necessary, this was already explained above. Another approach, which is not applicable to this example, would be to decrease the number of pole line crossings illustrated in Fig. 3.1 B). So far off-diagonal Chisholm approximations with an order $\langle N - 1/N \rangle$ were investigated where both variables in the numerator and both variables in the denominator had an equal maximum power, i.e. $N - 1$ and N respectively. This makes N^2 pole line crossings where the residues must get evaluated and possible artifacts can occur. For a suitable relaxation map one could also investigate more general Chisholm approximations where both variables in the numerator and in the denominator have an unequal maximum power [66] and hence reduce the number of pole line crossings in the Laplace image of the time domain signal.

4 Multi-Channel NMR System Development

In this chapter the development of a novel multi-channel NMR (mNMR) system for low-field applications will be presented. The design principles, the system validation and the results of T_2 binding experiments measured with the mNMR system were published in [67]. The T_2 binding experiments presented therein were performed at the *MGH Center for Systems Biology* (Boston, USA) and are the result of a collaboration with that institute.

At the beginning of the chapter the design principles will be presented along with the experimental methods to validate the system. Accordingly the electrical characterization of the device is presented and finally the validation of the system based on NMR experiments is presented. The chapter finishes with a detailed discussion where the mNMR setup gets analyzed and compared to existing platforms.

4.1 Methods - System Development

4.1.1 System Overview

Exemplified for a 3-channel system, Fig. 4.1 A) gives the basic design concepts of the mNMR system. Several points should be emphasized through this figure. First, the system is separated into three main sections, i.e. a digital processing part, an analog amplification part and the NMR probes. Second, the system is based on a software defined radio (SDR) approach, i.e. all signal processing tasks besides amplification are implemented digitally. And third, a time-interleaving procedure was chosen, i.e. through time multiplexing only a single-channel (SC) amplifier is used for the multi-channel (MC) system.

The targeted applications, Fig. 4.1 B), of the mNMR system are the determination of the longitudinal and transversal relaxation times T_1 and T_2 as well as NMR spectroscopy (NMRS) investigations.

Two different permanent magnets were used. On the one hand, the *PM1055-050N* magnet manufactured by *Metrolab* (Geneva, Switzerland). It has a mean field strength of 0.49 T which corresponds to a ^1H Larmor frequency of 21.040 MHz. Its footprint is 0.5 dm^2 and it weighs 1.25 kg. This magnet was solely employed for relaxation experiments. On the other hand, the *M2* from *Aspect Imaging* (Shoham, Israel) which got only used for NMRS investigations of ^{13}C , ^{19}F and ^1H . The magnet's mean field strength is 1.05 T which corresponds to Larmor frequencies of 11.261 MHz, 42.135 MHz and 44.790 MHz for ^{13}C , ^{19}F and ^1H respectively. The *M2* is actually part of a preclinical small animal MRI system and is therefore heavier and

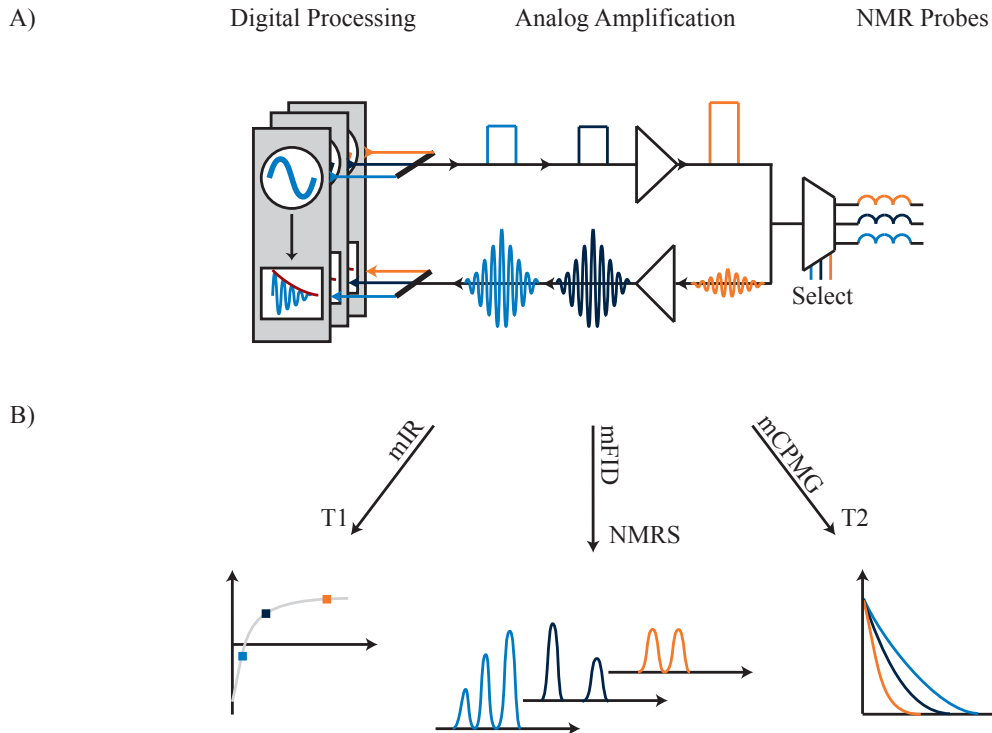


Figure 4.1: A) Design principles of the mNMR system. B) Targeted applications for the system.

larger. Its footprint is 48 dm^2 and it weighs 1000 kg. For simplicity in the following sections the magnets will be just termed the 0.5 T and the 1 T magnet respectively.

All design files like schematics, source codes and CAD models of the mNMR system are attached to this work on a DVD. An overview of this can be found in the appendix 6.2.

4.1.2 Digital Processing Unit

Mostly all digital signal processing tasks were implemented with the hardware description language *VHDL* on a *Xilinx Virtex 6* (San José, USA) FPGA in conjunction with a *ML605* board. As a design environment the *Xilinx ISE Design Suite 13.4* was chosen. A depiction of the digital design principles is given in Fig. 4.2 A).

The FPGA design approach is partly based on the results from [68]. There the development of Micro-Processor (μC) programmed in *C* with its Ethernet interface to *MATLAB* (Natick, USA) started. Furthermore, the utilization of FPGA internal memory blocks (BRAM), the fast Fourier transform (FFT) and the interfaces to control external hardware (not shown here) were tested. Finally, in [68] a first single channel NMR processing kernel got developed like it is shown in Fig. 4.2 B) in detail.

With respect to signal processing tasks this kernel is the core of the setup. Through its direct digital synthesis (DDS) the carrier frequency for the resonant NMR excitation

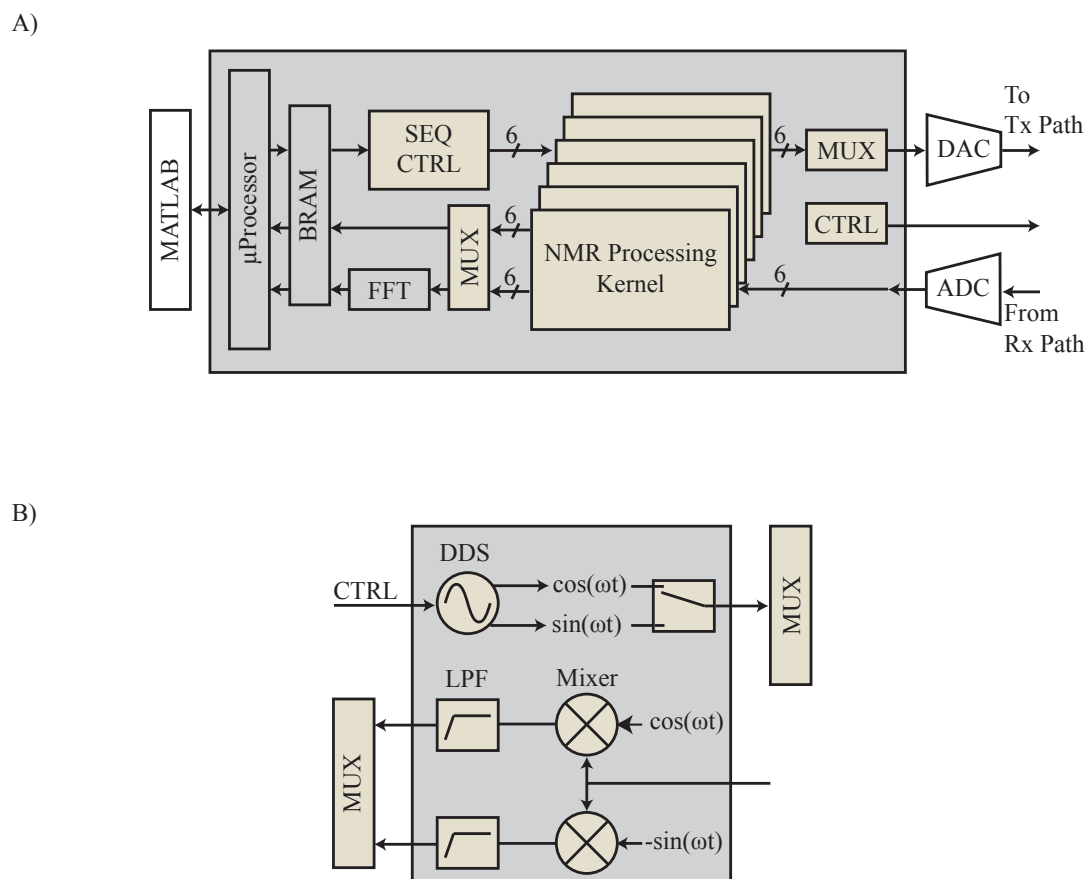


Figure 4.2: Schematic of the digital processing unit. A) Overview with peripherals. B) Close-up of the NMR processing kernel.

gets generated and switched to the output. The same carrier frequency is channel-wise also employed for complex down-modulating (IQ-demodulation) the NMR receive signals. For that reason the adjustment of the DDS frequency defines the investigated nuclei or accordingly the field strength of the system. In contrast to [68] the kernel got significantly improved and refurbished in this work. Now it can handle complex outputs, i.e. the in-phase and quadrature components of the receive signal get stored separately. Furthermore, the sampling frequency of the output gets strongly low-pass filtered and down-sampled. This is done by a chain of FIR filters after the mixers. For simplicity in Fig. 4.2 only a single filter is depicted. All filter coefficients were calculated with *MATLAB*. To implement the DDS, the μC , the FIRs, the mixer and the FFT, the *Xilinx Core Generator* was employed.

Based on this, the digital MC capabilities were implemented through parallelizing this processing kernel in the FPGA along with the required multiplexers (MUX). These multiplexers split up the time-interleaved NMR receive signals to the corresponding kernel and, vice versa, serialize the excitation signals from the kernel. All MUXs as well as the DDS frequencies are controlled by the sequence controller (SEQ CTRL) which got also developed in this work.

This component is the host of all NMR experiments. A NMR experiment is a sequence of succeeding events, most importantly those are the adjustment of the DDS frequency, the coil selection, the pulse excitation and the signal acquisition. Now the μC puts a sequence of commands into a defined BRAM section. A command consists of an identifier for the task which need to be done, a time stamp defining when it needs to get done and an optional parameter like e.g. the pulse length. From that it follows that the mNMR system can be easily programmed with different sequences. The sequence must only be programmed with *C* into the μC .

The digital-to-analog (DA) and analog-to-digital (AD) signal conversion was performed with the mezzanine card *FMC150* from *4DSP* (Austin, USA). On that card two DA and two AD channels are available. The AD converter (ADC) has got a 14-bit resolution, its maximum input amplitude is 1 V. The DA converter (DC) has got a 16-bit resolution and can drive signals with a maximum amplitude of 400 mV at the frequencies of interest. Internally a scaling component was implemented in the FPGA to allow a variable DAC output. With this the maximum Tx voltage can be multiplied by a rational number a/b . Both, the multiplicand and the denominator possess an 8-bit resolution and must obey to $a \leq b$.

4.1.3 Analog Amplification Unit

The requirements on the analog amplification unit of NMR signals are manifold. There is the low noise amplification of the NMR receive signal (Rx) as well as the high power amplification of the NMR excitation signal (Tx). Furthermore, there is the duplexer which must be able to separate the Tx and Rx paths respectively and connect them to the NMR probes. Additional drivers are requested to control the behavior of the PIN diodes located in the design and finally a supply unit is needed which must provide stable current and voltage levels.

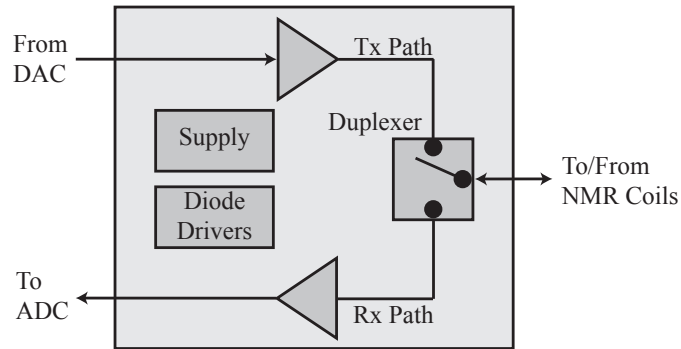


Figure 4.3: Schematic Overview of the analog processing unit.

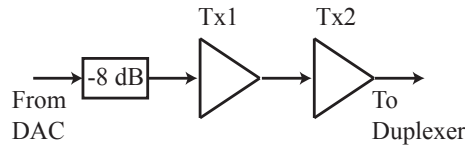


Figure 4.4: Schematic implementation of the analog Tx path.

To cope with those requirements an analog processing unit - schematically depicted in Fig. 4.3 - was developed and realized on a printed circuit board (PCB). The board was designed with *Altium* (Sydney, Australia) and manufactured by *PCB-Pool* (Aarbergen, Germany). All parts were soldered by hand to the board.

In the following paragraphs a more profound explanation of all components and their realization will be given. The detailed setup of the board is given in the attachment 6.2 where the schematic drawing and the layout plan can be found. Furthermore, the attachment 6.3 also contains a list of all mayor instruments which were used to characterize the analog amplification unit.

Tx Amplifier chain The Tx path, Fig. 4.4, consists of two amplifiers connected in series. This is the *ADL5536* (Tx1) from *Analog Devices* (Norwood, USA) and the *OPA2674* (Tx2) from *Texas Instruments* (Dallas, USA). To prevent a signal overload for the maximum possible DAC output signal the Tx chain has got a -8 dB attenuator connected right before Tx1.

Rx Amplifier chain The Rx path, Fig. 4.5, consists of four RF amplifiers from *Analog Devices* connected in series. As a low noise amplifier (LNA) the *ADL5536* was chosen followed by a variable gain amplifier *AD8331* (Rx2) and a *AD8350* (Rx3). To drive the ADC input, again a *ADL5536* was employed. The gain of Rx2 and hence the full Rx path gain is scalable by a voltage V_{Gain} which is in turn adjustable by an on-board potentiometer. Additionally there is also an option implemented to control the gain through an external voltage. The bandpass filters (BP1-3) and the high-pass filter (HP1) ensure the stability of the amplifier

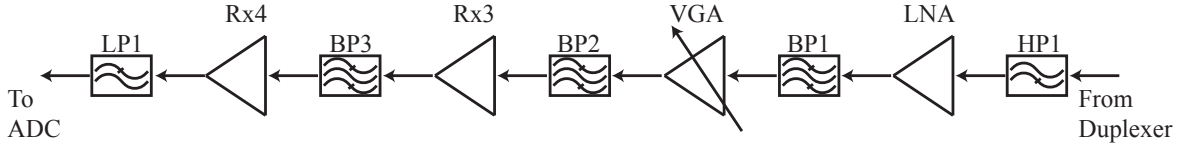


Figure 4.5: Schematic implementation of the analog Rx path.

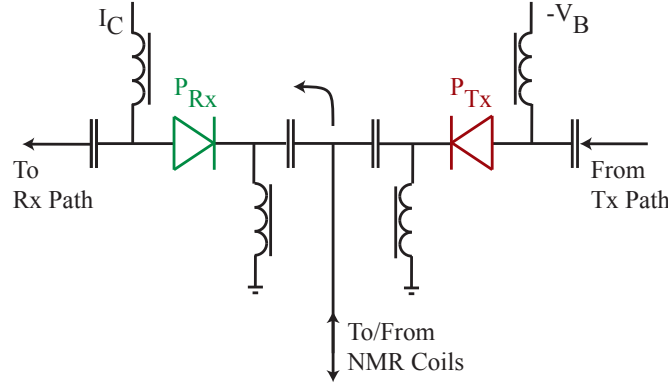


Figure 4.6: Schematic implementation of the broadband duplexer illustrated for the receive case here. The Rx PIN diode P_{Rx} is in a conduction state whereas the Tx PIN diode P_{Tx} is in a blocking state.

chain by band-limiting the Rx path in a range between 10 MHz to 50 MHz. Besides that they are not intended to fulfill signal processing tasks. The low-pass filter (LP1) at the output guarantees the compliance to the Nyquist sampling theorem. All filters were realized with lumped element LC circuits. The respective inductances and capacitances were calculated according to a Chebyshev design like described in [49].

Additionally, to prevent excessive receiver saturation during the NMR excitation pulses all amplifier inputs are protected with crossed Schottky diodes. Also for protection reasons, the Rx path output and hence the ADC input is limited by a pair of crossed Schottky diodes in series to a pair of crossed silicon diodes.

Duplexer To switch the NMR coils between the Rx and Tx amplifier chain a duplexer based on PIN diodes was employed, similar to the circuit described in [69]. However, in contrast to [69] a broadband design, Fig. 4.6, was implemented. The duplexer is based on two PIN diodes, P_{Tx} and P_{Rx} , located on the Tx path output and Rx path input respectively. The schematic setup is depicted in Fig. 4.6 with the duplexer in the Rx mode, i.e. a control current I_C is fed through P_{Rx} to ensure a low impedance state of the diode and simultaneously a negative blocking voltage $-V_B$ is applied at P_{Tx} to guarantee the high impedance state of this diode. The inductors in Fig. 4.6 serve as RF chokes, the capacitances as DC blocks.

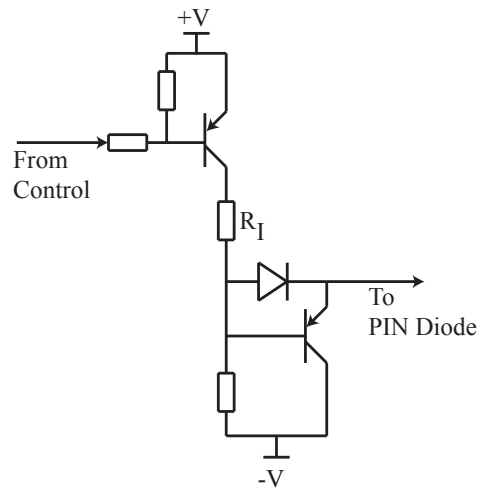


Figure 4.7: Basic building block of the PIN diode driver [70].

Diode Drivers The basic building block of the PIN Diode Driver is based on [70] and shown in Fig. 4.7. As function of the voltage input the circuit switches either a positive (+V) or negative (-V) voltage to the PIN diode. The positive voltage is supposed to drive a current through the PIN diode whereas the negative voltage merely serves for blocking purposes, i.e. no current is supposed to flow here. The resistor R_I is of primary interest because it adjusts the DC current level which gets fed to the PIN diode. The transistor Q1 serves as a switch for the positive supply voltage, the transistor Q2 aims to speed up the carrier removal from the PIN diode when the negative blocking voltage gets applied. In addition to the schematic in Fig. 4.7 each PIN driver is accompanied by another bipolar transistor (not shown here) in a grounded emitter configuration at its control input. This allows a switching of the driver with voltage levels shortly above 0.7 V, i.e. the Si forward bias.

The duplexer contains two PIN diodes which must get controlled complementary, i.e. one diode is in an isolation state whereas the other diode is in a feed-through state. To achieve this with a single control signal a complementary driver was employed (not shown here) [70]. Basically, there the voltage level above the resistor R_I serves as a input to another PIN driver which gives a complementary output. In this configuration the first driver was used to control the Tx side P_{Tx} of the duplexer whereas the complementary driver served to control Rx side with the diode P_{Rx} .

Supply To supply the amplifiers and the PIN diode drivers a switched-mode power supply is employed. In general such a supply module outputs a DC voltage which is superimposed by a weak supply ripple caused by the switching frequency. To suppress the distortion of amplifier outputs through this ripple, decoupling capacitors and ferrite beads got connected to all amplifier supply inputs. Furthermore, for generating the negative blocking voltages,

requested by the PIN diodes, a voltage inverter is used. Finally, to prevent damages through misconnecting the power supply a positive temperature coefficient resistor and a varistor protect the PCB input.

4.1.4 NMR Coils

Within this project three different types of multi-channel coil configurations were built, namely a quattro-coil setup (qCoil), a hexa-coil setup (hCoil) and a dual-coil setup (bCoil). For those, two different types of solenoids were employed, i.e. a micro-coil with a length of 4 mm and a diameter of 2.4 mm as well as a body coil with a length of 17 mm and a diameter of 12 mm.

qCoil: 4-Channel Array The qCoil setup consists of four micro solenoids targeted to be used at 0.5 T. All four coils were tuned to the ^1H Larmor frequency at 21.040 MHz. The four coils were mounted on a PCB with a pair of coils on the top and a pair on the bottom side. Both coils within a couple were aligned in a right angle with respect to each other. Their center-to-center distance was 7.5 mm. The corresponding decoupling coils had a diameter of 3.5 mm and a maximal possible length of 22 mm. They were made of a 0.56 mm diameter enameled copper wire.

hCoil: 6-Channel Array The hCoil setup consists of six micro solenoids targeted to be used at 1 T. Two coils were tuned to the ^{19}F resonance at 42.135 MHz the remaining four coils were tuned to the ^1H Larmor frequency at 44.790 MHz. This time all coils were mounted on the top side of a PCB with a right angle alignment between neighboring coils. The direct center-to-center distance was 8 mm. Slightly bigger than before, because here the coils also had a small vertical offset of 2 mm with respect to each other. The decoupling coils had a diameter of 5 mm and a maximum length of 22 mm. They were made again with 0.56 mm diameter enameled copper wire.

bCoil: Body-Coil Array The bCoil setup consists of a micro solenoid for ^{13}C which is enclosed in a ^1H body coil. The setup is targeted to be used at 1 T. For the bCoil setup a decoupling circuit was omitted.

All micro-coils had 8 windings of an enameled copper wire with a diameter of 0.4 mm. The coils were built around hollow cylinders with an outer diameter of 2.2 mm and a wall thickness of 0.4 mm. The DC magnetic field of this coil type was also simulated with *COMSOL* (Stockholm, Sweden). The body coil from the bCoil setup had a casing with an inner diameter of 10 mm. It had eight windings made with a 0.80 mm diameter enameled copper wire.

The required casings for the NMR and decoupling coils as well as the coil board sockets were manufactured with a 3D printer *Stratasys Objet Eden 260V* (Rheinmuenster, Germany). The drawings were made with *SolidWorks* (Waltham, USA). The required PCBs had a grounded copper layer between their top and bottom side. They were designed with *Altium* and manufactured by *PCB-Pool*.

In order to tune and match the coils a differential scheme, Fig. 2.6, was realized. All employed fixed capacitances were NP0/C0G ceramic capacitors. The trimming capacitances were chosen from the *Voltronics* (Cazenovia, USA) JZ series. Furthermore, the decoupling circuits of the qCoil and hCoil setup had configurations built with 6.8 μH RF chokes and 100 nF DC blocks. The employed PIN diodes were the *MA4P1250NM-1072T* manufactured by *M/A-Com* (Lowell, USA).

To adjust all capacitances C_M , C_T and C_S and to compare the single-channel and multi-channel configuration several steps were performed sequentially. At the beginning every coil on its own - the other coils got electrically disconnected - was tuned and matched to the desired resonance frequency in a single ended configuration, Fig. 2.6 A). After that the adjusted value for C_M was measured. In a second step the determined C_M got doubled and every coil - again on its own - got tuned and matched in a differential scheme, Fig. 2.6 B). Then a decoupling coil with a PIN diode was switched into the resonance circuit, Fig. 2.6 C) and D). While feeding 50 mA to the PIN diode, the number of decoupling coil turns and their mutual distance got optimized until a minimum of the s_{11} parameter occurred. This procedure was again repeated for all coils individually (SC). Finally, all coils in the differential matching scheme with optimized decoupling circuits got connected to the board (MC). Then the trimmer capacitors got adjusted once more with only a single coil in resonance. Again each non-resonant coil got decoupled with a 50 mA DC current.

To investigate the behavior of the coils with respect to the decoupling current, SC coils were built and matched to 21.040 MHz, 42.135 MHz and 44.790 MHz. Then the s_{11} parameter was investigated as a function of the decoupling current.

To analyze the switching behavior of the qCoil and the hCoil board, the setup depicted in Fig. 4.8 was employed. A signal generator - set to either 21.040 MHz, 42.135 MHz or 44.790 MHz - with a $50\ \Omega$ source impedance was connected to a scope with a $50\ \Omega$ load. In parallel to that a single channel NMR coil tuned and matched to either 21.040 MHz, 42.135 MHz or 44.790 MHz, depending on the generator output, was placed. The coil's decoupling circuit was connected to the output of a PIN Driver as shown in Fig. 4.7. The PIN driver in turn was controlled by a square wave generator.

4.1.5 Pulse Sequences

As shown in Fig. 4.1 the mNMR system was developed for T_1 , T_2 and NMRS experiments. For that reason the pulse programmer contains single channel IR and CPMG sequences and

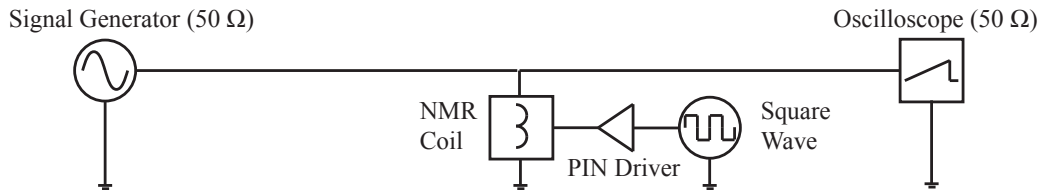


Figure 4.8: Setup to investigate the coil switching behavior.

also FID recording capabilities. In addition to that multi-channel time interleaved sequences for spectroscopy (mFID), T_1 (mIR) and T_2 (mCPMG) measurements were developed.

mFID The mFID sequence, illustrated for six coils in Fig. 4.9 A), is the sequential excitation and recording of NMR FID signals for an arbitrary number of coils between 2 to 6. The CHANNEL parameter (CH) defines how long a single coil is in resonance and sets the general timing of the sequence. In addition to that the pulse length parameter (α_i) and the length of the acquisition window (ACQ) define the behavior of each single coil.

mIR The mIR sequence, Fig. 4.9 B), is the multi-channel counterpart of the single-channel IR sequence and is implemented for 4 coils only. Its purpose is to sample the T_1 buildup of a single sample which is loaded to all coils in a time interleaved manner. Its timing is again defined by the CH and ACQ parameter as well as the pulse length which are supposed to match the 90° and 180° flip angles. Furthermore, there are the inversion times TI_i for all coils which must be ordered in an increasing manner. To sample the T_1 buildup curve more densely this sequence gets repeated N times separated by an adequate relaxation delay. Finally this sequence requires an additional cycle with $TI_N \gg T_1$ for normalization purposes.

mCPMG The mCPMG sequence, illustrated for 4 coils in Fig. 4.9 C), is the time interleaved multi-channel counterpart of the single-channel CPMG sequence and is implemented for 2 to 4 coils. Here the purpose is to measure the T_2 decay curve of different samples loaded to the coils in a quasi-simultaneous manner. The sequence is again defined by the CH and ACQ parameters. Furthermore, there is the echo time TE and the number of echoes N which define the length of the echo trains.

4.1.6 Data Analysis

The final data fitting was performed in *MATLAB*. For sequences with comparatively long acquisition windows, i.e. FID-type and IR-type sequences, the final data analysis was done after Fourier transformation. In contrast to that for CPMG-type sequences, when the acquisition windows were comparatively short, the final data analysis was performed in the time domain. Since the recorded signals are complex, a phase correction was necessary. The

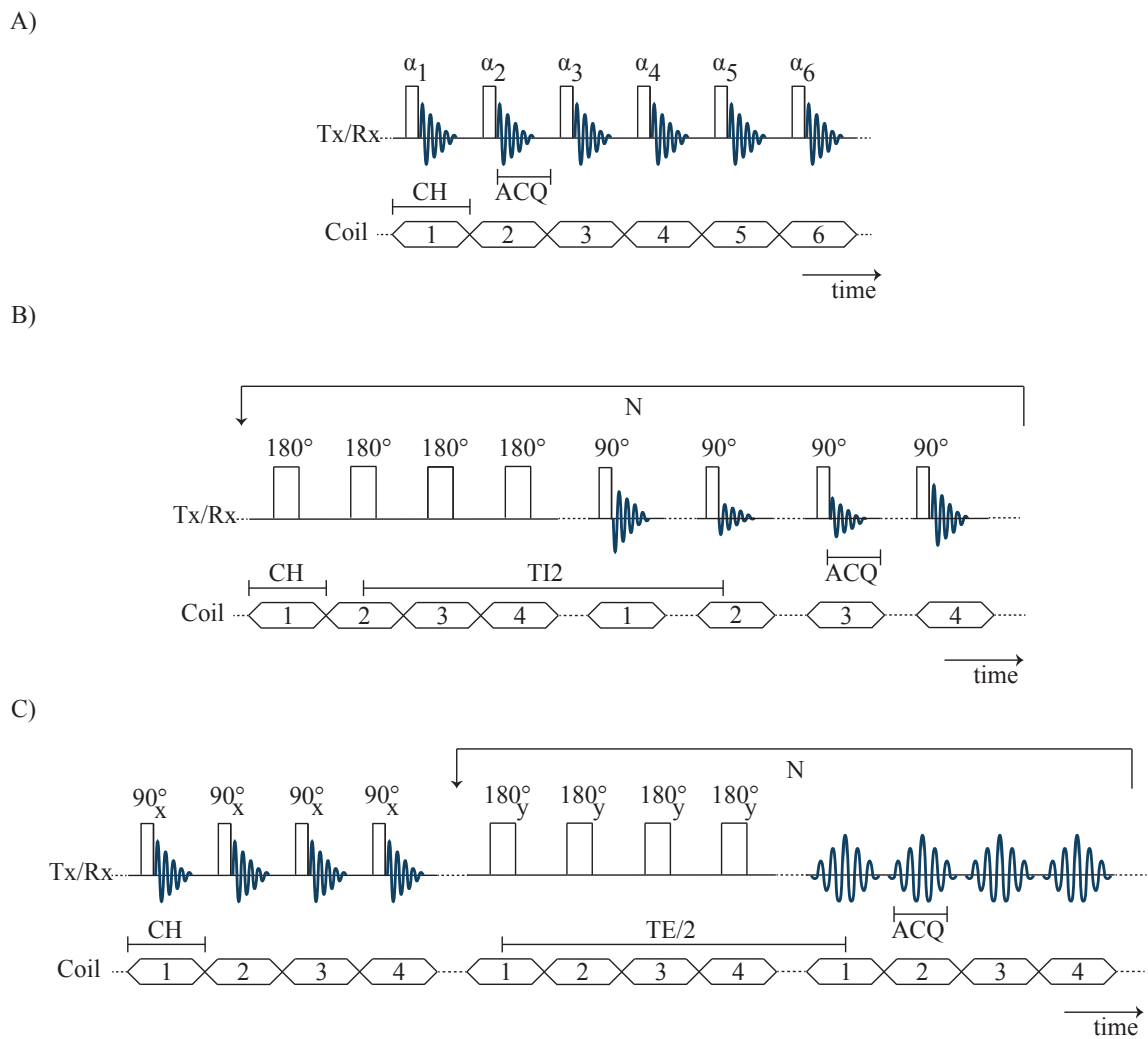


Figure 4.9: Schematic depiction of the multi-channel sequences developed for the mNMR system. A) mFID sequence for spectroscopy. B) mIR for T_1 experiments. C) mCPMG for T_2 experiments.

optimal phase was found by minimizing the difference between the data magnitude integral and the data real part integral as function of the phase. After phase correction only the real part was further analyzed.

To get the exponential build-up and decay curves for IR and CPMG-type sequences respectively the data of interest were integrated. To attenuate the influence of pulse imperfections in the IR build-up curves a three-parameter fit, Eq. 4.1a, was applied [71]. For the CPMG-like functions a simple exponential decay, Eq. 4.1b, was employed without offset.

$$a - b e^{-t/T_1} \quad (4.1a)$$

$$c e^{-t/T_2} \quad (4.1b)$$

4.2 Methods - NMR Application

4.2.1 General Settings

All NMR experiments presented in this work were performed with a 5 μl sample volume. The samples were confined in polyimide tubes with an inner diameter of 1.44 mm and a wall thickness of 0.03 mm. Furthermore, the DAC scaling was set to $\frac{1}{2}$. Since the mNMR system is based on analog 50 Ω interfaces this corresponds to a -4 dBm Tx path input power. In the analog Rx amplifier chain the VGA gain control voltage V_{Gain} was set to 0.525 V.

4.2.2 Quattro Channel - qCoil

For the 0.5 T experiments with the qCoil, the magnet casing was set to GND by connecting it with the coil. To evaluate the qCoil, the individual flip angles got calibrated, the coupling between the coils was studied and the relaxation measurement capabilities got validated.

For the flip angle calibration a single probe of the setup was loaded with H_2O and the NMR response after a single pulse excitation was recorded for an increasing pulse width [72]. This was done for all 4 coils available. To study the coupling between the coils again a single channel got loaded with H_2O . Subsequently with every probe a FID was recorded after a 90° pulse excitation. Then the sample was passed on the next channel and the procedure got repeated.

Finally the longitudinal and transversal relaxivities r_1 and r_2 of Cu^{2+} solutions got investigated with single-channel and with multi-channel sequences. For that reason $\text{CuSO}_4 \cdot 5 \text{H}_2\text{O}$ salt got dissolved in bidistilled water and a set of twelve solutions with logarithmically spaced concentrations between 0.01 g l^{-1} and 50 g l^{-1} got produced. Those solutions got loaded to all 4 coils. Then a single-channel IR sequence with coil 1 and a mIR sequence with all 4 coils got recorded. The T_1 build-up curve was sampled with 16 linearly spaced inversion times. In the multi-channel case 4 additional inversion times - long enough to ensure full signal relaxation - were added to allow the required signal normalization. For the lowest Cu^{2+} concentration

| Coil | Sample | |
|------|------------------------------|-----------------|
| 1 | 2,2,2-Trifluoroethanol (TFE) | $C_2H_3F_3O$ |
| 2 | Water | H_2O |
| 3 | N,N-Dimethylformamide | C_3H_7NO |
| 4 | Glycerol | $C_3H_8O_3$ |
| 5 | 1-Propanol | C_3H_8O |
| 6 | Perfluoro-1,8-Dichlorooctane | $C_8Cl_2F_{16}$ |

Table 4.1: Samples for spectroscopy experiments with the hCoil setup.

the mIR sequence parameters ACQ and CH were set to $1000\mu s$ and $2000\mu s$ respectively. With increasing concentration they got decreased stepwise towards an ACQ of $400\mu s$ and a CH of $450\mu s$ for the highest concentration.

The transversal relaxation of the same $CuSO_4$ solutions got also investigated in a single-channel and in a multi-channel manner. In contrast to the longitudinal study, here the single-channel measurement was done with every coil individually. The ACQ parameter was set to $100\mu s$ and CH was set to $300\mu s$. The employed echo time was 3 ms. For the lowest sample concentration 1600 echoes got recorded. This number decreased stepwise towards 25 for the highest concentration.

In both cases, i.e. for the r_1 and for the r_2 investigation, all measurements were done 10-fold at an ambient temperature of $22^\circ C$.

After about 100 reinsertions of the coil board holder into the 0.5 T magnet the edges of the holder deteriorated significantly due to ruptures. To ensure a tight placement of the coil board holder and hence a reproducible placement of the coils inside the magnet, the coil board holder got replaced by a new one after about 100 reinsertions.

4.2.3 Hexa Channel - hCoil

To analyze the hCoil setup at 1 T the flip angle of coil 2 was analyzed with H_2O . Afterwards spectroscopy experiments got performed with the samples given in Tab. 4.1. To attenuate sample flow out and evaporation one end of the polyimide tubes got sealed with wax.

In a first step only one coil at a time was loaded with its corresponding sample and a FID was acquired (SC). Afterwards all coils at a time got loaded and a mFID sequence (MC) was performed. In both cases ACQ was set to 125 ms. For the multi-channel experiment the CH parameter was set to 125.5 ms. To improve the B_0 field homogeneity the shimming unit of the MRI system was turned on. The shim parameter DC.x was set to 0.144, the parameters DC.y and DC.z were set to zero. Additionally, to assess the coil-to-coil B_0 homogeneity between the probes, all 4 1H coils got loaded with water and a FID was recorded.

Usually in NMRs the chemical shift is referenced to tetramethylsilane (TMS). To accomplish this with the MC measurement the H_2O peak of coil 2 was employed. Based on the resonant frequency of the water maximum the B_0 field was calculated taking the water chem-

cial shift of 4.7 ppm [21] into account. Through this calibration the ^1H spectra of coils 3, 4 and 5 could also get calibrated and hence are also referenced to TMS. For both ^{19}F spectra - i.e. coils 1 and 6 - the x-axis got calibrated through the frequency ratio 94.0940 %. This is the recommended ratio [73] and corresponds to a fluorine chemical shift referenced to CCl_3F .

Due to the field drift, a chemical shift referencing is not possible when investigating the SC dataset on its own. For that reason the SC data got not calibrated but only frequency shifted to achieve an overlap of the spectral maxima between the single-channel and multi-channel dataset for each coil.

4.2.4 Dual Channel - bCoil

With the bCoil a 8 M urea sample was investigated where ^{13}C was enriched to 99 %. The urea was dissolved in a 10 % D_2O and 89.85 % H_2O mixture with 0.15 % sodium azide (NaN_3) to prevent sample degradation. Furthermore, the ^1H and the ^{13}C spectra of urea were simulated with *ChemDraw* from *PerkinElmer* (Waltham, USA).

With the bCoil two experiments were performed, i.e. a pulse length calibration of the ^1H body coil and a ^{13}C spectroscopy experiment. Due to the expected weak signal an averaging procedure was applied with 5 measurements each separated by a 3 min waiting period. To allow a field drift correction the resonance frequency of the ^1H signal was employed, i.e. shortly before a ^{13}C measurement the ^1H Larmor frequency got determined. The maximum in the ^1H spectrum was used to determine the B_0 field strengths based on a proton H_2O chemical shift of 4.7 ppm. With a frequency ratio of 25.1450 % [73] the ^{13}C chemical shift was calibrated and corresponds to TMS.

4.3 Results - System Development

4.3.1 Digital Processing Unit

For the digital processing unit roughly 30 % of the available *Virtex 6* logic was used by the design environment. The ADC was clocked with a frequency of 245.76 MHz. This sampling frequency was decimated stepwise in the FIR chain to a final sampling frequency of 81.92 kHz after demodulation. The last FIR low-pass filter had a passband up to 5 kHz, the stopband began at 30 kHz. In conjunction to that, the filter delay was calibrated to be 75 μs . The sequence controller in the FPGA is clocked with 122.88 MHz. The resolution of command time stamps for the sequence controller was 1 μs . The resolution for the pulse length parameter is 0.1 μs , for the acquisition parameter the resolution is 1 μs . The digital duplexer control was leaded by 10 μs when going from the Tx to the Rx state and by 2 μs for the reverse transition. When switching coils the digital control signal was set 100 μs in advance.

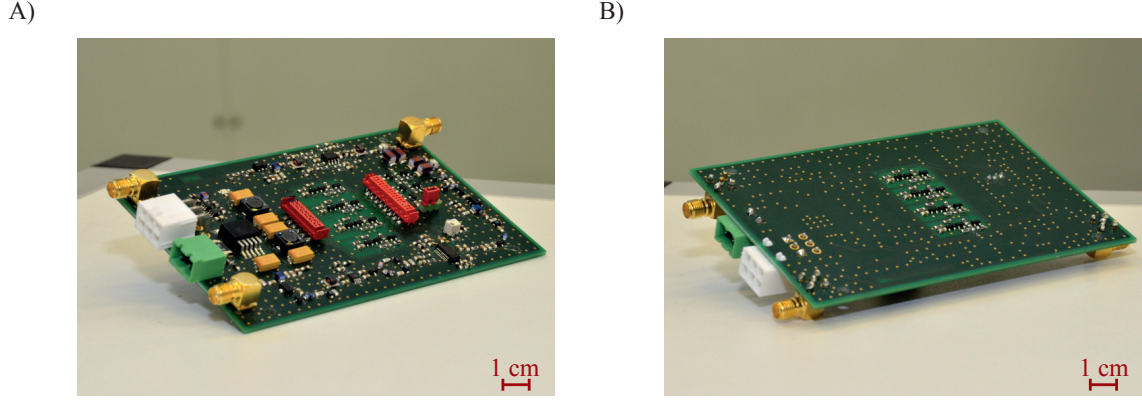


Figure 4.10: The mNMR amplification unit. A) Top side. B) Bottom side.

4.3.2 Analog Amplification Unit

In Fig. 4.10 the top and bottom side of the newly developed mNMR amplification unit is presented. The schematic is realized on a 2-Layer PCB with a size of 122.5×80.5 mm. Altogether the board contains 8 PIN diode drivers for coil decoupling purposes, 4 are on the top and 4 on the bottom side. All RF signal traces are routed on the top side with a grounded copper layer below and alongside the RF traces. The PCB requires a supply of 12 V with a current of 0.25 A. The board contains a second supply connector which allows a supply feed-through to the ML605 FPGA board. In this way only a single power source is necessary to operate the full mNMR system.

The PIN drivers, implemented with 100Ω resistors R_I , feed a current of 45 mA and supply a blocking voltage of -9.3 V. In the forward case the PIN driver for the duplexer also supplied a current of 45 mA through each of the two PIN diodes. In the isolation case it supplied a blocking voltage of -9.3 V and -7.0 V to the Rx and Tx PIN diode respectively.

In Fig. 4.11 the performance characteristics of the analog Tx and Rx amplifier chains are given. The Tx amplifier chain, Fig. 4.11 A), has got a gain of 26 dB for the 11.261 MHz and 21.040 MHz resonances and a gain of 24 dB for the 42.135 MHz and 44.790 MHz resonances. Furthermore, one can see the onset of the output power saturation with saturation values of 27 dBm for the two low-frequency curves and 26 dBm for the two high-frequency curves. In a 50Ω system this corresponds to an amplitude voltage of 7.1 V and 6.3 V respectively. With those saturation values and the gain from above one can estimate the 1-dB compression point P_{1dB} , i.e. the input power level where the output power deviates 1 dB from the linear behavior. For the low and for the high frequency couple P_{1dB} is at 1 dBm and at 2 dBm respectively.

In Fig. 4.11 B) the gain of the full Rx amplifier chain as a function of V_{Gain} , the variable gain amplifier (Rx2) control voltage, is given. The fitted slopes are 52 dB/V, 51 dB/V,

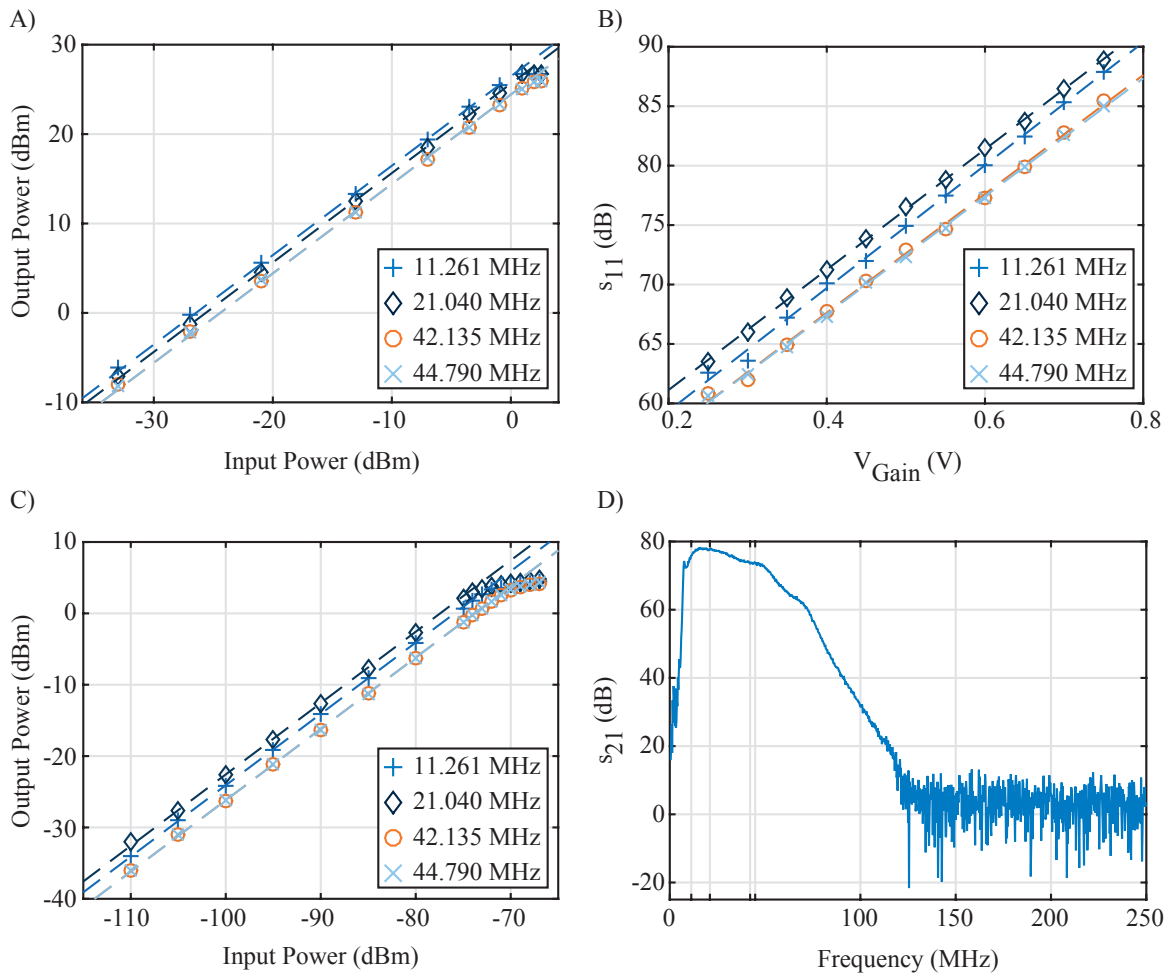


Figure 4.11: Characterisation of the Tx and Rx amplifier chains. A) Tx output power as a function of the input. B) Gain scalability of the Rx amplifier with V_{Gain} . C) Rx output power as a function of the input. D) s_{11} parameter as a function of frequency.

| Frequency (MHz) | Noise Figure (dB) | Gain (dB) |
|-----------------|-------------------|-----------|
| 11.261 | 6.0 | 19.6 |
| 21.040 | 3.7 | 20.1 |
| 42.135 | 4.2 | 19.8 |
| 44.790 | 4.3 | 19.7 |

Table 4.2: Noise figure and gain of the Rx input stage at the frequencies of interest.

50 dB/V and 50 dB/V, listed here for increasing Larmor frequencies. For all following results V_{Gain} was set to 0.525 V.

With this control voltage the linearity of the Rx amplifier chain was investigated, the results are given in Fig. 4.11 C). The linearized gains of the amplifier chain were 76 dB, 77 dB, 74 dB and 74 dB, again listed for increasing Larmor frequencies. Graphically one can read off the output power saturation value which is at 4 dBm and hence estimate the P_{1dB} value of the Rx chain. The results are -72 dBm, -73 dBm, -70 dBm and -70 dBm for an increasing frequency. The lowest input power investigated in Fig. 4.11 C) was -110 dBm. One can regard this - for the given input SNR - as the minimum detectable signal. In a $50\ \Omega$ system this corresponds to a voltage amplitude of $1\ \mu\text{V}$. With that minimum input power and the P_{1dB} points it is possible to estimate the dynamic range of the Rx chain, i.e. the ratio of the maximum input power to the minimum input power which corresponds to the difference since everything is given on logarithmic scales. Based on this the estimated dynamic ranges are 38 dB, 37 dB, 40 dB and 40 dB listed here for increasing frequencies. Associated to Rx characteristics of the Rx amplifier chain is the noise figure of the Rx input stage. This was measured, Tab. 4.2, for the duplexer accompanied with the first low pass filter LP1 and the LNA.

Finally, in Fig. 4.11 D) the s_{11} gain curve of the Rx chain as a function of frequency is shown. The four grid lines between 0 MHz and 100 MHz are located at the four resonance positions of interest.

In Fig. 4.12 the characteristics of the Rx duplexer side are presented. The attenuation for the feed-through and for the isolation state, Fig. 4.12 A), was measured on two different locations. First, at the output of the duplexer itself and second at the output of the subsequent low-pass filter LP1. In the first case the attenuation losses in the feed-through mode were -0.34 dB, -0.30 dB, -0.35 dB and -0.36 dB and in the second case they were -1.49 dB, -0.78 dB, -0.81 dB and -0.83 dB, given for increasing frequencies. In the blocking case all attenuation factors were well below -30 dB.

To evaluate the switching speed of the duplexer a 10 kHz rectangular wave was fed to the duplexer driver and simultaneously a continuous -2 dBm RF input signal was applied to the duplexer Rx side input. In Fig. 4.12 B) the output of the LP1 filter in conjunction with the rectangular control signal is shown. Here the RF input signal had a frequency of 21.040 MHz but for clarity only the envelope is presented. Clearly the Rx duplexer side is in the isolation

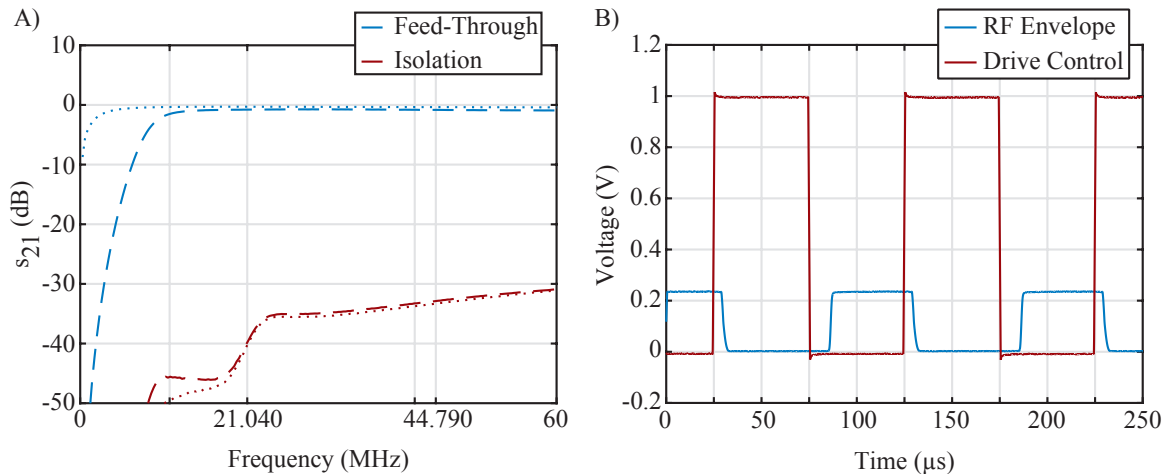


Figure 4.12: Duplexer characteristics A) The s_{21} parameter measured at the duplexer output (dotted line) and at the output of LP1 (dashed line). B) Switching behavior exemplified for a 21.040 MHz input signal

mode when a logic high is applied to the control input, a logic low switches the duplexer to the feed-through mode. The transition from the isolation to the feed-through mode was delayed by 10 μs , the actual transition lasts 2 μs . The reverse switching is delayed by 4 μs and the transition itself takes also 2 μs . For the other resonances and for the Tx diode (not shown here) the results were the same.

4.3.3 NMR Coils

In Fig. 4.13 the results of the magnetic field simulation for the micro coil are shown with a DC current of 1 A. The coil was placed in the center of a sphere filled with air. The coil's symmetry axis coincided with the x-axis. In Fig. 4.13 A) the B_1 -field in the xy-plane is given within a circle of radius 5 mm. The color scale represents the B_1 magnitude, the red arrows are logarithmically scaled and indicate the field lines. For illustrative purposes the same plot is repeated in Fig. 4.13 B) with the NMR micro coil hidden. Figure part C) shows the x-component of B_1 along the axial direction of the coil. The grid line located at 2.36 mT visualizes the theoretical outcome of Ampère's law. Finally, figure part D) also gives the x-component but in radial direction for several increasing distances from the coil axis center. The two grid lines at ± 0.72 mm indicate the borders of the employed sample tubes.

In Tab. 4.3 the complex impedances of both employed NMR coil types are shown. To connect the micro coil with the network analyzer a wire residual of 5 mm was left on each of the two coil pins. For the body coil the wire residual was 10 mm at each pin.

In order to tune and match those coils to 50Ω at the corresponding Larmor frequency and also in order to introduce a decoupling circuit the capacitances and decoupling coils described in the appendix 6.1 were employed.

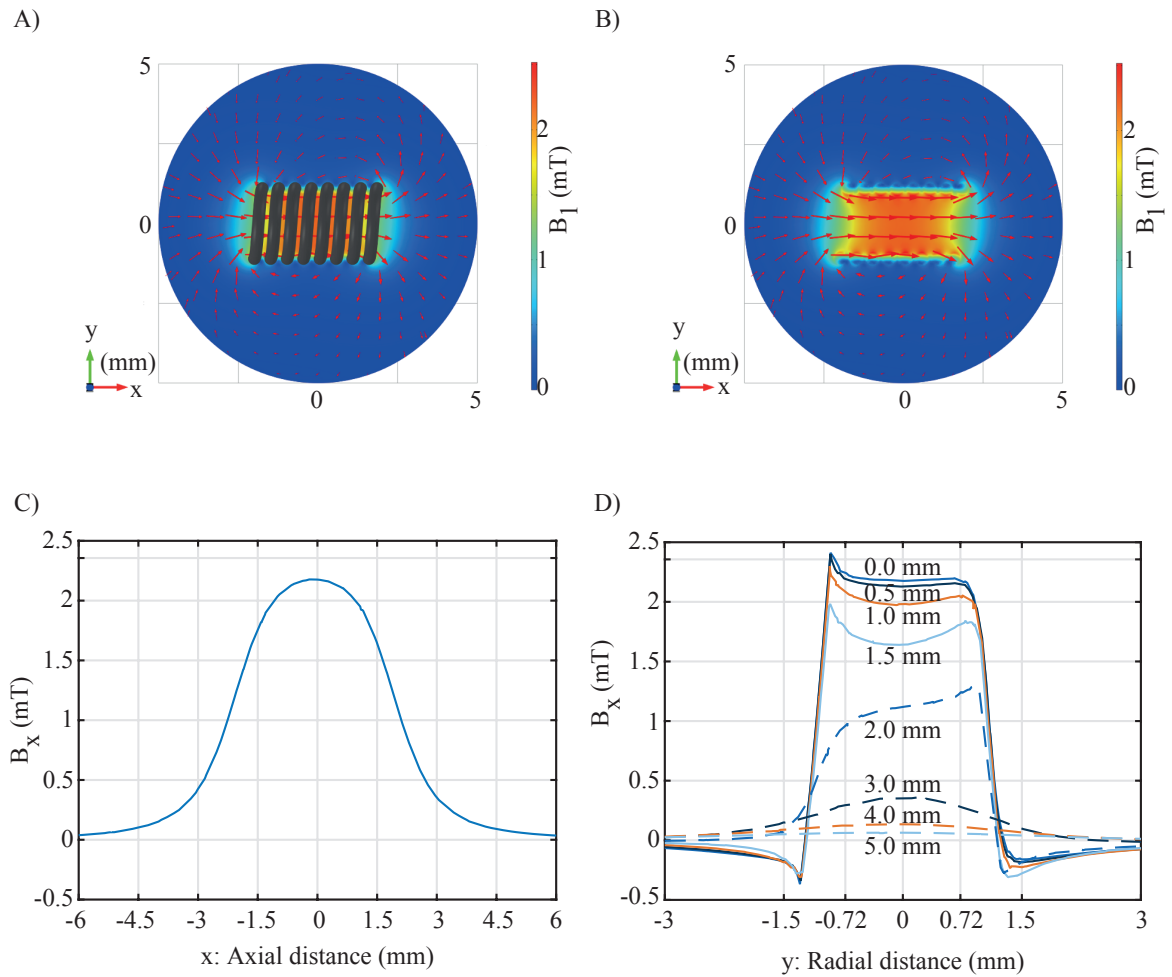


Figure 4.13: Results of the B_1 -field simulation with a current of 1 A. A) B_1 -field in the xy plane. Color scale gives the B_1 magnitude, arrows (logarithmically scaled) indicate the field lines. B) repetition of A) with the NMR coil hidden. C) x -component of the B_1 -field along the coil's symmetry axes. D) x -component of the B_1 -field along the y -direction - i.e. radially - given for the indicated distances from the coil center.

| Micro Coil | | | |
|-------------------|-------------------|-----------|-----|
| f (MHz) | R (m Ω) | L (nH) | Q |
| 11.261 | 137 | 82 | 42 |
| 21.040 | 239 | 81 | 45 |
| 42.135 | 420 | 80 | 50 |
| 44.790 | 435 | 80 | 52 |

| Body Coil | | | |
|------------------|-------------------|-----------|-----|
| f (MHz) | R (m Ω) | L (nH) | Q |
| 44.790 | 735 | 533 | 204 |

Table 4.3: Impedances and Q-factors for the employed NMR coils at the frequencies of interest.

To analyze the decoupling behavior as a function of the DC decoupling current single channel micro coils were tuned and matched to resonance frequencies of 21.040 MHz, 42.135 MHz and 44.790 MHz. In Fig. 4.14 A) the full s_{11} curves for different decoupling currents are illustrated for the 21.040 MHz case. The s_{11} parameter minimum was -47 dB when no current was fed to the decoupling circuit, the saturation value for a 100 mA decoupling current was -0.24 dB. In Fig. 4.14 B) only the s_{11} parameter at the three center frequencies are shown as a function of the decoupling current.

In Fig. 4.15 the qCoil is introduced, Fig. 4.15 A) and B) show the top and bottom side of the coil board respectively. The board has got dimensions of 80×30 mm. The top side contains two small NMR coils on the left followed by all four decoupling coils and the RF connector. The bottom side contains the remaining two NMR coils on the left along with the tuning and matching circuitry, the PIN diodes, the RF chokes and the PIN diode current connector on the right. The s_{11} parameters of the qCoil are presented in Fig. 4.15 C) where the SC and MC results are overlaid. In addition to that the decoupled s_{11} values of the single-channel case are given.

In Fig. 4.16 the hCoil is introduced, it has got a size of 80×52 mm. Figure part A) shows the top side of the board. The six small solenoids in front of the board are the NMR coils, the bigger solenoids behind them are the decoupling coils. At the rear end one can also see the single RF connector. Figure part B) shows the bottom side of the hCoil board. On the left hand side the NMR coils are soldered to the board followed by all tuning and matching capacitances, the PIN diodes and the RF chokes. The DC current to feed the PIN diode gets attached to the red connector on the right hand side. Figure part C) shows the s_{11} parameters, like above the single-channel and multi-channel measurement is presented

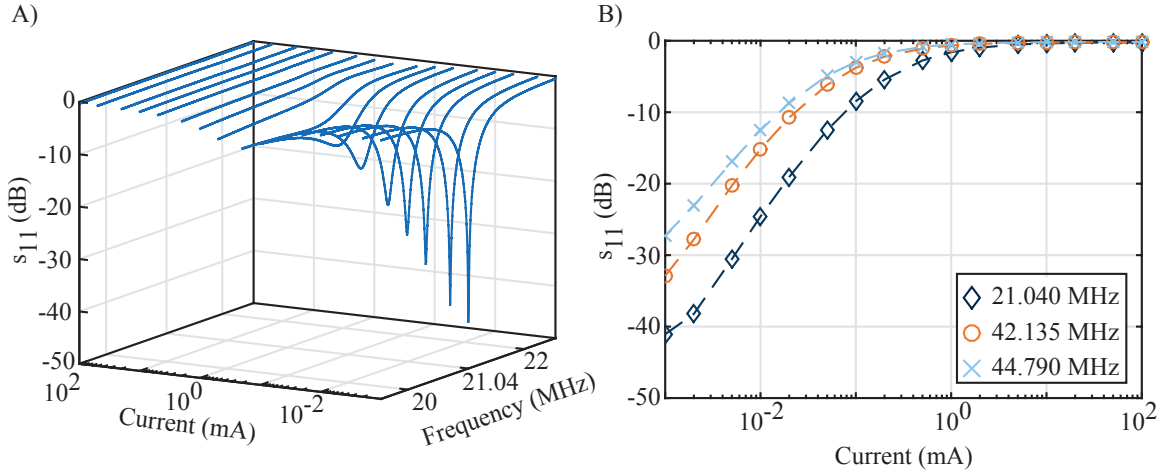


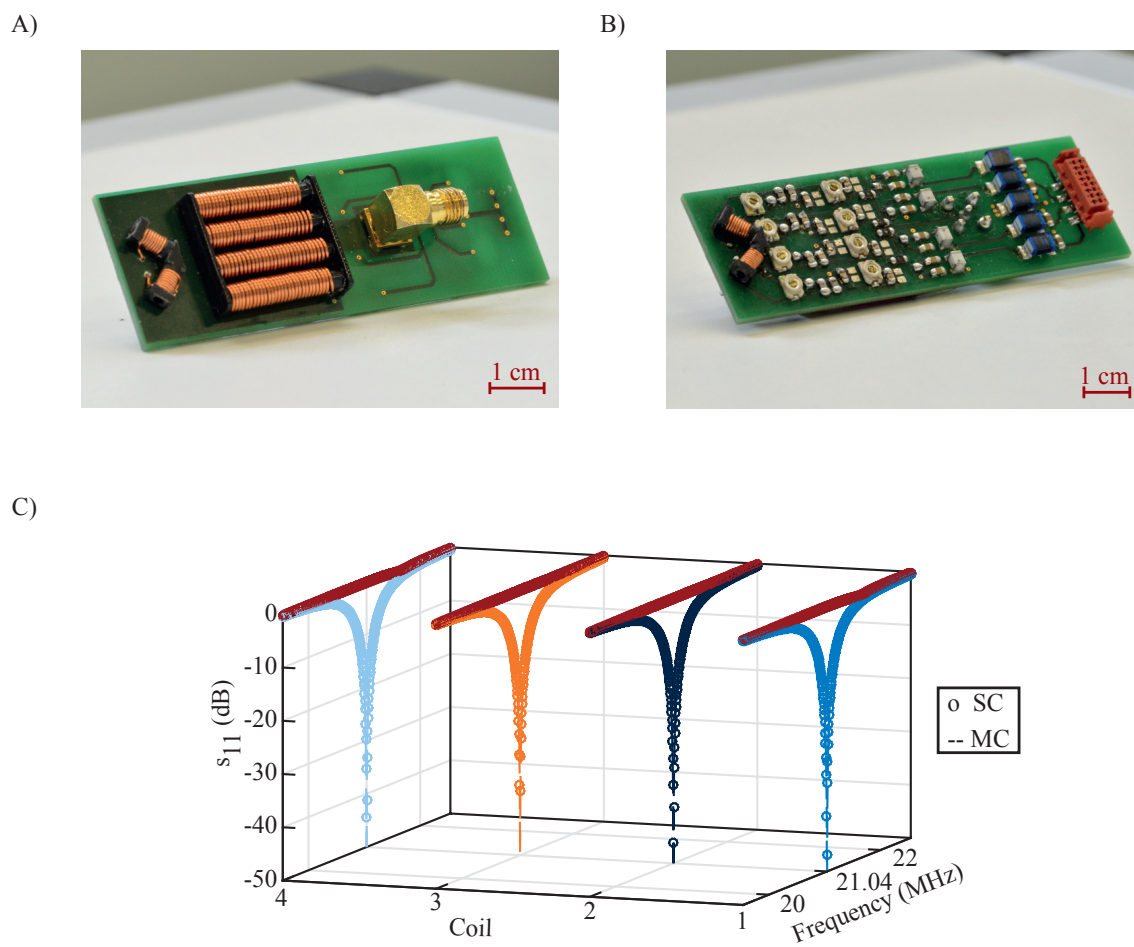
Figure 4.14: The s_{11} behavior as a function of the decoupling current for single-channel micro coils. A) Full s_{11} curves as a function of the decoupling current for a 21.040 MHz micro coil. B) s_{11} parameter at the center frequency for different matching frequencies.

together with the decoupled SC s_{11} parameters. In the hCoil setup coils 1 and 6 are matched to ^{19}F , coils 2, 3, 4 and 5 are matched to ^1H .

The bCoil board has got a size of 110×52 mm. In Fig. 4.17 A) the small ^{13}C micro coil (coil 1) is presented along with the ^1H body coil (coil 2). Figure 4.17 B) illustrates on the right hand side how the ^{13}C coil gets inserted into the enclosing body coil. Furthermore, the full bCoil setup is visible on the left hand side of figure part B). The s_{11} parameter of the setup is presented in Fig. 4.17 C), the ^{13}C and ^1H Larmor frequencies for 1 T are marked by two grid lines. The single-channel (SC) configuration shows the s_{11} parameter for the ^{13}C and ^1H coil when they were electrically disconnected. In the multi-channel (MC) curve the connection was established.

From the s_{11} curves for all three coil setups the quality factors were extracted. The results are shown in Tab. 4.4. Furthermore, the s_{11} parameters at the corresponding resonance frequencies are shown for the single-channel case when a coil was decoupled.

In Fig. 4.18 the determination of the switching speed is illustrated. Here the RF input power was -2 dBm and the rectangular control signal had a frequency of 10 kHz. For clarity only the RF envelope and only the 21.040 MHz case is presented. The two grid lines which confine the envelope are located at 160 mV and 250 mV. The time delay between a rising edge of the control signal and the rising edge of the RF envelope was 10 μs . In addition to that the delay between a falling control and a falling envelope edge was 2 μs . In both cases the actual RF envelope transition took 2 μs . For coils resonating at 42.135 MHz and 44.790 MHz those switching characteristics were the same.



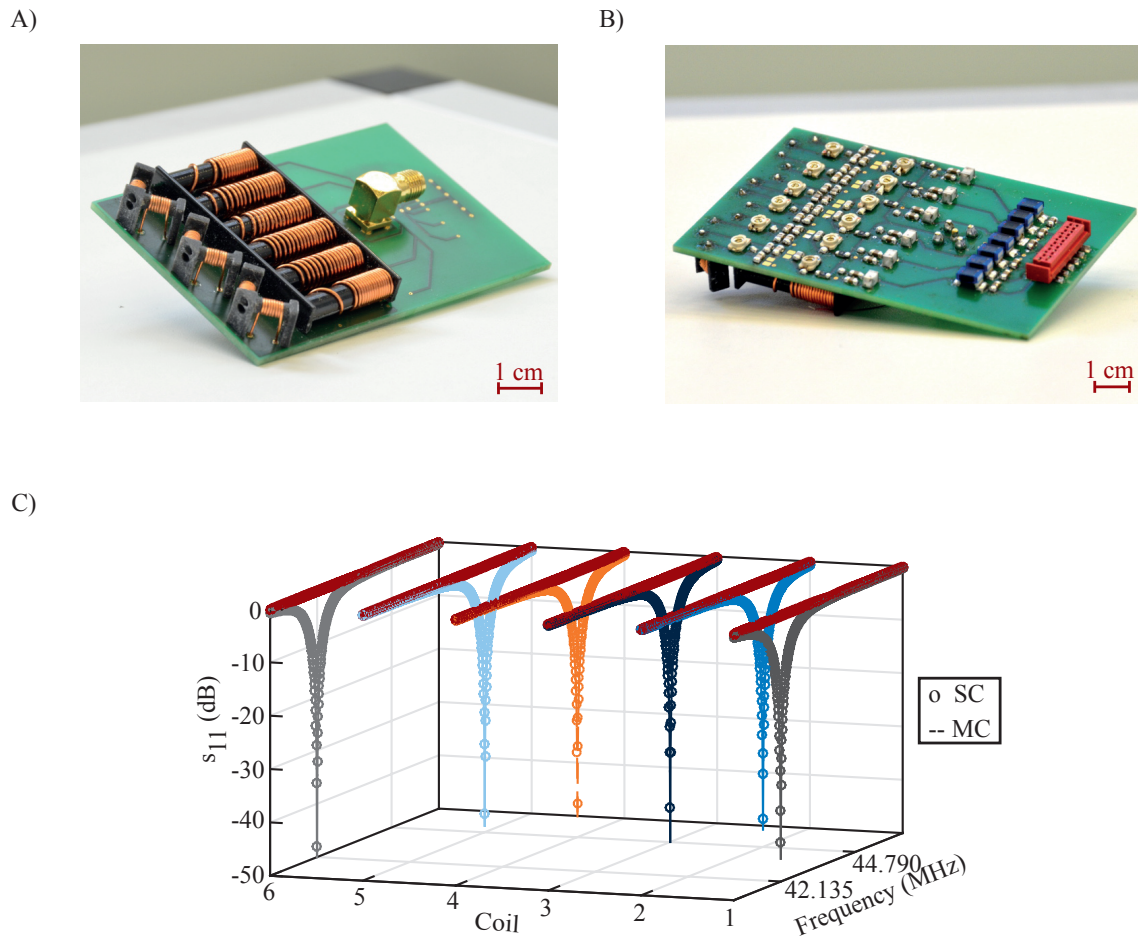


Figure 4.16: The hCoil. A) Top side. B) Bottom side. C) s_{11} parameters for the single (o) and hexa (--) channel configuration. The single-channel decoupled reflection parameter is red.

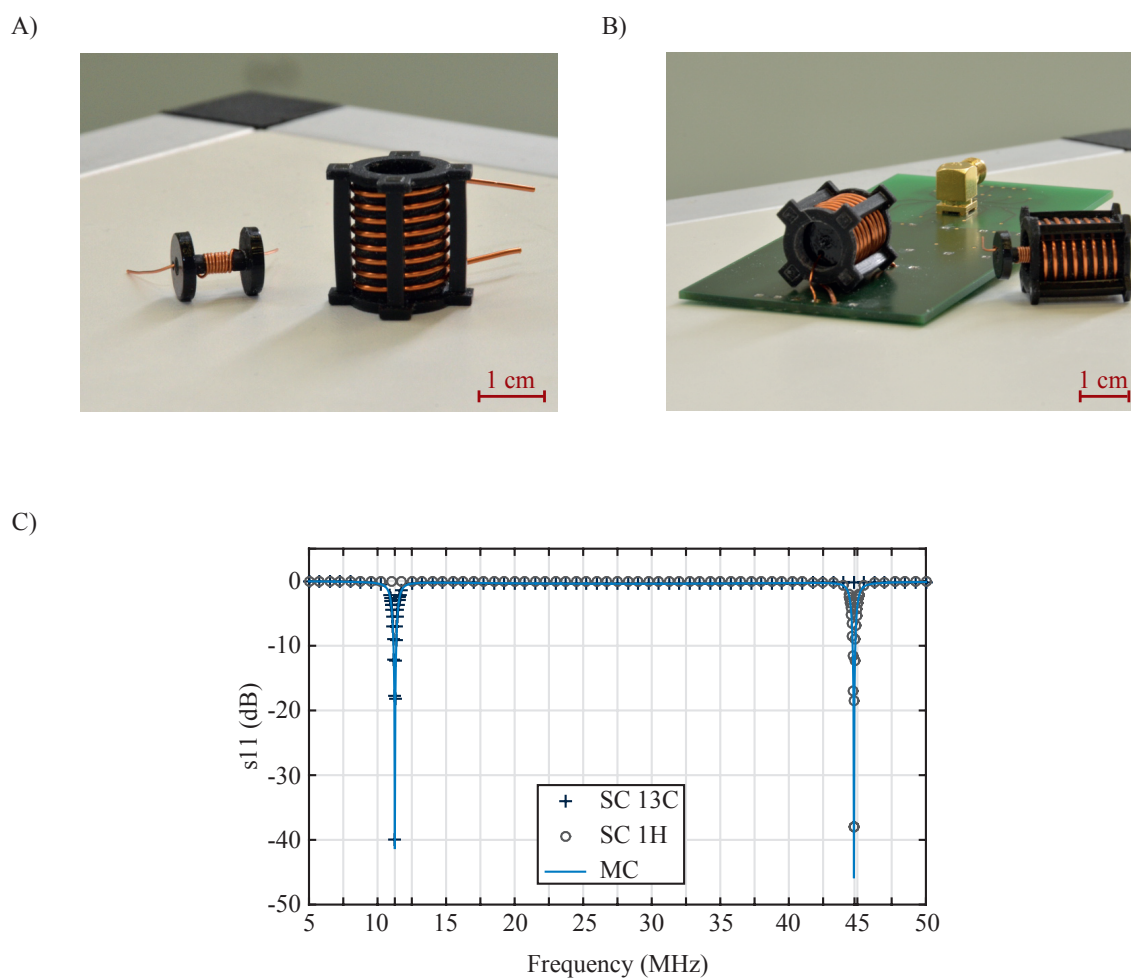


Figure 4.17: The bCoil. A) Small inlet micro coil with the enclosing body coil. B) bCoil PCB board along with a demonstration of the coil insertion. C) s_{11} parameters for the ^{13}C and ^1H coils measured in a single-channel (SC) and in a multi-channel (MC) fashion.

qCoil

| Coil | Q_{SC} | s_{11} (dB) | Q_{MC} |
|------|----------|---------------|----------|
| 1 | 50 | -0.26 | 43 |
| 2 | 48 | -0.24 | 39 |
| 3 | 49 | -0.23 | 40 |
| 4 | 49 | -0.25 | 43 |

hCoil

| Coil | Q_{SC} | s_{11} (dB) | Q_{MC} |
|------|----------|---------------|----------|
| 1 | 69 | -0.16 | 58 |
| 2 | 73 | -0.15 | 64 |
| 3 | 73 | -0.15 | 62 |
| 4 | 72 | -0.15 | 62 |
| 5 | 72 | -0.16 | 63 |
| 6 | 70 | -0.17 | 62 |

bCoil

| Coil | Q_{SC} | s_{11} (dB) | Q_{MC} |
|------|----------|---------------|----------|
| 1 | 38 | - | 38 |
| 2 | 170 | - | 159 |

Table 4.4: Comparison of the single and multi-channel Q-factors for all three coil setups along with the decoupled s_{11} parameter for the qCoil and hCoil setup.

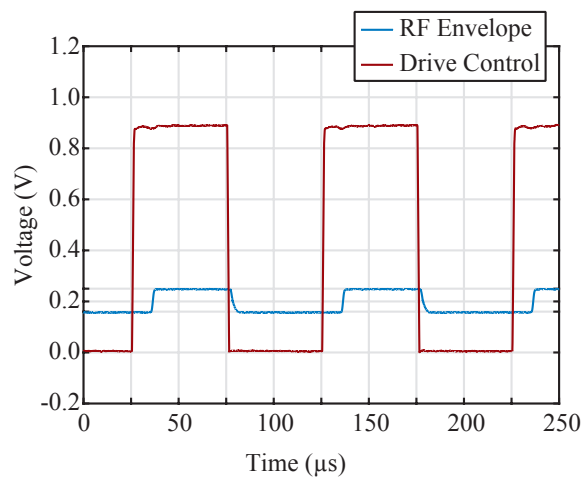


Figure 4.18: Switching speed determination at 21.040 MHz.

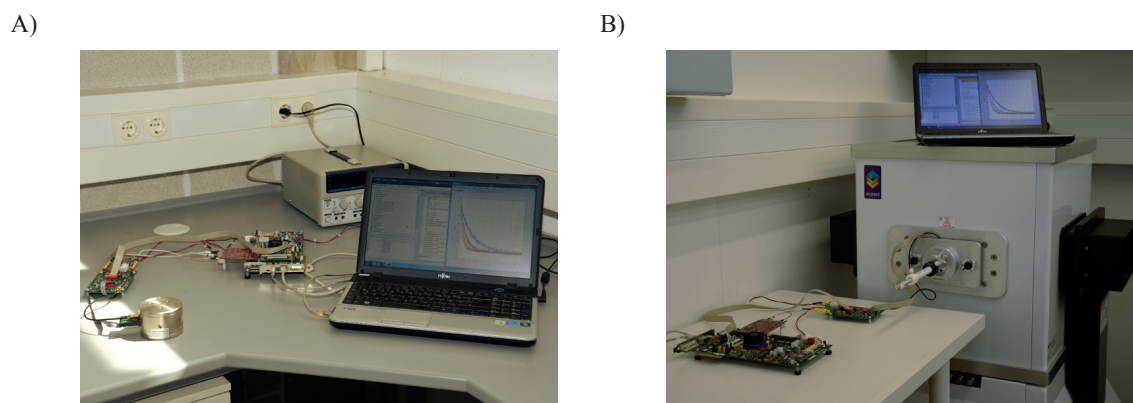


Figure 4.19: The full mNMR setup. A) Setup with the 0.5 T magnet. B) Setup with the 1 T magnet.

4.4 Results - NMR Application

4.4.1 General Setup

In Fig. 4.19 the full mNMR setup is shown. In Fig. 4.19 A) the system is working with the 0.5 T *Metrolab* magnet. The magnet is located at the bottom left corner with the coil board sticking inside. Next to the magnet one can see the analog amplification unit and the *ML605* board. The red *FMC150* mezzanine card is also visible. On the right one can see a notebook with *MATLAB* running to control the setup. In the background there is laboratory power source. The required power consumption was 3.05 A at 12 V. In Fig. 4.19 B) the mNMR setup is presented in conjunction with the 1 T magnet. In the front one can see the digital processing unit which is connected to the analog amplification board. The coils are inside the *M2* magnet, the control notebook sits on top of the magnet.

4.4.2 Quattro Channel - qCoil

In Fig. 4.20 the pulse length calibration for the qCoil setup is shown. For those experiments only the coil under investigation was loaded with H_2O . The recovery time between two individual FID acquisitions was 12.5 s. In figure part A) the FFT output of the FPGA is depicted as a function of the pulse length for coil 1 and normalized to the maximum. Figure part B) shows the integral of the spectral peak for all four coils normalized to unity. The first zero crossings - i.e. the 180° pulse length - got determined through a linear fit in the range between $10\ \mu\text{s}$ and $14\ \mu\text{s}$. The respective points in time were then divided by two to get the 90° pulse width. The results are $6.0\ \mu\text{s}$, $5.7\ \mu\text{s}$, $5.5\ \mu\text{s}$ and $6.0\ \mu\text{s}$ listed for an increasing coil number.

The coupling investigations of the qCoil setup are presented in Fig. 4.21. Figure parts A), B), C) and D) correspond to the case when only coil 1, 2, 3 or 4 was loaded respectively. Each

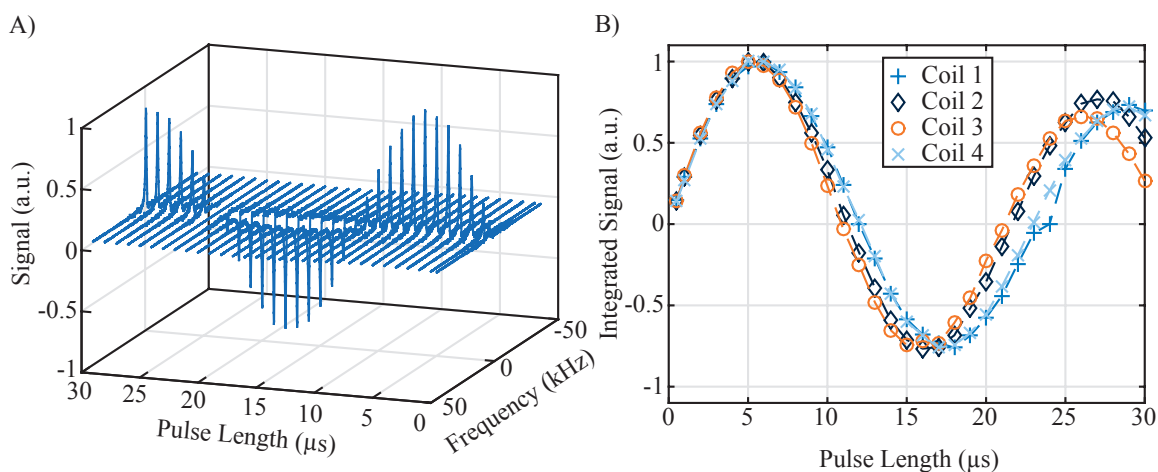


Figure 4.20: Pulse length determination of the qCoil setup. A) NMR spectra as a function of pulse length for coil 1. B) Integrated spectra for all coils as a function of the pulse length.

single figure shows four measurements whereas every measurement was followed by a recovery period of 12.5 s. The color scheme identifies the coil which was used for a FID measurement within a single figure. For example the orange signal in Fig. 4.21 D) corresponds to the case when coil 4 was loaded but a FID with coil 3 was acquired. Additionally, included in Fig. 4.21 are the red colored integrals of the spectra. The data are normalized in a way that the integrals are unity. The T_2^* times of the time domain data were analyzed by an exponential fit. The results are 322 μs , 113 μs , 103 μs and 129 μs listed here for an increasing coil number. As a side note one must add that the experienced field homogeneity, i.e. the T_2^* times, at the 0.5 T setup are dependent on the coil positioning.

In Fig. 4.22 demonstration data of the mIR and mCPMG sequence along with the single channel sequence equivalents are presented. In figure part A) a typical outcome of the mIR sequence is given where all coils got loaded with a CuSO_4 solution. The legend included in the figure assigns the 16 FID signals to the individual coils. Furthermore, the four required mIR normalization signals are presented at inversion times from 900 ms and upwards. The red circles give the normalized integral of the spectrum for each single signal. The red line presents the fit of the multi-channel inversion recovery curve. The grey crosses present the result of the single-channel outcome measured with coil 1. In the single-channel case the T_1 relaxation time was 139 ms, in the multi-channel case T_1 was 133 ms. The two additional fitting parameters a and b in the single-channel and multi-channel case were 1.01 a.u. and 1.83 a.u. as well as 1.00 a.u. and 1.58 a.u. respectively. The relaxation period between two inversions was set to 750 ms. The overall experimental time for the SC dataset was 18.0 s. For the MC dataset it was 5.7 s. Figure part B) presents the outcome of a typical mCPMG experiment (circles) along with the single-channel equivalent (crosses) when all four coils got loaded with different CuSO_4 solutions. In both cases the echo time TE was 3 ms but for

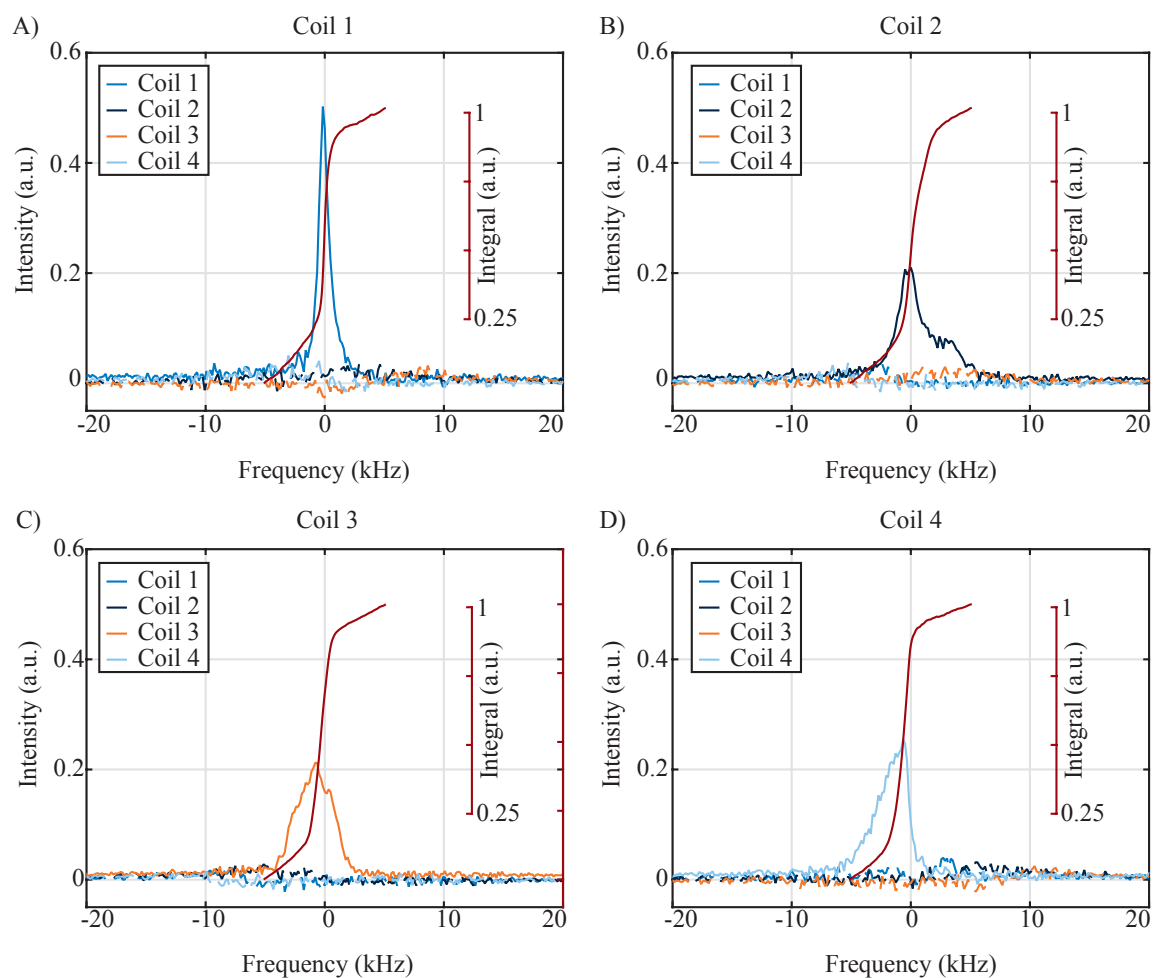


Figure 4.21: Coupling of the qCoil setup for coils 1, 2, 3 and 4 in A), B), C) and D) respectively. The data are normalized to the spectral integral shown in red.

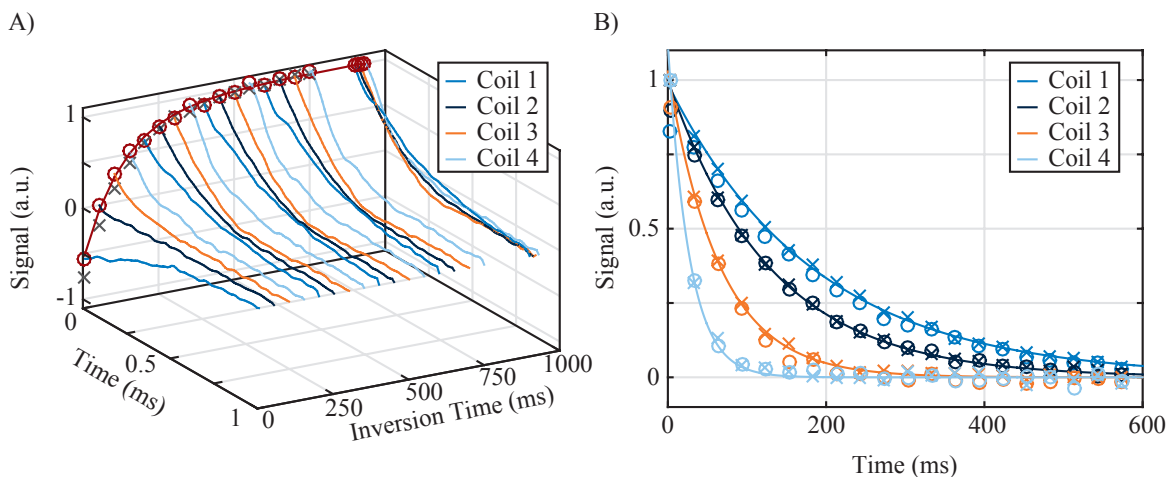


Figure 4.22: A) Demonstration of the mIR sequence. B) Demonstration of the mCPMG sequence.

clarity only every 10th data point is plotted. The solid lines give the multi-channel dataset fit. The fitted T_2 relaxation times in the single-channel case are 184 ms, 129 ms, 65 ms and 27 ms. In the multi-channel case T_2 times were 177 ms, 131 ms, 59 ms and 27 ms. In both cases the T_2 times are given for increasing coil number. Here, the full experimental time for the SC data was 3.6 s and for the MC data it was 0.9 s.

The experimental curve for the r_1 longitudinal relaxivity investigation is shown in Fig. 4.23 where the longitudinal relaxation rates are presented against the Cu^{2+} concentration. Both, the SC and the MC data set, are given with errorbars representing the standard deviation of the ten experimental runs. However, due to their size the errorbars are hardly observable. In order to determine the longitudinal relaxivity r_1 , Fig. 4.23 also contains a linear fit of the MC dataset which is presented as a red line. The fit is based on a robust least squares procedure with bisquare weights including the standard deviation. The same procedure was also applied to the SC dataset. The fitted parameters, i.e. the relaxivity r_1 and the water longitudinal relaxation rate $R_{1,0}$ in the absence of Cu^{2+} ions are given in the upper part of Tab. 4.5 along with the 95 % confidence bounds.

For the transversal SC and MC experiments the relaxation rates R_2 along with the standard deviation are given in Fig. 4.24 against the Cu^{2+} concentration for all four coils. Again, the red line represents a robust least square fit of the multi-channel dataset for every coil. The fits give the transversal relaxivity r_2 in conjunction with the Cu^{2+} -ion free transversal relaxation rate $R_{2,0}$. All fitted parameters are given in the lower part of Tab. 4.5 for the single-channel and multi-channel case, again accompanied with the 95 % confidence bounds.

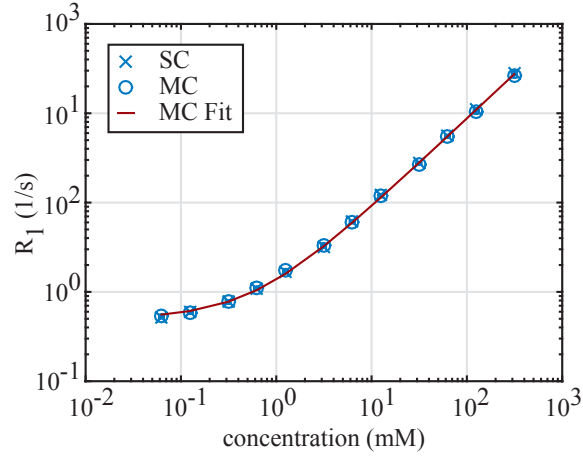


Figure 4.23: The longitudinal relaxation rates of the investigated Cu^{2+} solutions measured with a SC and a MC sequence. The red line gives a linear fit of the MC dataset.

| | SC | | MC | |
|------------------|------------------------------------|---------------------|------------------------------------|---------------------|
| | ($\text{mM}^{-1} \text{s}^{-1}$) | (s^{-1}) | ($\text{mM}^{-1} \text{s}^{-1}$) | (s^{-1}) |
| IR Data | | | | |
| Coil | r_1 | $R_{1,0}$ | r_1 | $R_{1,0}$ |
| – | 0.90 ± 0.03 | 0.48 ± 0.03 | 0.87 ± 0.03 | 0.50 ± 0.04 |
| CPMG Data | | | | |
| Coil | r_2 | $R_{2,0}$ | r_2 | $R_{2,0}$ |
| 1 | 0.97 ± 0.05 | 0.65 ± 0.03 | 0.98 ± 0.04 | 0.64 ± 0.05 |
| 2 | 1.03 ± 0.04 | 0.85 ± 0.03 | 0.98 ± 0.06 | 0.91 ± 0.06 |
| 3 | 0.99 ± 0.02 | 0.80 ± 0.02 | 0.98 ± 0.03 | 0.82 ± 0.04 |
| 4 | 1.03 ± 0.03 | 0.60 ± 0.02 | 1.00 ± 0.04 | 0.62 ± 0.06 |

Table 4.5: The fitted longitudinal and transversal relaxivities of Cu^{2+} along with the Cu^{2+} -ion free relaxation rates determined with a SC and a MC sequence.

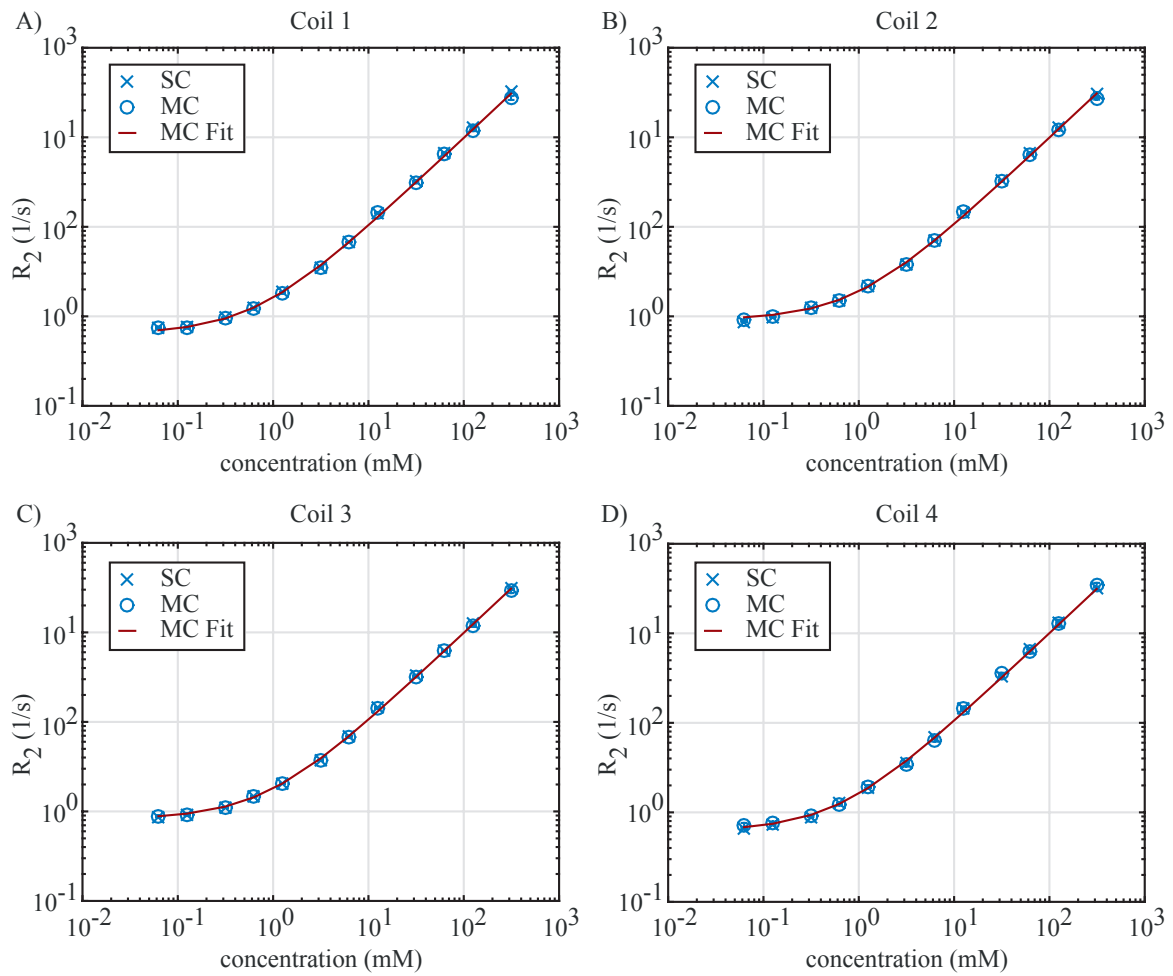


Figure 4.24: The transversal relaxation rates of the investigated Cu^{2+} solutions for all four coils measured with a SC and a MC sequence. In addition a linear fit of the MC data (red line) is shown for each coil.

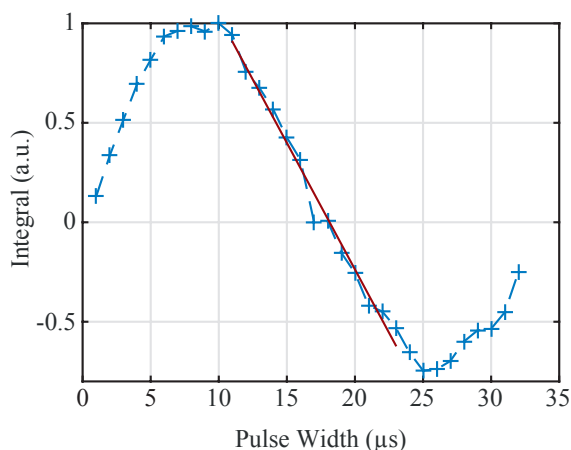


Figure 4.25: Pulse length calibration for coil 2 of the hCoil setup with H₂O.

4.4.3 Hexa Channel - hCoil

In Fig. 4.25 the integrated nutation curve of the H₂O signal of coil 2 is presented. The relaxation period between two consecutive pulses was 15 s. Again the FFT output from the FPGA was employed. The region between 11 μ s and 23 μ s was fitted by a line. The fitted zero crossing was at 18 μ s which corresponds to a 90° pulse of 9 μ s. This pulse length was also employed for the subsequent hCoil NMR experiments.

In Fig. 4.26 A), B), C), D), E) and F) the results of the single-channel and multi-channel spectroscopy experiments are shown for coils 1, 2, 3, 4, 5 and 6 respectively. The 2¹⁶-point Fourier transform of the corresponding time domain data was calculated with *MATLAB* apart from the FPGA. The vertical axis corresponds to the integral (shown in red) of each spectrum. The signals are normalized to the number of resonant nuclei in the respective molecule. In Fig. 4.26 also the chemical structure for all investigated molecules are included. The different nuclei are labeled and referenced to the corresponding spectral peaks. The H₂O Larmor frequency - already corrected to a 4.7 ppm chemical shift - during the MC experiment was at 44.780 MHz. From this it follows a ¹⁹F reference frequency of 42.135 MHz. In case of the ¹H single peak H₂O signal the linewidth was 0.4 ppm in both cases. This corresponds to a frequency of 17.9 Hz. In Fig. 4.26 A), the ¹⁹F TFE signal, also an inlet is presented where the peak is magnified in an interval of 4 ppm and centered at -80.63 ppm. The linewidth of the SC and MC peak was 0.6 ppm. This is equal to 25.3 Hz in frequency units. In addition to that the SNR, defined as the peak value divided by the root-mean-square of the noise level, got calculated for the TFE and for the H₂O peak. For the fluorine spectra the SNRs are 792.2 and 765.5. For the water spectra the results are 825.9 and 842.5. In both cases given for the SC and MC measurements respectively. The root-mean-square values, averaged for the SC and MC signals, were 0.0052 a.u. for fluorine and 0.0028 a.u. for protons.

Besides that, the investigation of the coil-to-coil B_0 field homogeneity yielded Larmor frequency differences of 5 Hz, 35.5 Hz and 66.25 Hz with respect to coil number 2. The list corresponds to coils 3, 4 and 5 respectively.

4.4.4 Dual Channel - bCoil

When simulating the expected urea NMR spectrum, both, the ^1H and the ^{13}C signal showed a single peak. The ^1H peak was located at 6.0 ppm, the ^{13}C peak was located at 161.2 ppm.

To evaluate the bCoil setup itself, as a first step Fig. 4.27 shows the spectral integral of the ^1H nutation curve integral after normalization. The waiting period between two subsequent pulses was 15 s.

After that the ^{13}C capabilities of the system were tested. In Fig. 4.28 the ^{13}C spectra of the urea sample is shown after a single measurement and after five averages where for the latter the field drift correction got employed. The linewidths of the single measurement and of the five fold averaged peaks are 5.8 ppm and 6.1 ppm respectively. The ^{13}C urea peak is located at 158 ppm. The employed B_0 tracking pulse for ^1H had a length of 33 μs . The ^{13}C pulse had a length of 9 μs . The full experiment, i.e. all five measurements together, lasted 12 min. The fitted field drift in that time was $-1.81 \mu\text{T}/\text{min}$.

In addition to that one can also investigate the SNR of both peaks. For the SC measurement the root-mean-square of the noise floor was 0.212 a.u., for the MC measurement it was 0.096 a.u.. This corresponds to SNRs of 4.7 and 10.4 respectively.

4.5 Discussion

4.5.1 System Development

Four different points must be noted when discussing the implementation of the digital processing unit. First, with respect to the resource utilization it is clear that more than six NMR processing kernels could be included in the employed *Virtex 6* FPGA. However, the precise number is hard to predict since the translation and subsequent routing of *VHDL* source code into FPGA logic is a process with many independent variables [74]. Second, the employed ADC sampling frequency would theoretically allow NMR investigations up to 122.88 MHz, for ^1H this would correspond to a B_0 field of 2.88 T. However, one should emphasize that this is rather the theoretical limit which complies to the Nyquist-Shannon sampling theorem. In general cases one chooses a sampling frequency which is a factor of three or more higher than the highest frequency component in the ADC input signal [75]. Third, in reference to the spectral widths of Fig. 4.21, the sampling frequency at the output of the last FIR in the digital chain and also the passband of this last low-pass filter could be further decreased. This would have two advantages, i.e. a alleviated memory requirement and an improvement of the SNR in the time domain, Eq. 2.17. However, when the spectral window gets decreased

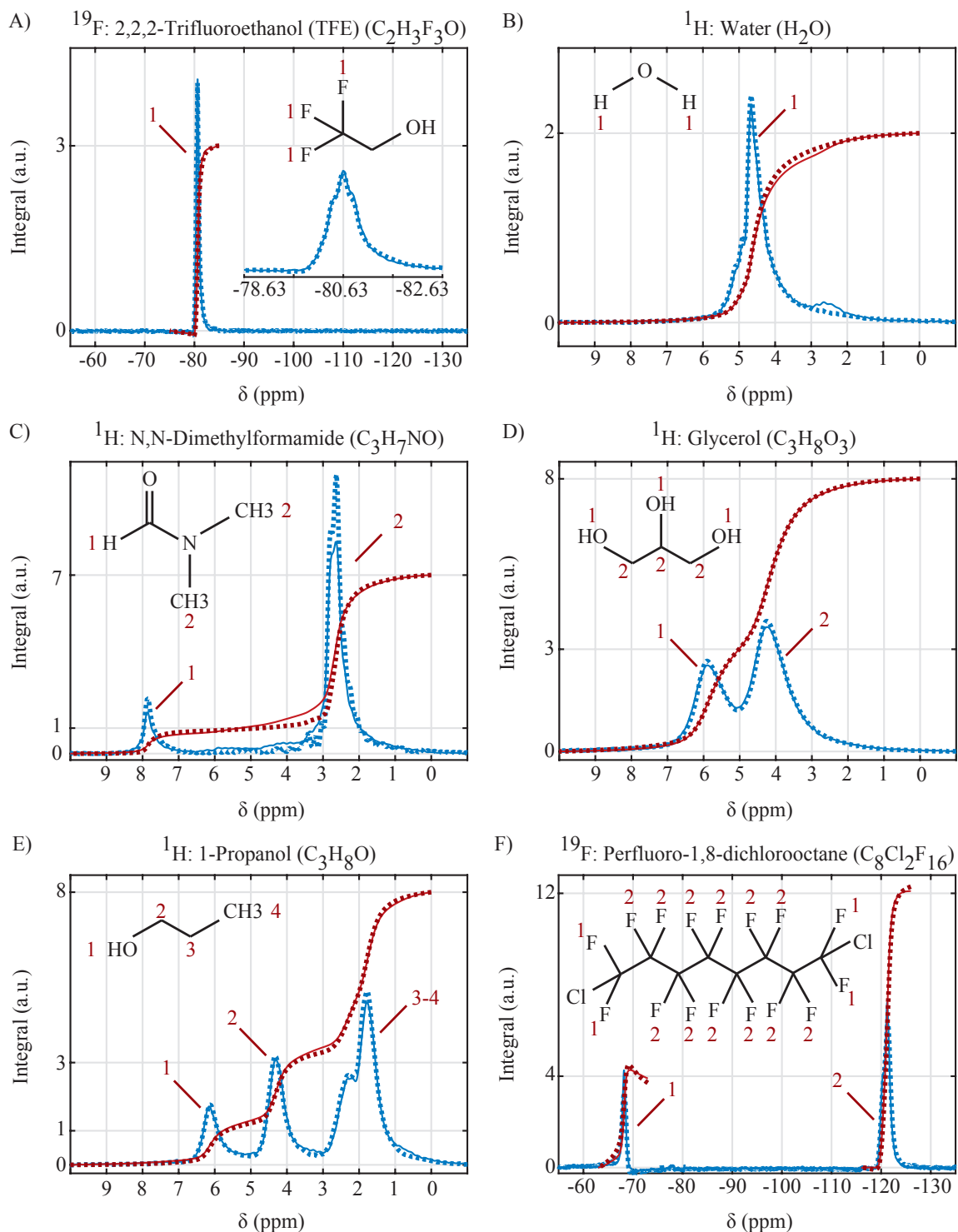


Figure 4.26: Spectroscopy with the hCoil. A), B), C), D), E) and F) show the spectra (blue) and corresponding integrals (red) of coil 1, 2, 3, 4, 5 and 6 respectively. Dotted lines represent SC results, solid lines the MC outcome. Furthermore, the structural formula of each sample, annotated with the spectral assignment, is added to the plots.

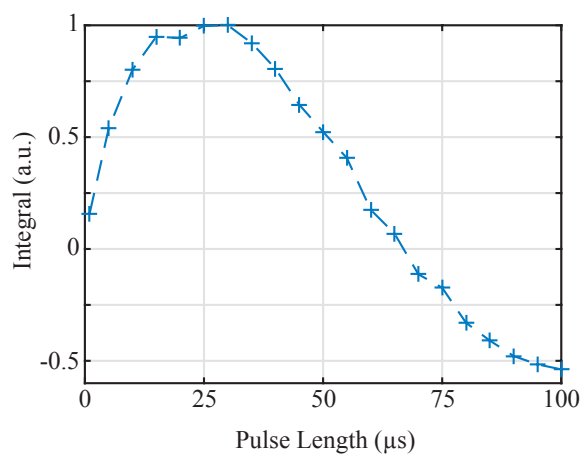


Figure 4.27: Pulse length calibration of the body coil with the ^1H signal of the urea sample.

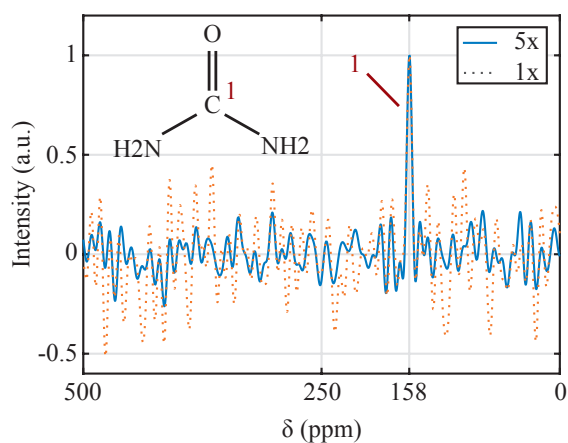


Figure 4.28: ^{13}C spectrum of 8 M enriched urea after a single shot (1x) and after five averages (5x) along with the urea structural formula.

it would also become harder to find the Larmor frequency when a significant field drift occurred. And finally, with respect to the measured switching delays of the duplexer and of the NMR coils, Fig. 4.6 and Fig. 4.18, clearly one can improve the leads of the digital control outputs. In case of the duplexer a minor incrementation from 2 μs and 10 μs to 4 μs and 10 μs would be advisable. In case of the coils switching a considerable reduction from 100 μs to 10 μs would be possible.

With respect to the Tx amplifier output, Fig. 4.11 A), several things must be noticed. First of all this is the saturation level located at 7.1 V and 6.3 V for low and high frequencies respectively. The output power limitation is caused by two different reasons, the supply voltage and the *OPA2674* gain characteristic. Since the mNMR supply voltage is 12 V the maximum peak-to-peak output voltage can not be substantially higher than this. In addition to that, the gain curve of the second Tx amplifier, i.e. the *OPA2674*, begins to drop when going from the frequency range around 20 MHz to 50 MHz hence limits the output power for the targeted ^{19}F and ^1H Larmor frequency at 1 T. In general this drop in the gain characteristic is also observable in the y-axis gap between the 21.040 MHz curve and both high frequency curves at medium input powers in Fig. 4.11 A). Additionally, one should perceive that the ^{13}C resonance output power is lower than the ^1H output for 0.5 T. This is due to the ADL5536 which has a limited output for decreasing frequencies below 20 MHz. Finally, it is important to note the linearity of the Tx output up to 2 dBm. This corresponds to a voltage amplitude of 400 mV in a 50 Ω system and is in accordance to the maximum DAC output level. With this linearity in mind it would be possible to calibrate the flip angle of NMR pulses not through the pulse length - like it was done in this work - but through the pulse height. In certain instances - e.g. in CPMG sequences - this would facilitate the sequence timing.

The Rx amplifier is characterized by Fig. 4.11 B), C) and D) as well as Tab. 4.2. Figure part B) shows the scalability of the receive gain. A functionality implemented in the mNMR system which is rather interesting for further developments of the setup. Especially when the Rx gain is supposed to be controlled through an external voltage V_{Gain} by a digital host. This would ease the handling of e.g. largely different sample volumes or concentrations, i.e. when the expected NMR signals between different specimen have got a large dynamic range.

The Rx output power as a function of the input, Fig. 4.11 C), shows two interesting features. First, this is the saturation value at 4 dBm which corresponds to an amplitude voltage of 0.5 V in a 50 Ω system. Since the AD converter has got a maximum input voltage of 1 V, this is clearly far off from being optimal. The Rx power saturation is caused by the protection diodes located at the output of the mNMR board and between the amplifier stages. For example, one could improve these protection mechanisms by replacing the fixed diodes through PIN attenuators [70]. This would allow a variable attenuation setting with respect to the required protection level. This also means one could increase the dynamic range by improving the P_{1dB} values, i.e. the upper limit of the Rx output power curve. Vice versa

one could improve the the dynamic range by decreasing the noise figure, i.e. the lower limit of the Rx output power curve.

With respect to the noise figures of the system, Tab. 4.2, one must mention that there are published NMR LNAs with noise figures well below 1 dB (see e.g. [20]). However, the noise figures given in Tab. 4.2 incorporate not only the LNA but also the duplexer and the lowpass input filter. Certainly, those two additional components will increase the noise figure. Furthermore, in general it is suggested that for many applications a noise figure of 3 dB is sufficiently good and that it makes more sense to optimize the probe SNR than the noise figure [76,77]. Additionally, it is worth noting that the mNMR Rx input stage is composed of simple and cheap standard parts, the LNA amplifier itself is integrated, characterized by its manufacturer and reliable. Besides that the full input stage is broadband, i.e. it is not only suited for a defined nuclei at a defined field strength but for a frequency range roughly between 11 MHz to 50 MHz. However, the noise figure corresponding to the targeted ^{13}C resonance is clearly higher than the remaining NF in Tab. 4.2. This can be explained by the decreased gain attributed to the high-pass filter behavior at 11.261 MHz. This is also observable in Fig. 4.11 D) and especially in Fig. 4.12 A), an attenuation before the LNA will directly contribute to the NF of the system [77]. Clearly the high-pass filter passband must get improved for a better noise figure. Additionally, this is demonstrated with the striking difference between the s_{21} parameter measured for the duplexer itself and measured in conjunction with the high-pass filter.

Besides the input attenuation a second feature is observable in Fig. 4.11 D), namely the compliance to the Nyquist-Shannon sampling theorem [78,79] which states that the sampling frequency must be at least twice as high as the maximum frequency in the signal. Since the ADC sampling frequency is nearly 250 MHz this requirement is fulfilled.

The remaining RF component on the mNMR board is the duplexer characterized by Fig. 4.12. In general one wants to have a s_{21} parameter as low as possible in the isolation case and as close as possible to zero in the feed-through case. For the isolation case the highest s_{21} was at 44.790 MHz, here 0.05 % of the Tx power will enter the Rx path. For an assumed maximum Tx power of 26 dBm this corresponds to a Rx input power of -7 dBm. Apparently this is significantly above the P_{1dB} values of the Rx chain. From that it gets clear that the main duplexer purpose is to direct the Tx power to the NMR coils. The prevention of receiver saturation of the Rx chain is primarily accomplished by the protection diodes which, however, narrow the dynamic range. Another aspect of the duplexer isolation case is the DC blocking voltage at the Rx diode. This blocking voltage may not be bigger than the negative Tx amplitude. This condition is fulfilled with the mNMR setup. In the feed-through case the measured mean s_{21} parameter for the frequencies of interest is -0.34 dB which means that 8 % of the incident power will get reflected. Apparently one can improve this by increasing the current through the PIN diode. However, this would also increase the switching duration of the duplexer since the current must rise to a higher level. When analyzing the switching

characteristics, Fig. 4.6 B), one must separate the RF envelope timing into two sections, i.e. the delay between the control signal and the envelope transition itself. The delay is an important parameter for the system setup since it can get calibrated away by an appropriate lead of the digital control signal. In contrast to that the transition duration itself cannot get calibrated away. Ideally one wants to have a transition time of zero when going from the Tx to the Rx case and reversely. This is especially true for FID experiments in inhomogeneous fields where T_2^* times are short. Here one misses an important part of the exponential FID decay during the duplexer switching. Typical T_2^* values in the B_0 field of the 0.5 T magnet are given in conjunction with Fig. 4.21. For the measured transition time of 2 μs a FID signal with a typical T_2^* time of 100 μs decayed to 98 % of the initial signal before the Rx path is on. With respect to the signal dynamic range, e.g. observable in Fig. 4.22 A), this is acceptable.

In general the micro coil setup must satisfy several requirements. It should yield a high SNR, it should generate a homogeneous B_1 field and it should be mechanically producible and stable. With the targeted sample container, i.e. the 1.50 mm diameter polyimide tubes, the sample radius and based on the 5 μl volume the sample length were fixed. The coil diameter was then defined by the stability of the 3D printed material. For the employed wall thickness of 0.4 mm still stable coil windings could be made without breaking the cylinder. The wire diameter of 0.4 mm was chosen because here the windings were mechanically stable but the wire was still thin enough to allow a high enough winding number for sufficiently high B_1 amplitudes. The winding spacing, i.e. the pitch, directly influences the proximity effect. The recommended pitch is $3r$ where r is the wire radius [33], i.e. in case of the micro coils the pitch would be 0.6 mm. However, winding distance employed here is 0.51 mm. The reason for this is the mechanical stability of the coils. When going to bigger pitches there is a higher chance to displace single coil windings due to the mechanical constraints during experiments. Consequently the coil inductance gets altered and the tuning and matching setup of the whole coil degrades. To analyze the proximity effect influence in a more detailed manner [57] gives enhancement factors ξ in dependence of the coil geometry. Those enhancement factors describe the increase of the coil resistance through the proximity effect. For the given coil geometry the ideal pitch would theoretically enhance the coil resistance by a factor of two whereas the pitch employed here leads to an enhancement of three.

To get a first impression of the employed micro coil's B_1 field, Fig. 4.13 A) and B) give an illustrative depiction. With respect to the circular border, the high field inside the coil is observable. In conjunction the field lines forming closed loops can be seen. Finally one can recognize the parallel and homogeneous behavior of the field lines inside the coil. However, for a quantitative analysis one should refer to Fig. 4.13 C) and D). First of all in figure part C) one can see that the B_1 maximum does not reach the theoretical outcome of Ampère's law. This is not surprising because Ampère's law can only give a rough estimate of a real solenoidal field, e.g. the coil length does not get considered there at all. However, since the theoretical value and the outcome of the simulation are in a close relationship, Ampère's law

can still serve to confirm the physical correctness of the simulation results. One can regard the employed sample volume of 5 μl as a cylinder with a diameter of 1.44 mm and a height of 3 mm. Hence, with respect to Fig. 4.13 C) the sample experiences a B_1 variation along its symmetry axis in the range between 1.64 mT to 2.18 mT, i.e. the B_1 field at the sample border is 25 % lower than the maximum. One should also note that the axial B_1 field is slightly asymmetric what can be explained by the helical structure of the coil. To analyze the homogeneity in the radial direction Fig. 4.13 D) is given. Especially the line located at 0.0 mm shows nearly no deviations inside the sample volume borders. In contrast to that, the radial line located at the sample border at 1.5 mm has a B_1 field in the range between 1.78 mT to 1.64 mT. From that it follows the B_1 inhomogeneity is more pronounced when regarded along the axial direction than along the radial direction. In case a more homogeneous B_1 field would be mandatory one can decrease the sample volume or increase the coil length. However, both solutions would decrease the filling factor and hence to SNR of the probe. Another solution could be to construct a solenoid with a non-constant radius, i.e. the radius of each single winding is adjusted to generate a more homogeneous excitation volume.

The complex impedances and quality factors of the micro coil and the body coil, Tab. 4.3 are in agreement with typical values in the literature [80]. Furthermore, one can see that the Q-factors increase with frequency. However, the results of Tab. 4.4 are hard to compare with the final tuning and matching since the wire residual at the coil ports also influences the impedance characteristics.

When analyzing the influence of the DC decoupling current, Fig. 4.14, one can see in figure part A) how the clear coil resonance at 21.040 MHz gets decreased, smeared out and finally vanishes. The same behavior is observable in figure part C). Here it is interesting to note that, with respect to the decoupling current of 45 mA, the s_{11} parameter for all three frequencies of interest is well in the saturation regime. For that decoupling current the s_{11} is around -0.2 dB, i.e. 5 % of the incident power get absorbed in the coil and accordingly 95 % get reflected. That means there is still some power which will enter the tuning and matching circuit of a decoupled coil. However, the actual current itself which will flow through the NMR coil and generate a B_1 field can not get determined from those data. Hence, the behavior of decoupled coils must get investigated experimentally.

With this in mind one can analyze the qCoil setup, Fig. 4.15, in more detail. The setup is compact and fits easily into a hand. Clearly, each coil can be tuned and matched to a s_{11} parameter well below -40 dB. Furthermore, the behavior of the single-channel and multi-channel curves is nearly identical. However, a closer inspection shows, Tab. 4.4, that the Q-factors in the multi-channel configuration decreased. More precisely, the mean Q-factor decreased by 16 % from 49 to 41 when going from the SC to the MC configuration. This is not surprising, due to the imperfect decoupling of the non-resonant coils they will still contribute to the single resonant coil's tuning and matching curve.

A similar reasoning applies to the hCoil setup, Fig. 4.16. Again the setup is compact and small. All coils, be it in a SC or in a MC mode, can get matched to the targeted frequency and are well below -40 dB. But again, Tab. 4.4, the Q-factors of multi-channel configuration are lower than of the single-channel configuration, namely they decreased by 14 % from 72 to 62. The percentage decline is slightly smaller than in the qCoil case although here a resonant coil is accompanied with five decoupled probes and not only with three. This is in accordance with the s_{11} parameter, Tab. 4.4, in the decoupled case. Those parameters, the mean in the hCoil case is -0.16 dB whereas the qCoil mean is -0.25 dB, are smaller for the high frequency case which means the decoupling for the high-frequency case is better. One could explain this by a better Q-factor of the decoupling circuit itself. This in turn could be either caused by a smaller resistance of the PIN diode at higher frequencies or by a higher Q-factor of the decoupling coil.

To maintain a good NMR probe setup with good signal characteristics and with good decoupling characteristics one needs a NMR coil circuit with a high Q-factor as well as a decoupling circuit with high Q-factor. Since in general the Q-factor of a solenoid rises with increasing frequency [50] - this is also observable in Tab. 4.3 - the superior decoupling behavior of the hCoil setup can be explained by this.

Finally, the bCoil setup was realized without a decoupling circuit because both resonances of interest were more than 30 MHz apart. The omission is justified by the s_{11} curve, Fig. 4.17 C), characterizing the bCoil setup. Both coils can be tuned and matched to a value below -40 dB in the single-channel and in the multi-channel case. The high impedance of the ^1H body coil at 11.261 MHz and the high impedance of the ^{13}C micro coil at 44.790 MHz are well observable. Furthermore, Tab. 4.4 shows that the ^{13}C coil has no drop in the Q-factor when going from the single-channel to the multi-channel configuration. In contrast to that the body coil experiences a small drop by 6 %.

To understand the measurement of the coil switching speed, Fig. 4.18, first of all one must analyze the voltage of the RF envelope signal given in blue. There are two cases, i.e. the coil is in a $50\ \Omega$ state and in a high impedance state. When the coil is in a $50\ \Omega$ state half of the signal generator power will get absorbed in the coil and half the power in the scope load. When the coil is in a high impedance state, it gets basically switched away from the circuit and all the signal generator power will get absorbed in the scope load. For that reason a high RF envelope corresponds to a decoupled coil and concurrently a low RF envelope signal corresponds to a coil in a $50\ \Omega$ state. Again the coil switching characteristics must be separated into two sections, the delay and the transition. Since one could calibrate away the delay through an improved lead in the digital domain it seems to be possible to even switch the signal acquisitions during different FIDs or spin echoes. This can be emphasized by comparing the transition time of $2\ \mu\text{s}$ with a typical T_2^* time of $100\ \mu\text{s}$ at 0.5 T.

The maximum number of probes is limited by several factors. For the current setup this is the number of GPIOs. Every channel requires an original PIN driver which in turn requires

an original binary control signal. The employed *ML605* board offers seven GPIOs (general purpose input/output). One GPIO is required for the duplexer control which makes six remaining GPIOs for the six channels of the hCoil setup. Through a serial-in-parallel-out (SIPO) shift register one could increase the number of binary control signals at the expense of switching speed. Another limiting factor - especially in the 0.5 T setup - is the space within the magnet. Eventually the ultimate limitation would be the Q-factor decrease like discussed above. At a certain number of channels the Q-factor decrease and hence the SNR decrease should be so significant that the parallelization gain becomes meaningless. Since the SNR is not only probe but among others also sample dependent, the identification of the maximum channel number stays an empirical question.

4.5.2 NMR Application

mNMR System With Fig. 4.19 one can estimate the general dimensions of the overall system. Clearly, the electronic mNMR setup is portable and hence suited for flexible applications. One should also emphasize that the currently employed 12 V laboratory power supply can be easily replaced by a common AC/DC adapter. Furthermore, one should emphasize that the *ML605* is a commercial evaluation board which offers a lot of functionality not needed for the current setup. That means through an original design of the digital unit, based on the same FPGA, it should be possible to considerably decrease the overall size of the digital processing unit without any degradation of the NMR capabilities.

qCoil: 4-Channel Array When calibrating the NMR flip angle, the nutation curve of the magnetization can be well observed in Fig. 4.20 A). Since a phase sensitive IQ-demodulator was employed, also negative spectral intensities are depicted. One must also draw the attention to the spectrum at a pulse length of $24 \mu\text{s}$ which is all nulled. Clearly some error occurred here. Most probably somewhere in the digital domain, since even noise is not present. Nevertheless one must note that obviously the experiment proceeded which illustrates also a slight error handling capability of the system. Besides that Fig. 4.20 B) demonstrates the spectral integral response for all four coils. The determined pulse lengths itself have got a mean of $5.8 \mu\text{s}$ which is small with respect to average T_2^* times. In addition one could even increase the Tx power and hence decrease the pulse lengths furthermore. The measurement seems to be grouped into coils 1 and 4 and coils 2 and 3. The first have got a slightly slower nutation frequency than the latter. Surprisingly this is not in accordance with Tab. 4.4 where coils 1 and 4 show a higher Q-factor than coils 2 and 3. A possible reason for this might be a minor sample misplacement. Also for permanent magnets the pulse lengths can change with time due to the B_0 field drift. When the Larmor frequency changes the RF source frequency will follow accordingly, although the probe resonance frequency is fixed. Hence, a slightly different s_{11} parameter might emerge and the pulse length will change. From that it follows another interesting point, because in terms of SNR one want to have a high Q-factor, i.e. a

narrow s_{11} dip. However, this width still must be sufficiently broad to ensure an acceptable field drift independence.

The four H₂O spectra shown in Fig. 4.21 give a first impression of the line shape and hence of the homogeneity of the 0.5 T B_0 field. Clearly coil 1 shows the highest homogeneity, i.e. the smallest line width. Both coils on the bottom side of the qCoil setup show the lowest homogeneity. What is way more important in Fig. 4.21 is the absence of coupling, i.e. no significant signal was measured with an unloaded coil. This is a very important feature of the setup since it allows to treat the micro-coil array with its four channels as four quasi independent NMR probes.

Two possible implications of this are exemplified in Fig. 4.22. In figure part A) the single-channel IR outcome is compared with the mIR outcome. First of all one must mention that in both cases for the lowest inversion time the signal build-up does not start at -1 , i.e. the 180° pulse is not perfect. This is in accordance with Fig. 4.20 and the discussion from above concerning the B_1 homogeneity. Nonetheless, the pulse imperfection effects can be attenuated by a 3-parameter fit [71] and both IR curves give nearly the same T_1 time. Typically an IR sequence is very time consuming for two reasons. Firstly the inversion times TI itself and secondly the relaxation periods TR between two consecutive inversions. Both effects can get considerably decreased with the mIR sequence due to the time-interleaving procedure. First, four investigated inversion times contribute only with the duration of the longest TI to the overall measurement time. Second, the number of required relaxation periods gets divided by four plus the normalization period. This is emphasized by the 68% shortening of the requested experimental time with the settings used here. Clearly one could even improve this by using a setup with more channels. In figure part B) the single-channel CPMG results are compared with the mCPMG outcome. The net experimental shorting of 2.7 s is really not impressive but the required time for a sample exchange is hard to be taken into account. But, one must also note that the mCPMG sequence determines four T_2 quasi simultaneously. This is especially of interest when the T_2 is expected to be a function of time, e.g. when the setup is employed in reaction monitoring.

In general, absolute relaxation times are hard to compare because paramagnetic ions (like e.g. dissolved oxygen [81]) will alter it. Furthermore, in case of T_2 , also the field homogeneity has got an influence, which is difficult to realize in a defined way with permanent magnets. For that reason, to validate the relaxation measurement outcome in a general sense, not relaxation times but relaxivity evaluations were employed.

The experimental results of the relaxivity measurements in this work, Tab. 4.5, can get compared intrinsically, i.e. between the single-channel and multi-channel case, and with respect to the results and the theory given in the literature.

To begin, an intrinsic comparison will be done. In case of the longitudinal relaxivity r_1 the single-channel ($0.90 \text{ mM}^{-1} \text{ s}^{-1}$) and multi-channel ($0.87 \text{ mM}^{-1} \text{ s}^{-1}$) results differ by 3% and also the absolute relaxation rates, i.e. $R_{1,0}$ differ by 4%. Both lie in the confidence bounds

with respect to each other. For the transversal results the mean r_2 value in the single-channel case is $1.01 \text{ mM}^{-1} \text{ s}^{-1}$ and in the multi-channel case the mean result is $0.99 \text{ mM}^{-1} \text{ s}^{-1}$. The difference is only 2% but again both results lie within the mutual confidence bounds. In case of the absolute $R_{2,0}$ rates one can clearly see the influence of the field homogeneity. In accordance to Fig. 4.21 the experienced B_0 variation for coil 2 and 3 - both coils are located at the bottom side - were higher than for the top side coils which is reflected by the higher relaxation rates for coil 2 and 3 in the single-channel and in the multi-channel case. The short T_2^* time of coil 4 is not reflected in a higher $R_{2,0}$ value here. This might be due to an imperfect sample positioning due to degradation of the coil board holder. For T_2 measurements one can suppress the influence of B_0 inhomogeneities with a short echo time. With the mNMR setup TE settings of 1 ms and below are easily possible in the SC case. However, in the MC case, the minimum echo time is limited by the time interleaving procedure. Here the minimum TE is confined by the first section of a CPMG sequence, i.e. the time from the first 90° to the first 180° pulse which is equal to $\text{TE}/2$. In reference to Fig. 4.9 C), $\text{TE}/2$ must be bigger than the number of channels times the CH parameter. This ensures that the individual coil signals do not overlap.

The influence of paramagnetic ions on relaxation times was studied since the early days of NMR. The underlying theory and experimental results are now the basis for the development of contrast media often used in MRI applications. This allows a good comparison to literature and to theory. For example already in 1959 Morgan et al. found $1.04 \text{ mM}^{-1} \text{ s}^{-1}$ for both, the longitudinal and the transversal relaxivity at a temperature of 27°C and a field of 0.47 T [82]. In 1984 Koenig et al. published a r_1 value of $0.81 \text{ mM}^{-1} \text{ s}^{-1}$ measured at 35°C and 0.5 T [47]. Finally in 1986 Bucciolini et al. published a value of $0.99 \text{ mM}^{-1} \text{ s}^{-1}$ for r_1 and a value of $1.04 \text{ mM}^{-1} \text{ s}^{-1}$ for r_2 measured at 25°C and 0.5 T [83]. Immediately one can see that the published values differ among each other but are all in the same range. This range agrees well with the results, Tab. 4.5, measured in this work.

For a detailed theoretical consideration one must refer to Eq. 2.11, Eq. 2.13 and Eq. 2.14. The relaxivity of metal ion solution depends on the binding radius r_{IS} , the binding exchange time τ_M and the correlation time τ_C as well as the Larmor frequency of the Cu^{2+} electron spin. A Cu^{2+} metal ion in an aqueous solution is surrounded by a shell of 6 coordinated H_2O molecules [46] with a binding radius of $2.7 \times 10^{-10} \text{ m}$ [84]. The mean residence lifetime τ_M of such a water molecule is $2.27 \times 10^{-10} \text{ s}$ [48]. In addition to that the electron g-factor of dissolved Cu^{2+} can be found in [85] and is 2.19. The last missing parameter is the correlation time τ_C . From the values published in [84] τ_C can get inferred at 22°C by a quadratic interpolation. This gives a correlation time of $2.80 \times 10^{-11} \text{ s}$. Those values plugged in to Eq. 2.11, Eq. 2.13 and Eq. 2.14 in conjunction with the B_0 field strength of 0.49 T and the remaining physical constants give theoretical relaxivities of $r_1 = 0.89 \text{ mM}^{-1} \text{ s}^{-1}$ and $r_2 = 0.99 \text{ mM}^{-1} \text{ s}^{-1}$. Those theoretically calculated relaxivities are in excellent agreement with the experimental results, Tab. 4.5, measured with the mNMR device.

hCoil: 6-Channel Array With the hCoil setup only single measurement FID experiments were performed. In contrast to IR or CPMG experiments, here the precise flip angle is not so important. For that reason the pulse length calibration of coil 2, Fig. 4.25, was not repeated for the remaining probes 1, 3, 4, 5 and 6. Because they are characterized by similar s_{11} parameters, Fig. 4.16 C), and the excitation powers, Fig. 4.11, at 42.135 MHz and 44.790 MHz are also comparable, hence, a similar nutation curve is expected. But still, Fig. 4.25 gives two interesting insights. First, for a 90° flip angle the pulse length is $9 \mu\text{s}$ which is very short with respect to the line width of the H_2O signal. Second, the pulse length is slightly longer than in the 0.5 T case which can be explained by the decreased output power at higher frequencies.

Like already mentioned above, the employed pulse length is not so important since it primarily influences the SNR of the spectra. With respect to Fig. 4.26 the employed quasi $\pi/2$ pulses create a sufficiently high SNR for the subsequent evaluation. Besides SNR some very interesting aspects emerge in Fig. 4.26. First of all this is the very good overlap between the single-channel and multi-channel data. Especially for coils 1, 4, 5 and 6 nearly no deviations are observable which demonstrates the good decoupling of the hCoil setup. A small spectral artifact is observable in the multi-channel H_2O spectrum, Fig. 4.26 B), located at a chemical shift δ of 2.5 ppm. This coincides with the main $\text{C}_3\text{H}_7\text{NO}$ peak from coil 3. In this coil, Fig. 4.26 C), another deviation between the single-channel and the multi-channel dataset is observable, namely the peak amplitude. Since the s_{11} parameters, Fig. 4.16 C), of coil 2 and 3 show no significant differences to the remaining coils, an error in the hCoil setup seems rather unlikely. Especially since the probes 1, 4, 5 and 6 show no coupling. Another possible explanation would be a suboptimal placement of the N,N-Dimethylformamide sample in coil 3, i.e. an experimental error. Like explained in the previous section, all samples were filled into polyimide tubes, then one tube entry was sealed with wax and finally the tube was put into the coil with the sample placed at the coil center. It would be possible that the tube of coil 3 was put too far into the coil's cylinder or the sample poured out. Then the $\text{C}_3\text{H}_7\text{NO}$ molecules, due to the orthogonal coil arrangement shown in Fig. 4.16 A), would come closer to regions where the B_1 field of coil 2 rises. Hence, a pulse to coil 2 would also excite the sample of coil 3 through the B_1 field, although the electrical decoupling through the investigated s_{11} parameters is unobtrusive. This causes an artifact peak in the spectrum of coil 2 and, due to the partly flipped magnetization of the $\text{C}_3\text{H}_7\text{NO}$ sample and the misplacement in less sensitive regions of coil 3, a decreased amplitude of the spectra in coil 3.

The virtual intersection point of the symmetry axis of coil 2 and 3 can be calculated from the center-to-center distance which was 8 mm. This gives, for an isocles right triangle, a distance of 5.7 mm from a coil center to the intersection point. With respect to Fig. 4.13 C) one can see that the B_1 field for such a distance does not completely vanish. Hence for a sample misplacement in the range of 5 mm it is likely to experience a significant sample coupling due to the B_1 field of neighboring coils.

Another interesting feature is the integral of all six plots shown in Fig. 4.26. In all cases the integral shows nicely the number of nuclei corresponding to defined peaks in the spectrum. Small deviations can be observed in Fig. 4.26 E), showing the 1-propanol data of C_3H_8O . The deviations are observable in the single-channel and in the multi-channel dataset and are most likely caused by inhomogeneities in the B_0 field.

Finally one must examine the quality of the chemical shift referencing in Fig. 4.26. Already from the homogeneity investigations with four H_2O samples it is clear that the x-axis gets more inaccurate with increasing distance from coil 2. For example the spectral difference between coil 1 and coil 5 corresponds to roughly 1.5 ppm with respect to the proton Larmor frequency. This absolute value will become more imprecise with repeated sample exchange, i.e. coil repositioning, and with field drift. Since typical 1H chemical shifts are between 0 ppm to 12 ppm [35] the inaccuracy is above 10% and significant. In contrast to that the typical chemical shift scale for ^{19}F is much broader. There, due to the strong electro-negativity of fluorine, chemical shifts between 50 ppm to -225 ppm were observed [35] which makes the inaccuracy due to an external referencing smaller than 1%. But still, this problem is not caused by the hCoil setup itself but by the B_0 homogeneity of the employed 1 T magnet.

Finally, to validate the recorded NMR spectra, three points must be observed. First of all those are the integrals shown in Fig. 4.26 which are in good agreement with the structure annotation. Secondly this is the chemical shift referencing which is imprecise due to B_0 field inhomogeneities. And thirdly the peak positions in a spectrum with respect to each other. This can be compared with the published results. Typical references for 1D NMR spectra are the *Human Metabolite Database (HMD)*, founded by several Canadian research institutes, and the *Spectral Database for Organic Compounds (SDBS)*, organized by the Japanese AIST institute. Further references are given in [86,87]. In all cases the 1H spectra agree well with the references in their general appearance. For the ^{19}F signal from coil 6 a reference could not be found. However, the chemical assignment is satisfying and makes physically.

The chemical shift was not corrected by the coil-to-coil homogeneity for coils 3, 4 and 5 to facilitate the discussion concerning B_1 coupling from above and to emphasize that all signals are referenced to coil 1. In general an improvement of the B_0 homogeneity would be desirable for two reasons: An improvement of the macroscopic homogeneity, i.e. the coil-to-coil homogeneity, would allow a more precise chemical shift referencing. Furthermore, an improvement of the microscopic homogeneity is necessary when the observation of scalar coupling is requested. Typical proton-proton coupling constants J_{H-H} have got values of just a few Hertz. For example the coupling of two protons bounded to the same carbon atom is around -12 Hz to -15 Hz, similar values are published in the case of fluorine [35].

Clearly, this is of the same order of magnitude like the experimental line widths which explains why coupling was not observed in an unambiguous quality in Fig. 4.26. To further analyze the peak width and coupling constants the inlet in Fig. 4.26 A) is presented. The TFE molecule contains three magnetically equivalent ^{19}F nuclei. Hence, a triplet is expected

with a J_{F-H} coupling constant of 8 Hz and an intensity ratio of 1 : 2 : 1 [35,88]. For the given reference frequency this coupling corresponds to 0.2 ppm. With respect to the inlet of Fig. 4.26 A), for a chemical shift in that range one can observe a broadening of the TFE center peak. Most probably this indicates the scalar spin-spin coupling. However, the resolution is clearly not high enough to further investigate the intensity ratios and the precise coupling constants, i.e. the individual peak centers of the supposed triplett. Hence the B_0 homogeneity must get improved for being able to resolve spin-spin coupling. When sticking to the same magnet a possible approach could be to use a more sophisticated shim. So far only a linear shim was employed. In addition to that, high resolution NMRS results with micro-coils are reported in [89] where the 300 MHz micro coil got susceptibility matched through immersion in a fluid. For that reason one should also examine the influence of the copper solenoid and the 3D printed material onto the magnetic field homogeneity.

In general NMRS specimen get dissolved and, hence, the SNR decreases. However, so far only undiluted samples were investigated. In case of the multi-channel measurement the TFE and H₂O peaks had a SNR of 766 and 843 respectively. From that one can estimate the influence of dilution with regard to the SNRs of the single peak signals. With respect to Eq. 2.18 the SNR is directly proportional to the sample concentration. When one defines the limit of detection at a minimum SNR of 3 [89] one can estimate the maximum dilution factors as 255 and 281 for TFE and H₂O respectively. Theoretically this would give an absolute minimum sample volume around 20 nl or a minimum sample concentration around 0.4 %, both at a field strength of 1 T.

bCoil: Body-Coil Array The NMR validation with the bCoil setup, Fig. 4.27 and Fig. 4.28, show some very interesting features of the mNMR device. First of all the the flip angle calibration, Fig. 4.27, of the ¹H body coil demonstrates that the output power of the Tx chain is able to excite NMR signals not only with the small micro coils but also with the significantly bigger body coil. Since the body coil casing had an inner diameter of 10 mm one could also think about experiments employing 10 mm NMR tubes like it is for example done with in the 0.5 T system from *Pure Devices*. With respect to the previous chapter one must note that the mNMR system possesses here a shorter pulse length than the commercial device. In addition to that one could even increase the output power of the mNMR board by decreasing the DAC scaling factor and, hence, further decrease the pulse length with the body coil.

So far, the pulse width was not optimized for a ¹³C tuned NMR probe. Since the available ¹³C excitation power is bigger than for the hCoil probes, while the Q-factor and the gyromagnetic ratio γ is smaller, a pulse length of 9 μ s was chosen.

The main purpose of the body coil was to demonstrate the field lock procedure which is necessary for low SNR measurements like the ¹³C spectroscopy experiment in Fig. 4.28. Here the determined chemical shift was 158 ppm. Since the line width was 5.8 ppm this agrees

very well with the simulation and also with the literature. For example in 2003 Ardenkjær-Larsen et al. [90] measured a chemical shift of 160 ppm when they demonstrated the dynamic nuclear polarization methods for hyperpolarized ^{13}C spectroscopy experiments. Their spin polarization is transferred from unpaired electrons to ^{13}C nuclei. Similar - but by far not as effective - polarization transfers could be realized with the bCoil setup. Here one could think about employing the nuclear Overhauser effect (NOE) to transfer polarization from ^1H to ^{13}C . In this case the theoretically maximal signal enhancement would be three [91]. Since in the case of averaging the SNR rises only by a factor of \sqrt{N} , also nicely observable with the calculated root-mean-square values, this would be superior to the five-fold averaging demonstration presented in Fig. 4.28.

Besides that it is very interesting to note that Fig. 4.28 shows the experimental detection limit of the mNMR system. In the case of the single shot measurement without any averaging the urea peak has got the highest amplitude which is roughly higher by a factor of 2 than the highest noise peak. The SNR of 5.4 is a bit above the detection limit definition. Methodically such data are hard to use and only the averaging procedure allows a clear distinction between noise and signal. Clearly, the field drift correction based on the ^1H signal, i.e. the body coil data, is preferable here. The measured field drift was $-1.81\ \mu\text{T}/\text{min}$. With respect to the mean field strength of the 1 T system this corresponds to a drift of $-1.72\ \text{ppm}/\text{min}$ which is comparable in magnitude to the measured line width of 5.8 ppm. Obviously, averaging without the ^1H based drift correction would decrease the noise level but also smear out the spectral line.

In general ^{13}C NMR substances have got a significantly longer T_1 than ^1H . To ensure a good signal relaxation a very long relaxation period was chosen for the averaging experiment. Those lengthy repetition intervals hinder the typical flip angle calibration procedures, i.e. measuring a nutation curve, and make them very time consuming. For that reason a pulse calibration was omitted since here it was only about the ^{13}C NMRS capability validation. However, there are more sophisticated methods like e.g. [72, 92] which one could implement in the mNMR system.

Commonly ^{13}C spectroscopy is accompanied by ^1H decoupling, i.e. a low power Tx pulse resonant to ^1H during ^{13}C signal acquisition, to simplify the spectral response of the system. Due to the single-channel implementation of the analog chain and especially due to the bivalent duplexer, this is not possible with the current setup. Still, since there is a second DAC output available at the *FMC150* card, a proton decoupled ^{13}C spectroscopy could get implemented.

General At last a general evaluation of the mNMR system with respect to existing hardware designs will be conducted. After more than 70 years of nuclear magnetic resonance, hardware development is still a vital field within the NMR community. During the last years

several reviews appeared which give a more general overview [18, 93]. Based on this the mNMR is distinguished to existing designs by the following aspects:

I. Mobility and hetero-nuclear capabilities:

The mNMR system is mobile and a broadband setup, i.e. it can work with hetero-nuclear samples and different field strengths. Its main components are easily portable and allow a flexible application.

There are several compact and mobile NMR systems available, e.g. shown in Fig. 3.2 A) the *Pure Devices* setup which is targeted for imaging applications. Two further examples for commercial devices would be the *Spinsolve* and the *NMR-Mouse*. Both manufactured by *magritek* (Aachen, Germany). Only for the *Spinsolve* setup hetero-nuclear capabilities are available in a single-channel fashion.

II. Multi-channel capabilities through time-multiplexing:

The mNMR system is a complete multi-channel setup with a parallelized micro-coil array. Complete means that the system consists out of a digital processing unit, an analog transceiver and the NMR probes. Through the active decoupling procedure with PIN diodes and the time-multiplexing approach only a single-channel transceiver is employed in conjunction with a digitally parallelized processing unit.

So far, several groups reported a micro-probe array, be it for high field NMR applications [94], for low-field water quantification [25], for low field T_2 applications [95] or for high-field imaging applications [26]. Only [25] and [26] deal with the complete NMR system. There multi-channel transceivers are employed. In [94] and [95] both works deal only with the probes. No complete system got developed there. Nowhere the switching between the multi-channel probe array is done via an active decoupling circuit. In [94] and [95] lossy multiplexers are employed. In [25] and [26] an active channel selection is not necessary due to the multi-channel transceiver.

III. Time-interleaved sequences:

The mNMR system comes along with specialized time-interleaved sequences for FID, T_1 and T_2 measurement. Within the literature a time-interleaved FID implementation is found in [94] for an accelerated data acquisition due to decreased relaxation periods. However, nowhere an implementation of a time interleaved mIR or mCPMG sequence was found which is intended for relaxation measurements.

5 Conclusion

This work is split into two different parts. Both are within the framework of low-field NMR applications.

The first part of the work was the development of a data processing algorithm for the analysis of 2D NMR relaxation signals. A completely new method based on Chisholm approximations was developed and validated. The applicability of the algorithm was demonstrated with simulated T_2 - T_2 and T_1 - T_2 as well as with experimental T_1 - T_2 data. The whole algorithm is the 2D extension of the Padé-Laplace method and was specifically developed for 2D relaxation data which are based on a discrete delta-like relaxation map. In such a case it was exemplified that this algorithm is superior to the state-of-the-art Tikhonov regularization method for moderate SNR. Furthermore, it also proved feasible for data which have got an underlying relaxation map with Gaussian distributions based on very narrow widths. Finally, the resolution limit of the algorithm was investigated with experimental data. There it was shown that the Chisholm approximation is able to separate two closely spaced compartments in a better way than the Tikhonov regularization method. For future work one could extend the procedure described here to more than two dimensions [66]. Eventually one could also attempt to improve the results of the Tikhonov regularization method by constraining the necessary kernel matrix with relaxation rates previously calculated with the Chisholm approach.

The second part of the project was the development of a multi-channel NMR platform. With the mNMR platform a completely new digital processing unit and an analog amplification unit were developed along with three unique micro-coil setups and tailored sequences. The system is based on a time multiplexing approach, unprecedented for low field applications. This allows a considerable reduction in the required hardware and makes the setup portable.

The results and discussion from above show several points. The mNMR is compact, mobile and broadband, i.e. it can work with different nuclei and different field strengths, defined by the rough frequency range between 11 MHz and 45 MHz. This was demonstrated by the hetero-nuclear ^1H , ^{13}C and ^{19}F measurements performed at 0.5 T and 1 T. For example, one could even extend that list by doing nuclear quadrupole resonance (NQR) experiments with ^{23}Na or by doing NMR experiments with ^{31}P or ^{15}N [73]. In the last case a higher B_0 field strength would be necessary. Furthermore, the mNMR system is multi-channel whereas only the number of miniaturized micro-coils got augmented due to the active decoupling procedure with PIN diodes. Physically, i.e. with respect to their observable external configuration, the digital processing and the analog amplification unit are quasi single-channel.

The three coil setups enclose a quattro-channel ^1H micro-coil array, a dual channel $^{13}\text{C}/^1\text{H}$ coil and a hexa-channel $^{19}\text{F}/^1\text{H}$ micro-coil array. The magnetic field of a single micro-coil was simulated with *COMSOL*. The quattro-channel setup was validated with T_1 and T_2 relaxation measurements of paramagnetic Cu^{2+} solutions at 0.5 T. Therefore unrivaled time-interleaved multi-channel IR and CPMG sequences were developed and implemented with the setup. The resulting Cu^{2+} NMR relaxivities were validated by theoretical calculations. The remaining two coils were validated with spectroscopy experiments at 1 T. The dual channel setup demonstrated the system's limit of sensitivity for ^{13}C experiments and was used for field locking procedures. With the hexa-channel setup a high throughput spectroscopy experiment was performed with ^1H and ^{19}F samples where six NMR spectra were acquired in a time less than 1 s.

For future work some procedure must be found to place the sample reliably in the homogeneous B_1 region of the coils and in addition to place the coils in the same B_0 region. Then, especially for low viscosity samples (e.g. Dimethylformamide), sample enclosing methods must get evaluated to prevent the pouring out of the sample and the evaporation. One could for example think about a micro-channel fluidic system to load the coils automatically.

From an electronic point of view one could integrate the digital processing unit and the analog amplification unit into a single custom board. This would considerably shrink the size of the system and hence further increase its mobility. Also, it should be possible to employ the concepts from this work to introduce even more channels.

Experimentally one could investigate the metabolic flux of tumor cells with ^{13}C spectroscopy but omitting the usual hyperpolarization procedure and replacing it with an nuclear Overhauser enhancement from protons. In addition, one could also build a ^{13}C micro-coil array and avoid the complications due to a the long relaxation times during averaging.

Furthermore, one could think about a novel multi-channel CPMG-like sequence for the body-coil setup were several micro-coils are inserted in a single body coil. With such a setup it would be possible to excite all micro-coil samples simultaneously through the body coil and perform a sequential echo readout with the micro-coils. This would attenuate the timing constraints from the mCPMG sequence.

Finally, one could build a "fluorine-only" micro-coil array and perform T_2 -induced binding detection experiments for biomarkers, similar to [7]. However, with the ^{19}F -array functionalized magnetic nanoparticles can get replaced through functionalized fluorine containing micelles. Such micelles are reported in imaging applications but have been not employed in NMR relaxation experiments yet [96–98]. Such an approach would allow to observe the functionalized particles and the binding state directly with the fluorine signal and not through indirect methods like in [7].

Bibliography

- [1] B. Blümich, F. Casanova, and S. Appelt, “NMR at low magnetic fields,” *Chemical Physics Letters*, vol. 477, pp. 231–240, aug 2009.
- [2] B. Luy, “Towards portable high-resolution NMR spectroscopy,” *Angewandte Chemie - International Edition*, vol. 50, no. 2, pp. 354–356, 2011.
- [3] K. Singh and B. Blümich, “NMR spectroscopy with compact instruments,” *TrAC Trends in Analytical Chemistry*, vol. 83, pp. 12–26, oct 2016.
- [4] J. Perlo, F. Casanova, and B. Blümich, “Ex situ NMR in highly homogeneous fields: ^1H spectroscopy,” *Science (New York, N.Y.)*, vol. 315, no. 5815, pp. 1110–2, 2007.
- [5] H. Wensink, F. Benito-Lopez, D. C. Hermes, W. Verboom, H. J. G. E. Gardeniers, D. N. Reinhoudt, and A. van den Berg, “Measuring reaction kinetics in a lab-on-a-chip by microcoil NMR,” *Lab on a chip*, vol. 5, no. 3, pp. 280–284, 2005.
- [6] F. Dalitz, M. Cudaj, M. Maiwald, and G. Guthausen, “Process and reaction monitoring by low-field NMR spectroscopy,” *Progress in Nuclear Magnetic Resonance Spectroscopy*, vol. 60, pp. 52–70, 2012.
- [7] H. Shao, C. Min, D. Issadore, M. Liang, T.-J. Yoon, R. Weissleder, and H. Lee, “Magnetic Nanoparticles and microNMR for Diagnostic Applications,” *Theranostics*, vol. 2, no. 1, pp. 55–65, 2012.
- [8] P. T. Callaghan, C. H. Arns, P. Galvosas, M. W. Hunter, Y. Qiao, and K. E. Washburn, “Recent Fourier and Laplace perspectives for multidimensional NMR in porous media,” *Magnetic Resonance Imaging*, vol. 25, no. 4, pp. 441–444, 2007.
- [9] D. Bernin and D. Topgaard, “NMR diffusion and relaxation correlation methods: New insights in heterogeneous materials,” *Current Opinion in Colloid & Interface Science*, vol. 18, no. 3, pp. 166–172, 2013.
- [10] Y. Q. Song, “Magnetic resonance of porous media (MRPM): A perspective,” *Journal of Magnetic Resonance*, vol. 229, pp. 12–24, 2013.
- [11] L. Venkataramanan, Y. Q. Song, and M. D. Hürlimann, “Solving Fredholm integrals of the first kind with tensor product structure in 2 and 2.5 dimensions,” *IEEE Transactions on Signal Processing*, vol. 50, no. 5, pp. 1017–1026, 2002.
- [12] K. E. Washburn and P. T. Callaghan, “Tracking pore to pore exchange using relaxation exchange spectroscopy,” *Physical Review Letters*, vol. 97, no. 17, pp. 25–28, 2006.

- [13] J. Mitchell, M. D. Hürlimann, and E. J. Fordham, “A rapid measurement of T1/T2: the DECPMG sequence.,” *Journal of magnetic resonance (San Diego, Calif. : 1997)*, vol. 200, no. 2, pp. 198–206, 2009.
- [14] M. D. Hürlimann, L. Burcaw, and Y. Q. Song, “Quantitative characterization of food products by two-dimensional D-T2 and T1-T2 distribution functions in a static gradient,” *Journal of Colloid and Interface Science*, vol. 297, no. 1, pp. 303–311, 2006.
- [15] J. Aubard, P. Levoir, A. Denis, and P. Claverie, “Direct analysis of chemical relaxation signals by a method based on the combination of Laplace transform and Padé approximants,” *Computers and Chemistry*, vol. 11, no. 3, pp. 163–178, 1987.
- [16] J. S. R. Chisholm, “Rational approximants defined from double power series,” *Mathematics of Computation*, vol. 27, no. 124, pp. 841–841, 1973.
- [17] P. R. Graves-Morris, R. H. Jones, and G. J. Makinson, “The Calculation of Some Rational Approximants in Two Variables,” *IMA Journal of Applied Mathematics*, vol. 13, pp. 311–320, jun 1974.
- [18] S. S. Zalesskiy, E. Danieli, B. Blümich, and V. P. Ananikov, “Miniaturization of NMR systems: Desktop spectrometers, microcoil spectroscopy, and ”NMR on a Chip” for chemistry, biochemistry, and industry,” *Chemical Reviews*, vol. 114, no. 11, pp. 5641–5694, 2014.
- [19] M. Sufke, A. Liebisch, B. Blümich, and S. Appelt, “External high-quality-factor resonator tunes up nuclear magnetic resonance,” *Nature Physics*, vol. 11, no. July, pp. 1–6, 2015.
- [20] N. Sun, Y. Liu, H. Lee, R. Weissleder, and D. Ham, “CMOS RF Biosensor Utilizing Nuclear Magnetic Resonance,” *IEEE Journal of Solid-State Circuits*, vol. 44, pp. 1629–1643, may 2009.
- [21] D. Ha, J. Paulsen, N. Sun, Y.-Q. Song, and D. Ham, “Scalable NMR spectroscopy with semiconductor chips,” *Proceedings of the National Academy of Sciences*, vol. 111, no. 33, pp. 11955–11960, 2014.
- [22] P. P. Stang, S. M. Conolly, J. M. Santos, J. M. Pauly, and G. C. Scott, “Medusa: A scalable MR console using USB,” *IEEE Transactions on Medical Imaging*, vol. 31, no. 2, pp. 370–379, 2012.
- [23] O. G. Gruschke, N. Baxan, L. Clad, K. Kratt, D. von Elverfeldt, A. Peter, J. Hennig, V. Badilita, U. Wallrabe, and J. G. Korvink, “Lab on a chip phased-array MR multiplatform analysis system,” *Lab Chip*, vol. 12, no. 3, pp. 495–502, 2012.

- [24] H. Chen, S. Viel, F. Ziarelli, and L. Peng, "19F NMR: a valuable tool for studying biological events," *Chemical Society Reviews*, vol. 42, no. 20, p. 7971, 2013.
- [25] K. Ogawa, Y. Yokouchi, T. Haishi, and K. Ito, "Development of an eight-channel NMR system using RF detection coils for measuring spatial distributions of current density and water content in the PEM of a PEFC," *Journal of Magnetic Resonance*, vol. 234, pp. 147–153, 2013.
- [26] D. Oligschlaeger, S. Lehmkuhl, J. Watzlaw, S. Benders, E. De Boever, C. Rehorn, M. Vossel, U. Schnakenberg, and B. Bluemich, "Miniaturized multi-coil arrays for functional planar imaging with a single-sided NMR sensor," *Journal of Magnetic Resonance*, vol. 254, pp. 10–18, 2015.
- [27] I. I. Rabi, J. R. Zacharias, S. Millman, and P. Kusch, "A New Method of Measuring Nuclear Magnetic Moment," *Physical Review*, vol. 53, pp. 318–318, feb 1938.
- [28] F. Bloch, W. W. Hansen, and M. Packard, "The Nuclear Induction Experiment," *Physical Review*, vol. 70, pp. 474–485, oct 1946.
- [29] E. M. Purcell, H. C. Torrey, and R. V. Pound, "Resonance Absorption by Nuclear Magnetic Moments in a Solid," *Physical Review*, vol. 69, pp. 37–38, jan 1946.
- [30] W. G. Proctor and F. C. Yu, "The Dependence of a Nuclear Magnetic Resonance Frequency upon Chemical Compound," *Physical Review*, vol. 77, pp. 717–717, mar 1950.
- [31] R. R. Ernst and W. A. Anderson, "Application of Fourier Transform Spectroscopy to Magnetic Resonance," *Review of Scientific Instruments*, vol. 37, pp. 93–102, jan 1966.
- [32] P. C. Lauterbur, "Image Formation by Induced Local Interactions: Examples Employing Nuclear Magnetic Resonance," *Nature*, vol. 242, pp. 190–191, mar 1973.
- [33] D. Hoult and R. Richards, "The signal-to-noise ratio of the nuclear magnetic resonance experiment," *Journal of Magnetic Resonance*, vol. 213, no. 2, pp. 329–343, 2011.
- [34] F. Bloch, W. W. Hansen, and M. Packard, "Nuclear Induction," *Physical Review*, vol. 69, pp. 127–127, feb 1946.
- [35] E. D. Becker, *High Resolution NMR: Theory and Chemical Applications*. ELSEVIER LTD, 1999.
- [36] E. L. Hahn, "Nuclear Induction Due to Free Larmor Precession," *Physical Review*, vol. 77, pp. 297–298, jan 1950.
- [37] H. Y. Carr and E. M. Purcell, "Effects of Diffusion on Free Precession in Nuclear Magnetic Resonance Experiments," *Physical Review*, vol. 94, pp. 630–638, may 1954.

- [38] S. Meiboom and D. Gill, “Modified Spin Echo Method for Measuring Nuclear Relaxation Times,” *Review of Scientific Instruments*, vol. 29, pp. 688–691, aug 1958.
- [39] E. L. Hahn, “Spin Echoes,” *Physical Review*, vol. 80, pp. 580–594, nov 1950.
- [40] H. C. Torrey, “Bloch equations with diffusion terms,” *Physical Review*, vol. 104, no. 3, pp. 563–565, 1956.
- [41] J. Mitchell, L. F. Gladden, T. C. Chandrasekera, and E. J. Fordham, “Low-field permanent magnets for industrial process and quality control,” *Progress in Nuclear Magnetic Resonance Spectroscopy*, vol. 76, pp. 1–60, 2014.
- [42] Y.-Q. Song, L. Venkataramanan, M. Hürlimann, M. Flaum, P. Frulla, and C. Straley, “T1 - T2 Correlation Spectra Obtained Using a Fast Two-Dimensional Laplace Inversion,” *Journal of Magnetic Resonance*, vol. 154, no. 2, pp. 261–268, 2002.
- [43] N. Bloembergen, E. M. Purcell, and R. V. Pound, “Relaxation effects in nuclear magnetic resonance absorption,” *Physical Review*, vol. 73, no. 7, pp. 679–712, 1948.
- [44] A. Abragam and R. V. Pound, “Influence of Electric and Magnetic Fields on Angular Correlations,” *Physical Review*, vol. 92, pp. 943–962, nov 1953.
- [45] I. Solomon, “Relaxation Processes in a System of Two Spins,” *Physical Review*, vol. 99, pp. 559–565, jul 1955.
- [46] L. Banci, I. Bertini, and C. Luchinat, *Nuclear and Electron Relaxation: The Magnetic Nucleus-Unpaired Electron Coupling in Solution*. Wiley-VCH, 1991.
- [47] S. H. Koenig and R. D. Brown, “Relaxation of solvent protons by paramagnetic ions and its dependence on magnetic field and chemical environment: implications for NMR imaging,” *Magnetic resonance in medicine*, vol. 1, pp. 478–95, dec 1984.
- [48] L. Helm and A. E. Merbach, “Inorganic and Bioinorganic Solvent Exchange Mechanisms,” *Chemical Reviews*, vol. 105, pp. 1923–1960, jun 2005.
- [49] R. Ludwig and G. Bogdanov, *RF Circuit Design: Theory and Applications*. Prentice Hall, 2008.
- [50] M. Lupu, A. Briguët, and J. Mispelster, *NMR Probeheads: For Biophysical and Biomedical Experiments*. Imperial College, 2006.
- [51] J. Murphy-Boesch and A. P. Koretsky, “An in Vivo NMR probe circuit for improved sensitivity,” *Journal of Magnetic Resonance*, vol. 54, no. 3, pp. 526–532, 1983.
- [52] W. A. Edelstein, C. J. Hardy, and O. M. Mueller, “Electronic decoupling of surface-coil receivers for NMR imaging and spectroscopy,” *Journal of Magnetic Resonance (1969)*, vol. 67, no. 1, pp. 156–161, 1986.

- [53] E. A. Barberi, J. S. Gati, B. K. Rutt, and R. S. Menon, "A transmit-only/receive-only (TORO) RF system for high-field MRI/MRS applications," *Magnetic Resonance in Medicine*, vol. 43, no. 2, pp. 284–289, 2000.
- [54] J. Lutz, H. Schlangenotto, U. Scheuermann, and R. D. Doncker, *Semiconductor Power Devices*. Springer-Verlag GmbH, 2011.
- [55] D. M. Pozar, *Microwave Engineering*. Wiley, 2011.
- [56] H. Heuermann, *Hochfrequenztechnik: Komponenten für High-Speed- und Hochfrequenzschaltungen(vormals: Lineare Komponenten hochintegrierter Hochfrequenzschaltungen) (German Edition)*. Vieweg+Teubner Verlag, 2009.
- [57] K. R. Minard and R. A. Wind, "Solenoidal microcoil design - Part II: Optimizing winding parameters for maximum signal-to-noise performance," *Concepts in Magnetic Resonance*, vol. 13, no. 3, pp. 190–210, 2001.
- [58] J. Mispelter, M. Lupu, and A. Briguet, *NMR Probeheads for Biophysical and Biomedical Experiments:Theoretical Principles and Practical Guidelines*. ICP, 2015.
- [59] S. Huber, A. Haase, and B. Gleich, "Analysis of 2D NMR relaxation data using Chisholm approximations," *Journal of Magnetic Resonance*, vol. 281, pp. 66–74, aug 2017.
- [60] J. Mitchell, T. C. Chandrasekera, and L. F. Gladden, "Numerical estimation of relaxation and diffusion distributions in two dimensions," *Progress in Nuclear Magnetic Resonance Spectroscopy*, vol. 62, pp. 34–50, 2012.
- [61] E. Yeramian and P. Claverie, "Analysis of multiexponential functions without a hypothesis as to the number of components," *Nature*, vol. 326, no. 6109, pp. 169–174, 1987.
- [62] Y.-Q. Song, G. Carneiro, L. M. Schwartz, and D. L. Johnson, "Experimental Identification of Diffusive Coupling Using 2D NMR," *Physical Review Letters*, vol. 113, p. 235503, dec 2014.
- [63] E. Fordham, A. Sezginer, and L. Hall, "Imaging Multiexponential Relaxation in the (y, Log T1) Plane, with Application to Clay Filtration in Rock Cores," 1995.
- [64] S. Ahola, V. V. Zhivonitko, O. Mankinen, G. Zhang, A. M. Kantola, H.-Y. Chen, C. Hilty, I. V. Koptuyug, and V.-V. Telkki, "Ultrafast multidimensional Laplace NMR for a rapid and sensitive chemical analysis," *Nature communications*, vol. 6, p. 8363, 2015.
- [65] D. Benjamini and P. J. Basser, "Use of marginal distributions constrained optimization (MADCO) for accelerated 2D MRI relaxometry and diffusometry," *Journal of Magnetic Resonance*, vol. 271, pp. 40–45, oct 2016.

- [66] R. Hughes Jones, "General rational approximants in N-variables," *Journal of Approximation Theory*, vol. 16, no. 3, pp. 201–233, 1976.
- [67] S. Huber, C. Min, C. Staat, J. Oh, C. M. Castro, A. Haase, R. Weissleder, B. Gleich, and H. Lee, "Biosensors and Bioelectronics Multichannel digital heteronuclear magnetic resonance biosensor," *Biosensors and Bioelectronics*, vol. 126, no. October 2018, pp. 240–248, 2019.
- [68] S. Huber, *Entwicklung eines mehrkanaligen NMR-Spektrometers zur Detektion von Biomolekülen durch T2-Analyse*. Diploma thesis, TU Munich, 2012.
- [69] D. Seeber, "Positive-intrinsic-negative diode-based duplexer for microcoil nuclear magnetic resonance," *Review of Scientific Instruments*, vol. 71, no. 2000, pp. 2908–2913, 2000.
- [70] J. F. White, *Microwave Semiconductor Engineering*. Dordrecht: Springer Netherlands, 1982.
- [71] P. B. Kingsley, "Signal Intensities and T1 Calculations in Multiple-Echo Sequences with Imperfect Pulses," *Concepts in Magnetic Resonance*, vol. 11, no. 1, pp. 29–49, 1999.
- [72] S. Berger and S. Braun, *200 and More NMR Experiments*. Wiley VCH Verlag GmbH, 2004.
- [73] R. K. Harris, E. D. Becker, S. M. Cabral De Menezes, R. Goodfellow, and P. Granger, "NMR nomenclature: Nuclear spin properties and conventions for chemical shifts (IUPAC recommendations 2001)," *Concepts in Magnetic Resonance Part A: Bridging Education and Research*, vol. 14, no. 5, pp. 326–346, 2002.
- [74] F. Kesel and R. Bartholomä, *Entwurf von digitalen Schaltungen und Systemen mit HDLs und FPGAs*. Gruyter, de Oldenbourg, 2013.
- [75] R. G. Lyons, *Understanding Digital Signal Processing*. ADDISON WESLEY PUB CO INC, 2010.
- [76] C. D. Motchenbacher and J. A. Connelly, *Low-Noise Electronic System Design*. JOHN WILEY & SONS INC, 1993.
- [77] G. Vasilescu, *Electronic Noise and Interfering Signals*. Springer-Verlag GmbH, 2004.
- [78] H. Nyquist, "Certain topics in telegraph transmission theory," *Proceedings of the IEEE*, vol. 90, no. 2, pp. 280–305, 2002.
- [79] C. Shannon, "Communication in the Presence of Noise," *Proceedings of the IRE*, vol. 37, pp. 10–21, jan 1949.

- [80] S. Jeong, R. Eskandar, S. M. Park, J. Alvarez, S. S. Tee, R. Weissleder, M. G. Kharas, H. Lee, and K. R. Keshari, "Real-time quantitative analysis of metabolic flux in live cells using a hyperpolarized micromagnetic resonance spectrometer," *Sci. Adv.*, vol. 3, no. June, p. e1700341, 2017.
- [81] K. Krynicki, "Proton spin-lattice relaxation in pure water between 0degC and 100degC," *Physica*, vol. 32, no. 1, pp. 167–178, 1966.
- [82] L. O. Morgan and A. W. Nolle, "Proton Spin Relaxation in Aqueous Solutions of Paramagnetic Ions. II. Cr $^{+++}$, Mn $^{++}$, Ni $^{++}$, Cu $^{++}$, and Gd $^{+++}$," *The Journal of Chemical Physics*, vol. 31, pp. 365–368, aug 1959.
- [83] M. Bucciolini, L. Ciraolo, and R. Renzi, "Relaxation rates of paramagnetic solutions: Evaluation by nuclear magnetic resonance imaging," *Medical Physics*, vol. 13, pp. 298–303, may 1986.
- [84] R. Hausser and F. Noack, "Kernmagnetische Relaxation und Korrelation in Zwei-Spin-Systemen," *Zeitschrift fuer Physik*, vol. 182, pp. 93–110, feb 1964.
- [85] P. M. Schosseler, B. Wehrli, and A. Schweiger, "Complexation of Copper(II) with Carbonate Ligands in Aqueous Solution: A CW and Pulse EPR Study," *Inorganic Chemistry*, vol. 36, pp. 4490–4499, sep 1997.
- [86] C. Pouchert and J. Campbell, *The Aldrich Library of NMR spectra 1-11*. Milwaukee: Aldrich Chemical Co., 1974.
- [87] W. Simons, *The Sadtler handbook of proton NMR spectra*. Philadelphia: Sadtler Research Laboratories, 1978.
- [88] B. S. Selinsky, D. E. Rusyniak, J. O. Warsheski, and A. P. Joseph, "19F nuclear magnetic resonance analysis of trifluoroethanol metabolites in the urine of the Sprague-Dawley rat," *Biochemical Pharmacology*, vol. 42, no. 11, pp. 2229–2238, 1991.
- [89] D. L. Olson, T. L. Peck, A. G. Webb, R. L. Magin, and J. V. Sweedler, "High-Resolution Microcoil 1H-NMR for Mass-Limited, Nanoliter-Volume Samples," *Science*, vol. 270, pp. 1967–1970, dec 1995.
- [90] J. H. Ardenkjaer-Larsen, B. Fridlund, A. Gram, G. Hansson, L. Hansson, M. H. Lerche, R. Servin, M. Thaning, and K. Golman, "Increase in signal-to-noise ratio of $> 10,000$ times in liquid-state NMR," *Proceedings of the National Academy of Sciences*, vol. 100, pp. 10158–10163, sep 2003.
- [91] D. Neuhaus and M. P. Williamson, *The Nuclear Overhauser Effect in Structural and Conformational Analysis, 2nd Edition*. Wiley-VCH, 2000.

- [92] R. F. Schulte, L. Sacolick, M. H. Deppe, M. A. Janich, M. Schwaiger, J. M. Wild, and F. Wiesinger, "Transmit gain calibration for nonproton MR using the Bloch-Siegert shift," *NMR in Biomedicine*, vol. 24, no. 9, pp. 1068–1072, 2011.
- [93] A. G. Webb, "Radiofrequency microcoils for magnetic resonance imaging and spectroscopy," *Journal of Magnetic Resonance*, vol. 229, pp. 55–66, 2013.
- [94] Y. Li, A. M. Wolters, P. V. Malawey, J. V. Sweedler, and A. G. Webb, "Multiple solenoidal microcoil probes for high-sensitivity, high-throughput nuclear magnetic resonance spectroscopy," *Analytical chemistry*, vol. 71, no. 21, pp. 4815–4820, 1999.
- [95] H. Lee, E. Sun, D. Ham, and R. Weissleder, "Chip-NMR biosensor for detection and molecular analysis of cells," *Nature Medicine*, vol. 14, no. 8, pp. 869–874, 2008.
- [96] J. Janjic and E. Ahrens, "Fluorine containing nanoemulsions for MRI cell tracking," *WIREs Nanomedicine and Nanobiotechnology*, pp. 492–501, 2009.
- [97] S. Patel, J. Williams, and J. Janjic, "Cell Labeling for ^{19}F MRI: New and Improved Approach to Perfluorocarbon Nanoemulsion Design," *Biosensors*, vol. 3, pp. 341–359, sep 2013.
- [98] A. M. Morawski, P. M. Winter, X. Yu, R. W. Fuhrhop, M. J. Scott, F. Hockett, J. D. Robertson, P. J. Gaffney, G. M. Lanza, and S. A. Wickline, "Quantitative "magnetic resonance immunohistochemistry" with ligand-targeted ^{19}F nanoparticles," *Magnetic Resonance in Medicine*, vol. 52, pp. 1255–1262, dec 2004.

6 Appendix

6.1 Coil Matching Capacitances

In Tab. 6.1 the installed capacitances C_M , C_T and C_S as well as the number of decoupling coil turns N are given for the tuning and matching of the three developed coil arrays.

| qCoil: 4-Channel Array | | | | |
|-------------------------------|------------|------------|------------|----|
| Coil | C_M (pF) | C_T (pF) | C_S (pF) | N |
| 1 | T* + 70 | T + 610 | 100 | 29 |
| 2 | T + 70 | T + 610 | 100 | 29 |
| 3 | T + 70 | T + 610 | 100 | 29 |
| 4 | T + 70 | T + 610 | 100 | 29 |

| hCoil: 6-Channel Array | | | | |
|-------------------------------|------------|------------|------------|----|
| Coil | C_M (pF) | C_T (pF) | C_S (pF) | N |
| 1 | T + 20 | T + 135 | 30 | 16 |
| 2 | T + 15 | T + 110 | 25 | 17 |
| 3 | T + 15 | T + 110 | 25 | 17 |
| 4 | T + 15 | T + 110 | 25 | 17 |
| 5 | T + 15 | T + 110 | 25 | 17 |
| 6 | T + 20 | T + 135 | 30 | 16 |

| bCoil: Body-Coil Array | | | | |
|-------------------------------|------------|------------|------------|---|
| Coil | C_M (pF) | C_T (pF) | C_S (pF) | N |
| 1 | T | T + 10 | 10 | – |
| 2 | T + 210 | T + 1430 | 220 | – |

* Trimmer

Table 6.1: Installed capacitances and number of decoupling coil turns for the qCoil, hCoil and bCoil setup.

6.2 DVD

Attached to this work there is a DVD which contains four folders. Those folders include the design files of the mNMR system like explained below:

FPGA:

Xilinx ISE Project with all VHDL and C source code for the digital processing unit

MATLAB:

MATLAB scripts to communicate with the digital processing unit

PCB:

Altium schematic and layout files of the analog amplification unit and all coil boards

SolidWorks:

SolidWorks projects files for all coil casings and board holders

6.3 RF Characterization Instruments

Tab. 6.2 gives a list of the major instruments which were used for the RF characterization of the mNMR analog amplification unit.

| Instrument | Type |
|-----------------------|--|
| Signal Generator | Rohde & Schwarz SMB 100A Agilent 33120 A |
| Noise Figure Analyzer | Agilent N8973A |
| Spectrum Analyzer | Agilent CXA Signal Analyzer N9000A |
| Network Analyzer | Agilent E5061A |
| Oscilloscope | LeCroy waveSurfer 44MXs Agilent InfiniiVision DSO-X 3054A |

Table 6.2: Instruments used for the RF characterization of the mNMR analog amplification unit.

7 List of Publications

Peer-Reviewed Articles

- S. Huber, A. Haase, B. Gleich: Analysis of 2D NMR relaxation data using Chisholm approximations. *Journal of Magnetic Resonance*, 281:66-74, (2017)
- S. Huber, C. Min, C. Staat, J. Oh, C. Castro, A. Haase, R. Weissleder, B. Gleich, H. Lee: Multichannel Digital Heteronuclear Magnetic Resonance Biosensor. *Biosensors and Bioelectronics*, 126:240-248, (2019)

Conference Contributions

- S. Huber, B. Gleich, A. Haase: Portable Multi-Coil NMR Relaxometer: 13th International Conference on Magnetic Resonance Microscopy, Munich, 2015 (poster award)
- S. Huber, A. Joos, B. Gleich, A. Haase: Homodyne Relaxation Analysis: 13th International Conference on Magnetic Resonance in Porous Media, Bologna, 2016 (poster)

8 Acknowledgments

At the beginning I would like to thank my wife Sophia and my son Leopold. During a PhD it is inevitable to come into a grumpy (a mean really grumpy) mood. Nevertheless Sophia supported me unconditionally whenever it was possible and bore my grumpiness whenever I was "impossible". And Poldi, he taught me that there is really way more to see than work, especially at three o'clock at night, every night.

Next I would like to thank my parents Angela and Hermann for their support and their help when daycare was closed. It is always nice to have a tractor in the garage. The same holds true for my parents in law Inge and Ernst (it is always nice to have a camper in the garage) and for my brother Hermann, his wife Johanna and my sister Eva (it is always nice to use a giant box as a garage).

Then I would like to thank all colleagues from the IMETUM/MSB who helped me with my PhD. Especially Bernhard Gleich who made it possible at all. Furthermore I would like to thank Axel Haase, Alexandra Heidsieck, Christine Rümenapp, Norbert Gattinger, Nicole Donant and Roman Rahm. But of course also Alexander Joos, Christoph Staat and Andreas Wegemann who shared similar problems during their work and who shared some time with me playing table soccer. Special thanks go here to my "Kolleche" Christoph Staat for his help with the PIN decoupling circuits and for his defense work during a 10 : 0 victory. Then I also would like to thank Christian Hundshammer from the Klinikum Rechts der Isar for the ^{13}C urea sample and the very helpful discussions.

Next I would like to thank Katharina Scholz and Kristina Kindl for their administrative support. I also would like to thank Susanne Schnell-Witteczek and Josef Hintermair. Susanne for helping me in the chemistry lab, a place were my physicist's soul never felt very comfortable. And Onkel Josef for helping me in the biology lab, similar feelings apply here. In addition, he always took the time for a very nice chat about everything and soccer. Actually that is a good point to appreciate the club TSV 1860 München for the really extremely joyful Friday evening in the lab when they relegated ("...Freiheit für 60..."). Then I have to thank Stefan Grumbein and Manuel Viermetz. They took care of the IMETUM coffee machine. Without them I am sure you would sit in front of a blank paper right now. In the end I would like to thank the cleaning lady Olga for her work but especially for her good mood in which she was every day, really every day.

And finally I would like to address to Hahko Lee and Changwook Min from the Harvard Medical School. During my PhD I had the joy to cooperate with them.

정말 감사합니다